Universidade de São Paulo
Instituto de Física

Desenvolvimento de simulações de detetores de nêutrons baseados em estruturas GEM

Renan Felix dos Santos

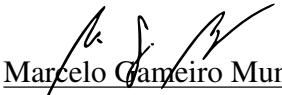

Orientador: Prof. Dr. Marcelo Gameiro Munhoz
Coorientador: Prof. Dr. Maurício Moralles

Dissertação de mestrado apresentada ao Instituto de Física da Universidade de São Paulo, como requisito parcial para a obtenção do título de Mestre em Ciências.

Banca Examinadora:
Prof. Dr. Marcelo Gameiro Munhoz - Orientador (IFUSP)
Prof. Dr. Sandro Fonseca de Souza (UERJ)
Prof[a]. Dra. Carmen Cecília Bueno (IPEN)

São Paulo
2023

FICHA CATALOGRÁFICA
Preparada pelo Serviço de Biblioteca e Informação
do Instituto de Física da Universidade de São Paulo

Santos, Renan Felix dos

Desenvolvimento de simulações de detetores de nêutrons baseados em estruturas GEM. São Paulo, 2023.

Dissertação (Mestrado) - Universidade de São Paulo. Instituto de Física. Depto. de Física Nuclear.

Orientador(a): Prof. Dr. Marcelo Gameiro Munhoz

Área de Concentração: Instrumentação em Física

Unitermos: 1. Nêutrons; 2. Física nuclear; 3. Detetores radioativos.

USP/IF/SBI-005/2023

University of São Paulo
Physics Institute

Simulation studies of GEM-based neutron detectors

Renan Felix dos Santos

Supervisor: Prof. Dr. Marcelo Gameiro Munhoz
Co-supervisor: Prof. Dr. Maurício Moralles

Dissertation submitted to the Physics Institute of the University of São Paulo in partial fulfillment of the requirements for the degree of Master of Science.

Examining Committee:
Prof. Dr. Marcelo Gameiro Munhoz - Supervisor (IFUSP)
Prof. Dr. Sandro Fonseca de Souza (UERJ)
Prof[a]. Dra. Carmen Cecília Bueno (IPEN)

São Paulo
2023

Dedico este trabalho à minha avó, Antonia

Agradecimentos

À Cristiane, pelo incentivo e apoio incondicional durante todo este trabalho. Pela paciência, companheirismo e por todo o carinho.

Aos meus pais, Keila e Edson, minha irmã, Caroline, e avós, Marina e José Arnaldo, por todo o apoio oferecido em todas as fases da minha vida.

Aos meus tios, Katia e Kleber, e a todos os familiares, Ana, Vaete, Maisa, entre tantos outros, pelo encorajamento de sempre.

Ao meu orientador Marcelo Munhoz por possibilitar que este projeto fosse concluído. Agradeço pelos muitos ensinamentos, pela paciência e por todo o tempo a mim dedicado. Seu acompanhamento distinto, preciso e sensato foram indispensáveis.

Ao meu coorientador Maurício Moralles, pelas ricas contribuições. Sua colaboração agregou de maneira ímpar ao trabalho.

Aos professores Marco Bregant, Tiago Fiorini e Francisco Souza pelas sugestões e ideias.

Aos meus colegas Lucas Filho, Geovane Grossi e Leonardo Campos pela colaboração generosa.

Ao professor Antonio Riul, pelo incentivo que me impulsionou a continuar.

Ao professor Edmilson Manganote por todo o conhecimento partilhado desde a iniciação científica e por toda a assistência desde então. Sua presença afetuosa e a confiança que sempre depositou em mim foram indispensáveis para que eu chegasse até aqui.

Resumo

Detetores de nêutrons são importantes em muitas áreas, como física, química, biologia e medicina. O $^{3}\mathrm{He}$ é amplamente utilizado em detetores gasosos de nêutrons, porém desde o início da década de 2000 uma forte escassez no fornecimento desse gás motivou a comunidade científica a buscar soluções alternativas com detetores livres de $^{3}\mathrm{He}$, empregando $^{113}\mathrm{Cd}$, $^{157}\mathrm{Gd}$, $^{10}\mathrm{B}$, ou $^{6}\mathrm{Li}$ como conversor de nêutrons.

Uma estrutura muito promissora é o multiplicador gasoso de elétrons (GEM) combinado com uma camada de boro-10 como conversora. Esta estrutura pertence à família dos detetores gasosos microestruturados (MPGD) que surgiram na década de 90. Essas estruturas são amplamente utilizadas em sistemas de rastreamento de partículas, como a câmara de projeção temporal (TPC) do experimento ALICE no LHC-CERN, e foram propostas para muitas outras aplicações, incluindo a deteção de nêutrons.

O estudo e desempenho dos detetores podem ser desenvolvidos através de simulações de Monte Carlo, explorando a resposta do detetor em diversas condições, com diferentes configurações e partículas sem o custo de construção de um protótipo. É comum utilizar as ferramentas GEANT4 e Garfield++ para realizar estas simulações, que compreendem a interação nuclear do nêutron, bem como a propagação dos produtos dessa interação e de elétrons frutos da ionização no meio gasoso, suas interações e a formação da avalanche.

Os produtos da reação $^{10}\mathrm{B}(n,\alpha)^{7}\mathrm{Li}$ possuem um alto poder de ionização levando a cálculos de CPU muito demorados e tornando-os impossíveis de serem realizados, mesmo em um cluster de computadores. A redução do tempo de processamento em várias ordens de grandeza é crucial para um estudo substancial e com suficiente estatística. Portanto, um simulador rápido foi desenvolvido neste trabalho para avaliar o desempenho de detetores de nêutrons baseados em MPGD de forma eficiente.

Este trabalho consiste no estudo do desempenho e otimização de detetores de nêutrons térmicos sensível à posição baseados em GEMs utilizando uma simulação rápida desenvolvida para este projeto. As otimizações se concentram em melhorar a resolução espacial explorando as propriedades do gás utilizado, assim como sua composição e pressão, provocando tanto alterações na distância percorrida pelos produtos da reação bem como na difusão e deriva dos elétrons. Os resultados deste trabalho indicam possíveis caminhos para a otimização desses detetores além de prover uma ferramenta versátil para estudos futuros desse tipo de detetor.

Palavras-chave: detetores de nêutrons, detetores gasosos microestruturados, Gas Electron Multiplier, GEANT4, Garfield++.

Abstract

Neutron detectors are important in many areas such as physics, chemistry, biology, and medicine. The $^{3}\mathrm{He}$ is widely used in neutron gaseous detectors however since the early 2000s a severe shortage in the supply of this gas motivated the scientific community to search for alternative solutions with $^{3}\mathrm{He}-\mathrm{free}$ detectors, employing $^{113}\mathrm{Cd}$, $^{157}\mathrm{Gd}$, $^{10}\mathrm{B}$, or $^{6}\mathrm{Li}$ as neutron converter.

A very promising structure is the Gas Electron Multiplier (GEM) combined with a boron-10 converter layer. It belongs to the family of Micro-Pattern Gaseous Detectors (MPGD) which are a type of gaseous detector with small structures that emerged in the 90s. These small structures are widely used in particle tracking systems, such as the Time Projection Chamber of the ALICE experiment in the LHC-CERN, and are proposed for many other applications, including neutron detection.

The study and performance of the detectors can be developed through Monte Carlo simulations exploiting the detector response in various conditions, with different particles and configurations without the cost of building a prototype. It is common to use the frameworks GEANT4 and Garfield++ to accomplish these simulations, which comprehend the nuclear interaction of neutrons as well as the propagation of the reaction products and ionization electrons in the gas medium, its interactions, and the avalanche formation.

The reaction products from $^{10}\mathrm{B}(n,\alpha)^{7}\mathrm{Li}$ have a high ionizing power leading to very time consuming CPU calculations making it impossible to perform them even in a computer cluster. The reduction in processing time by several orders of magnitude is crucial for a substantial study with enough statistics. Therefore, a parameterized fast simulator was developed in this work to evaluate the charge distribution in a more efficient way.

This work consists in the study of the performance and optimization of thermal neutron position-sensitive detectors based on GEMs using simulations. The optimizations focus on improving the spatial resolution by exploiting the properties of the working gas, such as its composition and its pressure, making changes in reaction products path length and electron drift and diffusion. The results of this work indicate possible ways to optimize these detectors in addition to providing a versatile tool for future studies of this type of detector.

Keywords: neutron detectors, micropattern gaseous detectors, Gas Electron Multiplier, GEANT4, Garfield++.

Contents

Introduction

The development of neutron detectors is important for different areas such as physics, chemistry, biology, and medicine. Since the early 2000s, the scientific community are searching for alternative solutions to neutron detectors equipped with helium-3 due to the shortage in the supply [1, 2, 3].

Micro-Pattern Gaseous Detectors (MPGD) are a type of gaseous detector with small structures that emerged in the 90s [4]. This new generation of detectors is employed using modern photo-lithographic technology. A very promising structure for neutron detection is the Gas Electron Multiplier (GEM) [5] which can be combined with a boron-10 converter layer and presents good spatial and energy resolution, robustness, and the possibility to operate at higher rates.

In the context of the development and optimization of particle detectors, Monte Carlo simulations are an essential tool to study the detector response in various conditions, with different particles and configurations without the cost of building a prototype. Each step in the development can be modeled in order to understand the signal generated by the detector.

A common strategy to simulate neutron detection with GEMs is based on the frameworks: GEANT4 [6] and Garfield++ [7]. The GEANT4 is a powerful tool to simulate the interaction of particles with matter, including the nuclear interaction of thermal neutrons. The software Garfield++ is well suited for gaseous detectors due to its very detailed simulation of electrons propagation in the gas medium, its interactions, as well as the avalanche formation.

In the case of neutron detectors, the reaction products from $^{10}\mathrm{B}(n,\alpha)^{7}\mathrm{Li}$ have a high ionizing power leading to a large number of electrons that needs to be considered in the avalanche simulation. This also leads to very time consuming CPU calculations that are impracticable even in a large computer cluster. Considering this fact, the reduction in processing time by several orders of magnitude is crucial for a substantial study with enough statistics. Thus, a fast simulation tool that uses a parameterization of the response function describing the charge deposited at the detector's readout plane was developed.

This work aimed to study the performance and optimization of thermal neutron position-sensitive detectors based on GEMs through simulations using GEANT4, Garfield++, and mainly the fast simulator. The optimizations focus on improving the spatial resolution by exploiting the properties of the working gas, such as its composition and its pressure, making changes in reaction products path length and the electron drift and diffusion. This dissertation is divided in seven parts as described below.

Chapter 1: Describes the characteristics of the neutron particle. Show the underlying concepts of the interaction of radiation with matter, focusing on neutrons and heavy

charged particles. This chapter also presents the main ideas regarding neutron detection methods.

Chapter 2: Discuss the processes in gaseous detectors like gas ionization, drift and diffusion of electrons, and amplification. Introduces a class of detectors known as Micro-Pattern Gaseous Detectors (MPGD) which is the "family" of the GEM structure. Finally, presents features to characterize the performance of a position-sensitive radiation detector.

Chapter 3: Introduces the simulation tools used in this project (GEANT4, Garfield++, SRIM, Gmsh, and Elmer) and how they work in each step of the development of the thermal neutron detection simulation. In this chapter, it is discussed the motivations for the creation of a fast simulator for neutron detection with GEM structures.

Chapter 4: Describes in detail the parameterization strategies used to construct the fast simulator.

Chapter 5: Presents a double-GEM detector prototype developed and tested in partnership with the Nuclear and Energy Research Institute (IPEN) which was partially used to validate the simulations and the fast simulator.

Chapter 6: Perform detector optimizations aiming for the improvement in spatial resolution by changing the gas composition as well as its pressure using the fast simulator.

Chapter 7: Finally, the conclusion of this work with the considerations about the findings and perspectives.

Chapter 1

Thermal Neutron Detection

After the suggestion of the existence of a neutral particle inside the nucleus by Ernest Rutherford in the 1920s [8], several experiments were performed searching for this new particle. In particular, an experiment conducted by Bothe and Becker in 1930 [9] discovered that when alpha particles pass through beryllium, radiation that is not affected by electromagnetic fields is produced and they assumed it was gamma radiation.

Irène Joliot-Curie and Frédéric Joliot irradiate paraffin with this radiation that comes from the beryllium and observed that this "new" radiation is able to eject protons [10]. They interpret this process as a kind of Compton effect.

Later, in 1932, James Chadwick studied the results [11] and the interpretation proposed by Irène and Frédéric using the Klein-Nishina formula. According to the Klein-Nishina formula, the cross section for the Compton effect is inversely proportional to the square of the mass of the recoiling particle [12]. Considering that the recoiling particle is a proton, two problems appear:

- the number of protons observed in the experiment is two times higher than the one predicted by the Klein-Nishina formula and
- the energy predicted by the formula is smaller than the observed one.

Then, Chadwick conclude that these problems could be solved if this radiation is the neutron proposed by Rutherford. Using the experimental apparatus in Figure 1.1, Chadwick could reproduce the experiment with paraffin and with many other light elements such as helium, lithium, beryllium, boron, carbon, nitrogen, oxygen, and argon. For all these elements, the "beryllium radiation" was capable to eject particles, leading Chadwick to publish his famous paper *"The existence of a neutron"* in June of 1932 [11].

1.1 Neutron Characteristics

One of the building blocks of matter, composed of two down quarks and one up quark, the neutron is an interesting particle because it is almost insensitive to electromagnetic fields and does not feel the coulomb barrier which allows it to pass through electronic barriers and become a tool to study the nuclei. In this section, the general characteristics of neutrons will be presented.

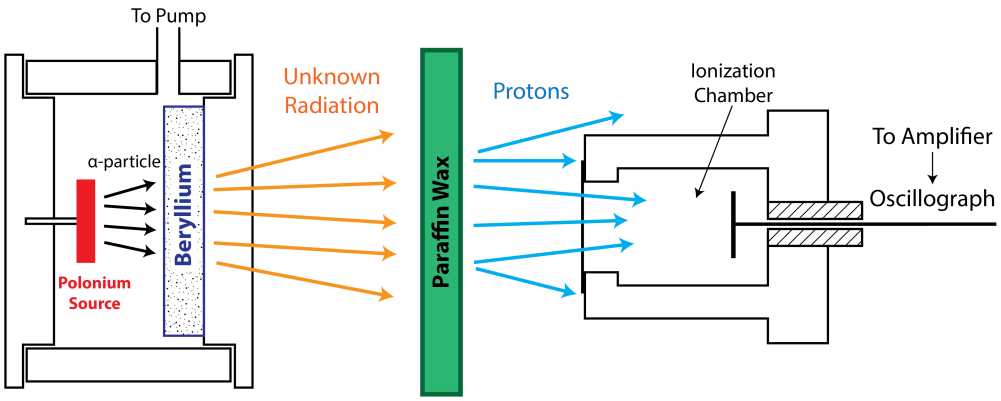

Figure 1.1: Experimental apparatus used by James Chadwick. Adapted from [11].

Lifetime

A free neutron is not stable and decays as $n \rightarrow p + e + \bar{\nu}_e$ but there is a dilemma in neutron lifetime observed by the two most precise measurements methods: *"bottle"* and *"beam"* method [13]. In the first one, ultracold neutrons are confined in a bottle and the number of neutrons inside is measured at times t fitting an exponential decay

$$N(t) = N(0)e^{\frac{-t}{\tau_n}},$$

where recent results achieved $\tau_n = (877.75 \pm 0.28_{\text{stat}} + 0.22_{\text{sys}} - 0.16_{\text{sys}})\text{s}$, the highest precision until now [14].

In the beam method, the lifetime is measured from the differential exponential decay

$$\frac{dN}{dt} = \frac{-N}{\tau_n},$$

where $\frac{dN}{dt}$ is the rate of neutron decay and N the number of neutrons in a determined beam volume. The last measurement by this beam method shows a lifetime of $\tau_n = (887.7 \pm 1.2_{\text{stat}} \pm 1.9_{\text{sys}})\text{s}$ [15], hence neutrons in a beam live almost $10\,\text{s}$ additionally. Some results from these two methods are shown in Figure 1.2. Both methods show enough lifetime for detection purposes in this dissertation.

Mass

Chadwick's experiment came with mass measurements. Nowadays the error in neutron mass is limited by the uncertainty in the Avogadro's number, where the most recent measured value is [17]:

$$m_n = 1.008\,664\,915\,9(5)\,\text{u} = 939.565\,413(6)\,\text{MeV},$$

which is slightly heavier than a proton.

Magnetic Moment

Although approximately 1000 times smaller than the magnetic moment of an electron and with no net charge, the neutron has a magnetic moment that was measured directly

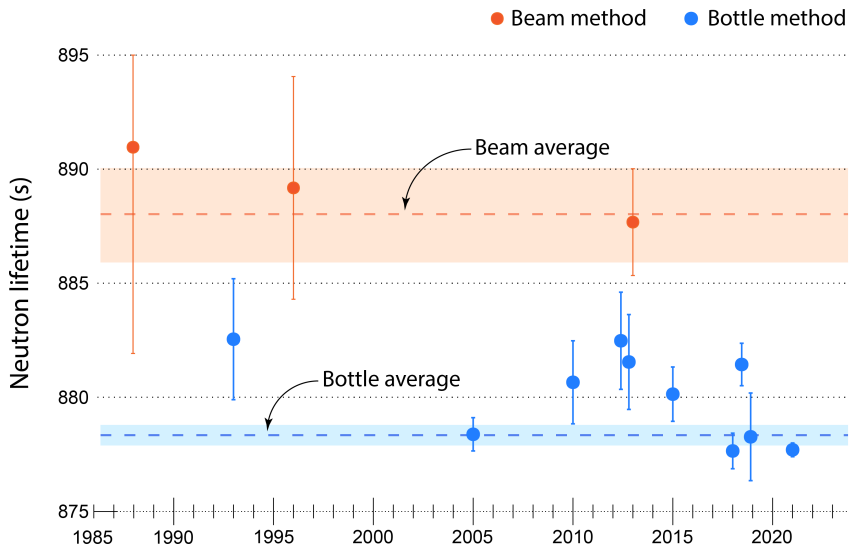

Figure 1.2: Neutron lifetime measurements using the bottle and beam method. Adapted from [16].

by Alvarez and Bloch [18] at Berkeley in 1940. The most recent measured value is [17]:

$$\mu_n = -1.9130427(5)\mu_N,$$

where μ_N is the physical constant of the magnetic moment called nuclear magneton (defined in SI units as $\mu_N = \frac{e\hbar}{2m_p}$, where e is the elementary charge, $\hbar$ is the reduced Planck constant, m_p is the proton rest mass, and c is the speed of light). In SI units, its value is

$$\mu_N = 5.050\,783\,746\,1(15)\,\mathrm{J\,T^{-1}}.$$

1.2 Neutron Classification

The reactions that the neutron can undergo depend on its energy and therefore it is interesting to classify them based on their kinetic energy. In a non-relativistic limit, the kinetic energy E of a neutron can be described by its wavelength through the de Broglie relation [19]:

$$\lambda = \frac{h}{m_n v}, \tag{1.1}$$

where h is the Planck constant, v is the velocity, and m_n is the neutron's mass. Then the energy can be written as [19]

$$E = \frac{1}{2}m_n v^2 = \frac{h^2}{2m_n\lambda^2}, \tag{1.2}$$

and the neutron classification by its energy regime is shown in Table 1.1.

The main topic of this dissertation is thermal neutrons, which means that they are in thermal equilibrium with the medium, and for a temperature of 293 K, the average energy is 25 meV.

Table 1.1: Neutron classification with respect to its kinetic energy, wavelength and velocity. Adapted from [20].

	Kinetic Energy [eV]	Wavelength [Å]	Velocity [m/s]
Ultracold	$< 3 \cdot 10^{-7}$	< 520	< 7.5
Very Cold	$3 \cdot 10^{-7} - 5 \cdot 10^{-5}$	$520 - 40$	$7.5 - 100$
Cold	$5 \cdot 10^{-5} - 5 \cdot 10^{-3}$	$40 - 4$	$100 - 1000$
Thermal	$5 \cdot 10^{-3} - 5 \cdot 10^{-1}$	$4 - 0.4$	$1000 - 10000$
Thermal Peak	$25.3 \cdot 10^{-3}$	1.8	2200
Epithermal	$5 \cdot 10^{-1} - \cdot 10^{3}$	$0.4 - 0.01$	$10^3 - 4.4 \cdot 10^5$
Intermediate	$10^3 - 10^5$	$0.01 - 0.001$	$4.4 \cdot 10^5 - 4.4 \cdot 10^6$
Fast	$10^5 - 2 \cdot 10^7$	$0.001 - 6 \cdot 10^{-5}$	$4.4 \cdot 10^6 - 6.2 \cdot 10^7$
High Energy	$> 2 \cdot 10^7$	$< 6 \cdot 10^{-5}$	$> 6.2 \cdot 10^7$

Energy and Velocity

The neutrons in the thermal region have similar energy distribution as gas molecules, thus the kinetic energy is related to temperature by the Maxwell-Boltzmann distribution [21]:

$$f(E) = \frac{2\pi}{(\pi kT)^{\frac{3}{2}}} e^{-\frac{E}{kT}} E^{\frac{1}{2}}, \tag{1.3}$$

where $f(E)$ is the fraction of neutrons of energy E per unit energy interval; k is the Boltzmann constant $8.6 \times 10^{-5}\,\mathrm{eV/K}$ and T the absolute temperature in Kelvin. The behavior of this distribution is sketched in Figure 1.3 where it is shown the behavior of two values of temperature.

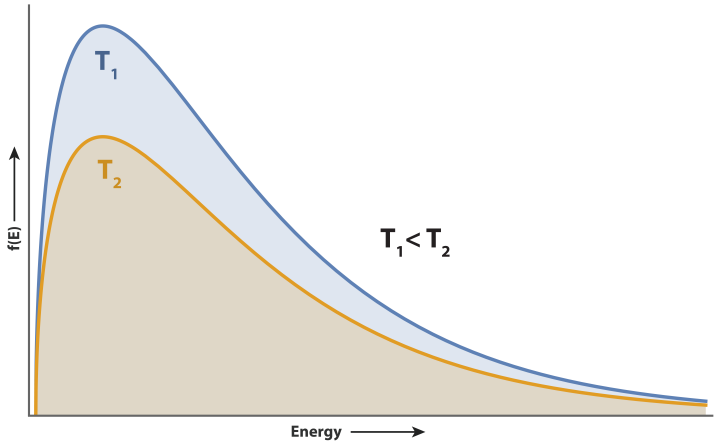

Figure 1.3: Maxwell-Boltzmann energy distributions for the temperatures $T_1 = 500\,\mathrm{K}$ and $T_2 = 400\,\mathrm{K}$.

Setting $\frac{df(E)}{dE} = 0$, the most probable energy is

$$E = kT \tag{1.4}$$

where for room temperature ($T = 293\,\mathrm{K}$) gives an energy of $25\,\mathrm{meV}$, hence the velocity of a neutron moving at the most probable energy is

$$v = \sqrt{\frac{2kT}{m_n}} = \frac{2 \times 0.025\,\mathrm{eV}}{939.6\,\mathrm{MeV}/c^2} \quad \rightarrow \quad v \approx 2.2 \times 10^3\,\mathrm{m/s}. \tag{1.5}$$

The Maxwell-Boltzmann distribution in Eq. 1.3 can be rewritten in terms of the velocity as

$$f(v) = \sqrt{\left(\frac{m}{2\pi k_B T}\right)^3} 4\pi v^2 \exp\left(-\frac{mv^2}{2k_B T}\right). \tag{1.6}$$

Using this equation, the velocity distribution of molecules in different gases can be calculated as shown in Figure 1.4. As will be discussed in detail in Section 2.1.2, the velocity of electrons in a gas affects its drift and diffusion. The drift and diffusion of electrons are connected with the spatial resolution of the detector which this work aims to improve in Chapter 6.

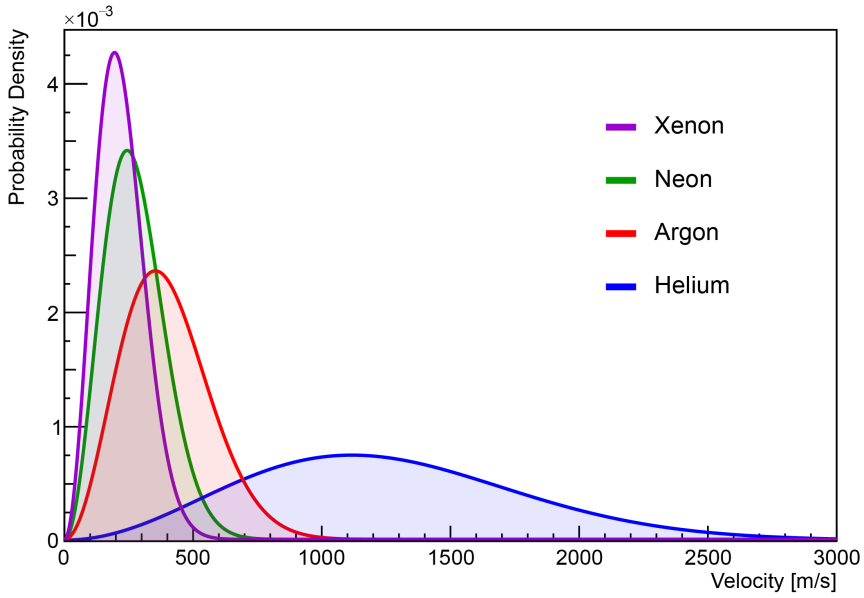

Figure 1.4: Maxwell-Boltzmann velocity distributions for different gases with $300\,\mathrm{K}$.

1.3 Particle Interaction with Matter

The detection and measurement of radiation and particles are only possible through their interactions with matter. The processes involved in the interaction depend on the type of the particle (e.g. photons, charged particles, neutrons, etc). The development of a radiation detector is intrinsically connected to the particle interaction and the energy deposited in the detector material. Thus, it is of extreme importance to know and understand the radiation interactions when developing this kind of detector.

This section is an introduction to an extensive subject and here the focus is thermal neutron detection. A comprehensive study of these interactions can be found in [22, 23, 24].

1.3.1 Underlying Concepts

Cross Section

The cross section is a quantity that describes the interaction of two particles in terms of a measured probability for a reaction to occur. Assume that a flux Φ (number of particles per unit area per unit time) of incident particles uniformly distributed in space and time is impinging upon a target material as shown in Figure 1.5. A fraction of these particles will scatter in the material (the type of interaction is not important now) and suppose a detector is able to count the average number of particles per unit time dN_s scattered per unit solid angle[1] $d\Omega$. The *differential* cross section is defined as [23]

$$\frac{d\sigma}{d\Omega}(E,\Omega) = \frac{1}{\Phi}\frac{dN_s}{d\Omega}, \tag{1.7}$$

where $\frac{d\sigma}{d\Omega}$ is the average fraction of the particles scattered into $d\Omega$ per unit time per unit flux Φ. The dimensions of the flux make $d\sigma$ have dimensions of area, leading to the interpretation that $d\sigma$ is the geometric cross sectional area of the target intercepting the beam [23].

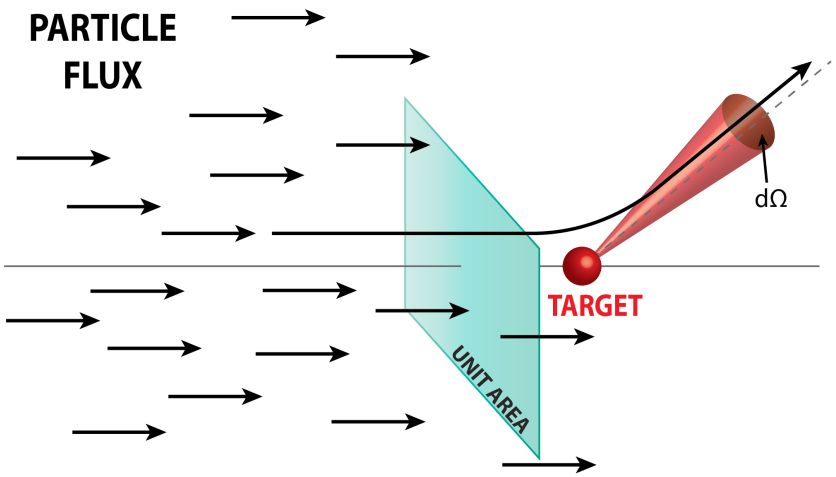

Figure 1.5: Illustration of scattering cross section. Adapted from [23].

The value defined in Eq. 1.7 varies with the energy and with the angle, therefore integrating this over all space results in the *total* cross section as [23]

$$\sigma(E) = \int d\Omega \frac{d\sigma}{d\Omega}. \tag{1.8}$$

Mean Free Path

The mean free path can be defined as the mean distance traveled by a particle before it suffers a collision. This distance is related to the cross section and the material density as

[1] The *solid angle* measures the fraction a sphere one has delimited with a given area on the surface of a sphere

[22]

$$\lambda = \frac{1}{\rho_n \sigma}, \tag{1.9}$$

where σ is the cross section and

$$\rho_n = \frac{N_A \rho}{A} \tag{1.10}$$

is the number density of the medium where A is the atomic weight of the material, N_A is the Avogadro number, and ρ is the weight density.

1.3.2 Heavy Charged Particles

These heavy charged particles, like ions and alpha particles, primarily interact with matter via coulomb interactions involving the orbital electrons. Interactions with nuclei are also possible but not significant in the response of radiation detectors [24].

Stopping Power

This quantity is defined as the rate at which a charged particle loses energy when traversing a material [22]

$$S = -\frac{dE}{dx}, \tag{1.11}$$

where the negative sign means that the particles are losing energy when moving in a material.

Hans Bethe, and later with the correction of Felix Bloch, proposed an expression to the energy loss known as the Bethe-Bloch formula [22]:

$$-\frac{dE}{dx} = \frac{4\pi N_A r_e^2 m_e c^2 \rho Z q^2}{A\beta^2} \left[ln\left(\frac{W_{max}}{I}\right) - \beta^2 - \frac{\delta}{2} - \frac{C}{Z} \right] \tag{1.12}$$

where N_A is the Avogadro's number, r_e is the classical electron radius, m_e is the electron mass $\times$ c^2, q is the electrical charge of the ion. ρ, Z, A, and I are the density, atomic number, atomic mass, and ionization potential of the medium, respectively. β, δ, and C are correction factors. Finally, W_{max} is the maximum possible energy transfer to an electron in a single collision.

Bragg Curve

When a particle loses energy in the material, its stopping power, i.e. effectiveness of ionization, changes. This happens because with a decrease in energy, the scattering cross section increases causing even more ionization in their path giving rise to a pronounced peak in the energy loss as a function of depth of penetration, called *Bragg peak* [22]. This peak can be seen on a *Bragg curve* like shown in Figure 1.6.

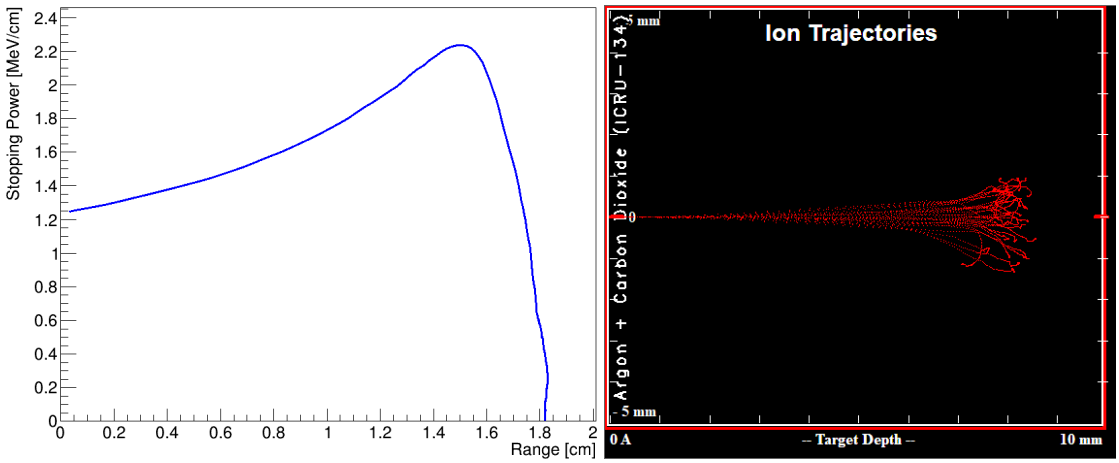

Figure 1.6: Left: Bragg peak for alpha particles having initial energy of $3\,\mathrm{MeV}$ moving into Ar:CO_2 gas mixture. Right: alpha particle trajectories in gas. Simulated in SRIM [25].

1.3.3 Neutrons

Neutrons carry no charge and therefore can not interact with the electric field of atoms interacting primarily via strong nuclear force [22]. Depending on its energy, the neutron can interact with the nuclei through scattering (elastic or inelastic), spallation, transmutation, or radiative capture. Neutron interaction classification is given in Figure 1.7 [26].

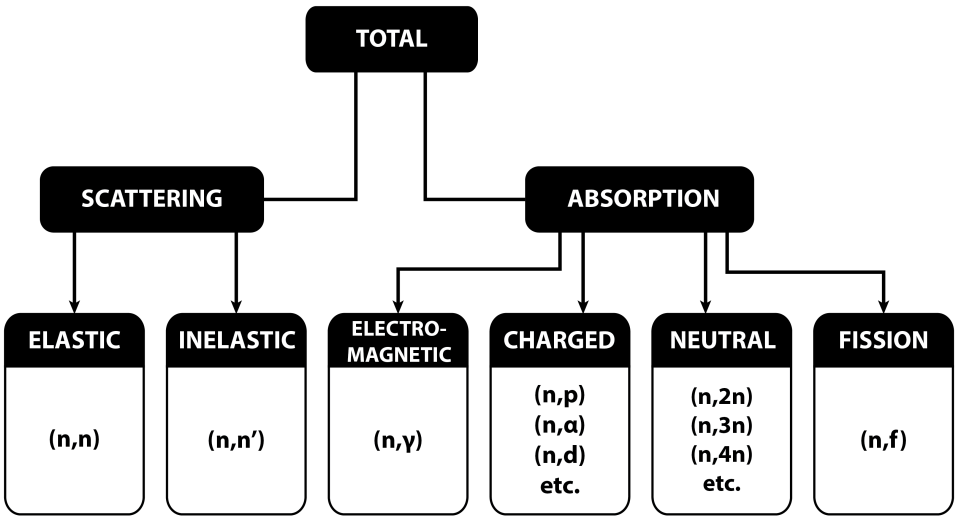

Figure 1.7: Neutron interaction classification. Adapted from [26].

Elastic Scattering

This reaction is written as

$$\mathrm{n} + \mathrm{X}_p^{n+p} \rightarrow \mathrm{n} + \mathrm{X}_p^{n+p}, \tag{1.13}$$

thus the state of the nucleus is not affected and it remains the same after the reaction. This is the principal mode of interaction of neutrons with the atomic nuclei.

Inelastic Scattering

Now, the target nucleus is left in an excited state in a process where the neutron is temporarily absorbed by the nucleus creating a compound and a unstable one. In the de-excitation, a neutron with lower energy is emitted. The reaction is written as

$$\mathrm{n} + \mathrm{X}_p^{n+p} \rightarrow \mathrm{n} + [\mathrm{X}_p^{n+p}]^*. \tag{1.14}$$

Transmutation (Charged)

Here the neutron is captured by the nucleus, producing a compound nucleus that loses energy by emitting a charged particle and producing a nucleus of a different element, like

$$\mathrm{n} + \mathrm{B}_5^{10} \rightarrow \alpha + \mathrm{Li}_3^7. \tag{1.15}$$

Radiative Capture (Electromagnetic)

This reaction is characterized by the emission of a gamma particle from a compound nucleus which is an isotope of the same element as the original nucleus:

$$\mathrm{n} + \mathrm{X}_p^{n+p} \rightarrow [\mathrm{X}_p^{n+p+1}] + \gamma. \tag{1.16}$$

The production of radioisotopes, such as cobalt-60, are an example of this interaction:

$$\mathrm{n} + \mathrm{Co}^{59} \rightarrow \mathrm{Co}^{60} + \gamma. \tag{1.17}$$

Fission

This process occurs when a heavy nucleus captures a slow neutron and is excited. After a while, the nucleus split into fragments resulting in neutrons and gamma-ray photons. The fission of uranium-235 is an example of this process:

$$\mathrm{n} + \mathrm{U}_{92}^{235} \rightarrow \mathrm{I}_{39}^{139} + \mathrm{Y}_{53}^{95} + 2\mathrm{n} + \gamma. \tag{1.18}$$

1.4 Neutron Detection Methods

As mentioned before, neutron detection techniques must involve a nuclear reaction that results in energetic charged particles. The cross section of each interaction strongly depends on the neutron energy. This dissertation is focused on slow neutrons detection whose energy is below the cadmium cutoff of about $0.5\,\mathrm{eV}$. For fast neutron interaction, a complete discussion is presented in [24].

1.4.1 Helium-3 Crisis

Considering gaseous detectors, helium-3 was the most chosen counting gas until the early 2000s when US homeland security install radiation detection, based on helium-3, in their borders and international ports after the terrorist threat, increasing the demand for this gas and causing a shortage in the supply [27] as shown in Figure 1.8. This problem led the researchers to search for a replacement for helium-3.

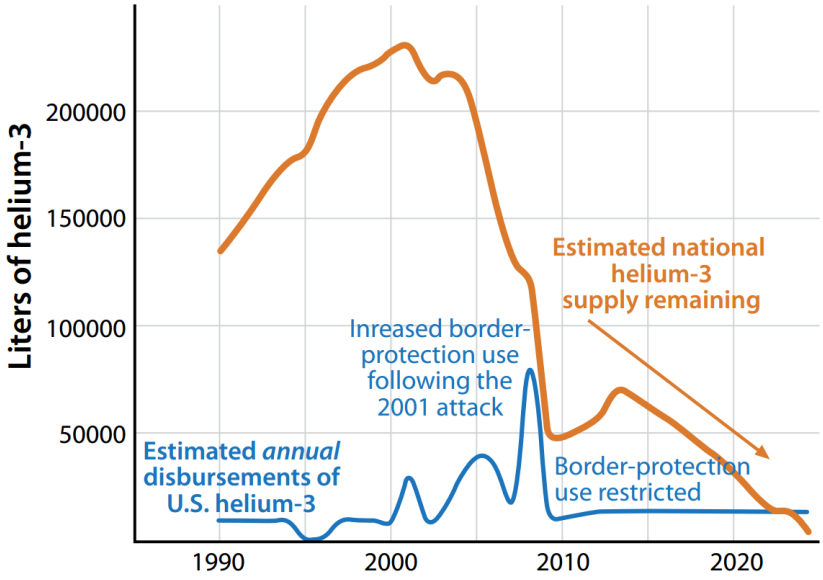

Figure 1.8: In orange is showed the U.S. supply of helium-3 and its decline since the terrorist attacks of 2001. Annual releases, in blue, were reduced to extend the stockpile. Figure from [28].

With the increasing necessity of an alternative to neutron detectors helium-3 based, the number of papers and citations, indexed by the Web of Science, involving the words “neutron” and “detection” (or “detector”) in their title increased abruptly as shown in Figure 1.9. This shows an area with a still increasing demand and probably promising landmarks.

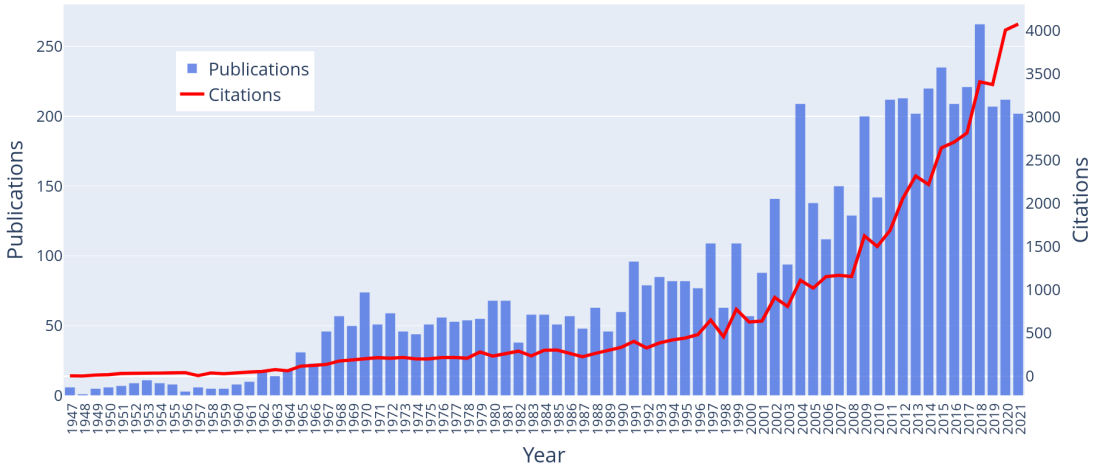

Figure 1.9: Number of papers and citations since 1947 with words “neutron” and “detection or detector” within title searched in Web of Science.

1.4.2 Nuclear Reactions

The selection of nuclear reactions that can result in a charged particle depends on the cross section of these reactions to occur in the slow neutron region. Additionally to the cross section, a quantity called Q-value of the reaction that determines the energy liberated in the reaction following neutron capture must be considered. A higher Q-value means that a greater amount of energy is given to the reaction products allowing good discrimination against γ-rays. Furthermore, the range of the reaction products is also an important aspect to be considered in the detector construction. Figure 1.10 shows the cross section versus neutron energy for the three most common materials used to generate the reactions of interest in neutron detection: Helium-3, Boron-10, and Lithium-6 [24].

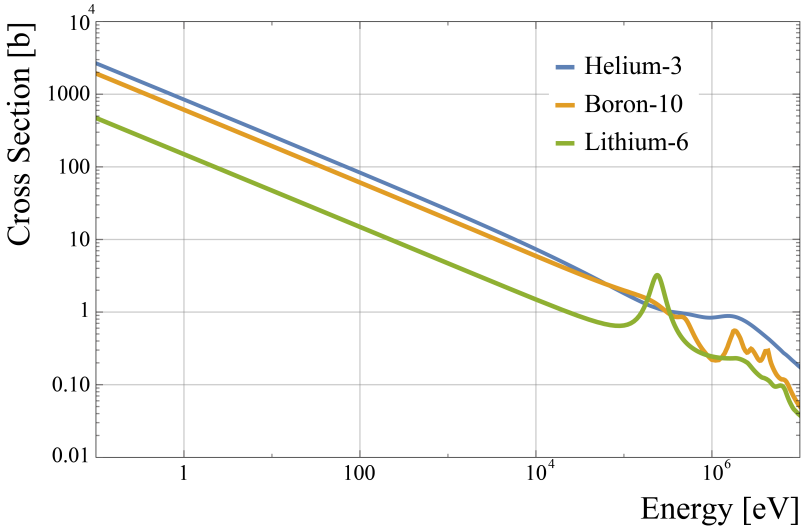

Figure 1.10: Cross sections of ^{10}B, ^{3}He, ^{6}Li with respect to neutron energy. Data from [29].

$^{10}\mathbf{B}(\mathbf{n},\alpha)$ Reaction

This reaction is probably the most useful reaction for thermal neutron detection due to its large cross section and the $1/v$ energy dependence [30]. The reaction can be written as

$$\mathrm{n} + {}^{10}\mathrm{B} \longrightarrow \begin{cases} {}^{4}\mathrm{He} + {}^{7}\mathrm{Li}: & \underset{Q\text{-value}}{2.792\ \mathrm{MeV}}\ \text{(ground state, about 6\%)} \\ {}^{4}\mathrm{He} + {}^{7}\mathrm{Li}^{*}: & 2.310\ \mathrm{MeV}\ \text{(excited state, about 94\%)}, \end{cases} \tag{1.19}$$

where there are two possible reactions. The first one represents the non-radiative channel with a branching ratio of $6\,\%$ and Q-value $= 2.792\,\mathrm{MeV}$. The second one is a radiative channel with a branching ratio of $94\,\%$ and Q-value $= 2.310\,\mathrm{MeV}$, where ${}^{7}\mathrm{Li}^{*}$ is an excited state that rapidly de-excite by emitting a γ-ray of $478\,\mathrm{keV}$. Both possibilities have a very large Q-Value compared with the income thermal neutron energy. Also, the reaction products must be emitted in exactly opposite directions due to the small incoming linear momentum. By conservation of energy and momentum the individual energies of the α-particles and lithium nucleus are:

$$\text{excited state:} \begin{cases} E_{Li} = 0.84\,\mathrm{MeV} \\ E_{\alpha} = 1.47\,\mathrm{MeV} \end{cases} \quad \text{ground state:} \begin{cases} E_{Li} = 1.02\,\mathrm{MeV} \\ E_{\alpha} = 1.78\,\mathrm{MeV} \end{cases} \tag{1.20}$$

$^{6}\mathbf{Li}(\mathbf{n},\alpha)$ Reaction

Neutron detection is also possible through the $^{6}\mathbf{Li}$ reaction, although with a lower cross section. The reaction leads to the products:

$$\mathrm{n} + {}^{6}\mathrm{Li} \longrightarrow {}^{3}\mathrm{H} + {}^{4}\mathrm{He}: \quad Q\text{-value } = 4.78\,\mathrm{MeV}. \tag{1.21}$$

When considering a position-sensitive detector, this reaction is less preferable because of the longer range of $^{3}\mathbf{H}$ than the products of $^{10}\mathbf{B}$ reaction.

$^{3}\mathbf{He}(\mathbf{n},\mathbf{p})$ Reaction

Widely used for neutron detection, the reaction using the Helium-3 can be written as:

$$\mathrm{n} + {}^{3}\mathrm{He} \longrightarrow {}^{3}\mathrm{H} + \mathrm{p}: \quad Q\text{-value } = 0.764\,\mathrm{MeV}. \tag{1.22}$$

Although it has a high cross section to thermal neutron and suitable reaction products, there is a severe lack of ${}^{3}\mathrm{He}$ and consequent high costs [27], as discussed in Section 1.4.1.

1.4.3 Boron Thin-Film

One way to use the boron reaction is to deposit a thin-film of boron close to the detector sensitive part. As the interaction can occur at any point inside the film and considering that the reaction products will lose energy as they move through the film, the thickness of the film must be kept as thin as possible to allow the products to enter in the detection region.

Figure 1.11 shows the energy loss of the reaction products, considering that the average particle range in solid boron-10 is $3.6\,\mu\mathrm{m}$ and $1.6\,\mu\mathrm{m}$ for α-particles and ^{7}Li, respectively. Given these particle ranges, Figure 1.12 shows two different points of interaction inside the converter foil (A and B) with the respective solid angle Ω to enter in the detector. τ_α and τ_{Li} are the radii of spheres that limit the accessible region for these particles. In (A) the interaction point is too far from the gaseous region, and both products have a low probability of detection. On the other hand, in (B), both products have a high probability to enter the detector. A and B are extreme cases, but in between these two cases, the detection probability is lower for ^{7}Li because of the shorter range compared with the α-particle.

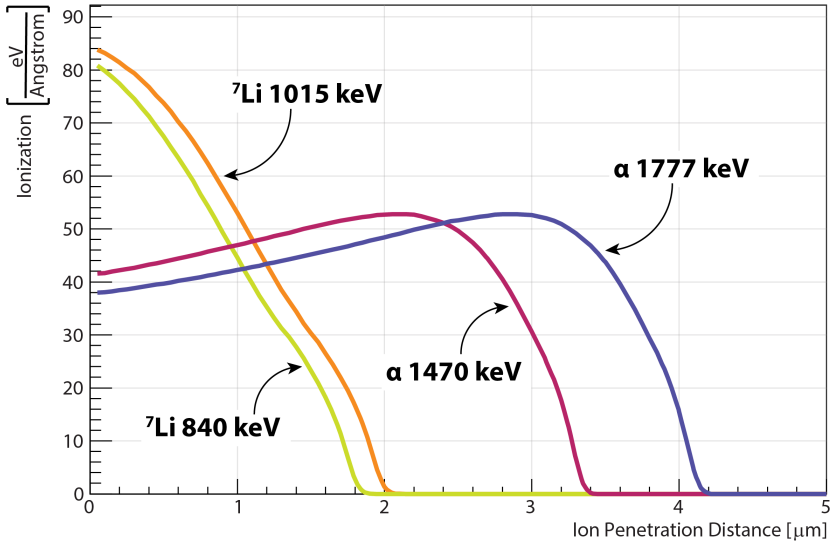

Figure 1.11: Energy loss of reaction products in ^{10}B. Adapted from [31].

Summary

Until now only general properties of neutrons were discussed as well as their mechanisms of interaction with matter. The detection of thermal neutrons involves the combination of a target material that produces measurable radiation together with a conventional radiation detector. So far, it was presented the first part of this procedure, exploiting especially the conversion of the thermal neutron with a nuclear reaction with boron-10. The next chapter will present gaseous detectors to accomplish the second step in this chain for neutron detection.

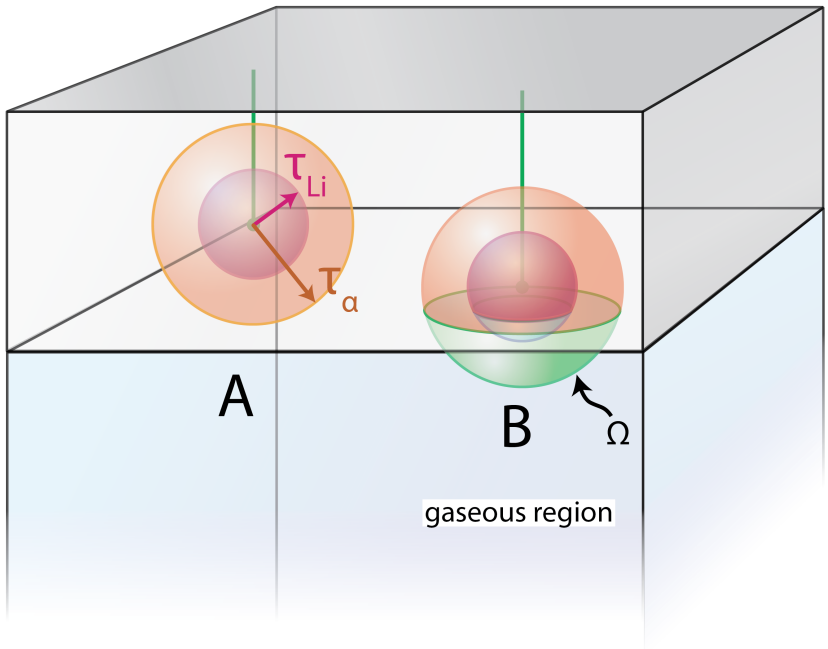

Figure 1.12: Solid angle reaction products inside boron converter layer. Adapted from [32].

Chapter 2

Gaseous Detectors

The use of gaseous detectors dates back to Rutherford and Geiger in 1908 [33]. When radiation traverses a region that is filled with gas, it can ionize the molecules generating electron-ion pairs that with an appropriate applied electric field results in a measurable electrical pulse. In the following sections, a more detailed description of this kind of detector will be provided focusing on the development of Micro-Pattern Gaseous Detectors (MPGD). An introduction to the most important concepts about the characterization of imaging systems will also be provided.

2.1 Basic Processes and Interactions in Gas

2.1.1 Gas Ionization

When a charged particle crosses a gaseous media, it can leave a track of ionization along its path. These charges created by the incident radiation itself are known as *primary* charge where the average energy needed to be created is referred to as the *W-value*. For most gases of interest in radiation detectors, this value lies within $25 - 45\,\mathrm{eV}$ per pair (see Table 2.1). Consider a particle that deposits some energy in the detector, ΔE, using the *W-value* the total number *N* of electron-ion pairs produced can be calculated as

$$N = \frac{\Delta E}{W}. \tag{2.1}$$

This number can also be written in terms of the stopping power dE/dx, as

$$N = \frac{1}{W}\frac{dE}{dx}\Delta x. \tag{2.2}$$

In a gas mixture, the number of total charge pairs can be calculated by a composition law as

$$n_t = \sum_i x_i \frac{(dE/dx)_i}{W_i}, \tag{2.3}$$

where i is the i-th gas and x_i is the fraction by volume of gas i.

These electron-ion pairs are created along the path of the charged particle that traverses the gas. The ionizing collisions are purely random and are characterized by the

Table 2.1: Properties for some gases: ionization potentials I_e (which is the minimum energy required to remove an electron from an isolated atom), W-values, stopping powers dE/dx, primary ionization yield n_p, and total ionization yield n_t of gases at standard conditions (where *ip* means the number of electron-ion pairs). Table from [22]

Gas	Z	Density (10^{-4} g/cm^3)	I_e (eV)	W (eV/pair)	dE/dx (keV/cm)	n_p (ip/cm)	n_t (ip/cm)
H_2	2	0.8	15.4	37	0.34	5.2	9.2
He	2	1.6	24.6	41	0.32	5.9	7.8
N_2	14	11.7	15.5	35	1.96	10	56
O_2	16	13.3	12.2	31	2.26	22	73
Ne	10	8.4	21.6	36	1.41	12	39
Ar	18	17.8	15.8	26	2.44	29	94
Kr	36	34.9	14.0	24	4.60	22	192
Xe	54	54.9	12.1	22	6.76	44	307
CO_2	22	18.6	13.7	33	3.01	34	91
CH_4	10	6.7	10.8	28	1.48	46	53

mean free path λ and the ionization cross section per electron σ_I [34]

$$\frac{1}{\lambda} = N_e \sigma_I \tag{2.4}$$

where N_e is the electron density of the gas. This inverse mean free path for ionization is called *cluster density*, also referred to as *specific ionization*.

Considering a path length L, the number of collisions k follows a Poisson distribution with mean L/λ

$$P(k|L,\lambda) = \frac{L^k}{\lambda^k k!} e^{\frac{-L}{\lambda}}. \tag{2.5}$$

The probability of having no ionization, $k = 0$, in L is

$$P(0|L,\lambda) = e^{\frac{-L}{\lambda}}, \tag{2.6}$$

and this equation can be used to calculate the value of λ [34]. The mean free path λ is an important parameter used in this work to study detector optimization aiming to improve the spatial resolution, as will be shown in Chapter 6.

There exist another mechanism of indirect ionization in gases, called Penning Effect. In some atoms, a deexcitation may occur through a collision with a second atom resulting in the ionization of this second atom. This happens in certain atoms where meta-stable states are excited and are unable to deexcite immediately to the ground state by the emission of a photon [23]. For instance, consider that an atom or molecule A^* collides with a second atom or molecule B

$$A^* + B \rightarrow A + B^+ + e^-. \tag{2.7}$$

2.1.2 Drift and Diffusion of Electrons in Gases

Understanding how the electron-ion pairs move in the gaseous medium is fundamental to optimize these detectors. When an electric field is applied, the motion of electrons and ions is characterized by drift and diffusion phenomena.

Drift

Using the classical kinetic theory of gases the drift properties of electrons in gas at temperature T in the absence of an electric field follow a Maxwellian distribution with the most probable value kT, and at room temperature, kT corresponds to $0.4\,\mathrm{eV}$. In the presence of an electric field E, these electrons acquire a drift velocity [35]:

$$w = \frac{eE}{m}\left\langle \frac{l}{v} \right\rangle = \frac{eE}{m}\tau, \tag{2.8}$$

where e, m, v, and l are, respectively, the charge, the mass, the velocity, and the mean free path of the electron, and τ is the average collision time. The electron energy (and then v) is a function of the reduced field E/P, l is inversely proportional to the gas pressure P, then the drift velocity is also a function of E/P [35].

When an increasing in values of E do not modify the energy of the electrons, the τ is constant, thus the drift velocity increases linearly with the field as:

$$w = \frac{eED}{kT}, \tag{2.9}$$

where k is the Boltzmann's constant, D is a field-dependent diffusion coefficient (generally given in $\mathrm{cm^2\,s^{-1}}$). A series of drift velocities of electrons in many gas mixtures as a function of the electric field is shown in Figure 2.1

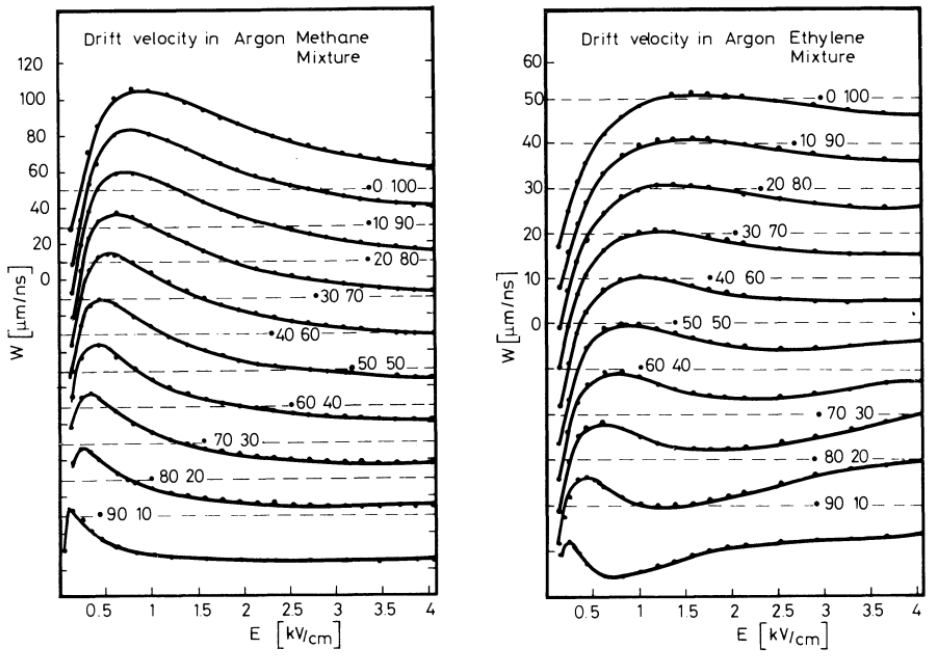

Figure 2.1: Electron drift velocity in gases as a function of the electric field. From [23].

Diffusion

Electron diffusion, i.e. the dispersion of the ionized electron position as a function of time, can be well described by a Gaussian curve of width σ_x. Consider an electron drifting in the x-axis, its position will disperse by an amount

$$\sigma_x = \sqrt{\frac{2Dx}{w}}, \tag{2.10}$$

where D is the *diffusion coefficient*. Substituting the Eq. 2.9 into Eq. 2.10, the *diffusion width* gives a thermal limit for the electron diffusion [35, 36]:

$$\sigma_x = \sqrt{\frac{2kTx}{eE}}. \tag{2.11}$$

Rewriting Eq. 2.9 as

$$\frac{eED}{w} = kT = \epsilon_k, \tag{2.12}$$

ϵ_k stands for characteristic energy which is a function of the reduced field E/P. In this way, the diffusion width can be expressed as

$$\sigma_x = \sqrt{\frac{2\epsilon_k x}{eE}} = \sqrt{\frac{2\epsilon_k}{e\frac{E}{P}}}\sqrt{\frac{x}{P}}, \tag{2.13}$$

and shows a clear dependence of the diffusion width on the pressure at a given E/P.

Electron Attachment and Recombination

A gas mixture can be composed of a polyatomic gas that degrades the performance of a detector absorbing electrons in a wide energy range [22] through two main processes: recombination and electron attachment.

Electron-ion pairs will recombine under the attraction of the electrical force when no electric field is applied, emitting a photon in this process known as recombination:

$$X^+ + e^- \rightarrow X + h\nu. \tag{2.14}$$

The second process is the electron attachment which free electrons are captured by an atom with a high electronegativity:

$$e^- + X \rightarrow X^- + h\nu. \tag{2.15}$$

Hence, the detection efficiency is severely diminished when electronegative gases are present in the detector [23].

2.1.3 Amplification

When the primary electrons gain sufficient energy accelerating through the electric field, they can also ionize gas molecules resulting in secondary electrons. This process can continue to produce tertiary ionization and so on, resulting in the formation of an avalanche.

In Figure 2.2 it is shown a schematic view of the avalanche formation. When ionizing radiation passes through a gaseous media, the ionized charges form a liquid droplet shape due to the fact that electrons (orange) are faster than ions (blue).

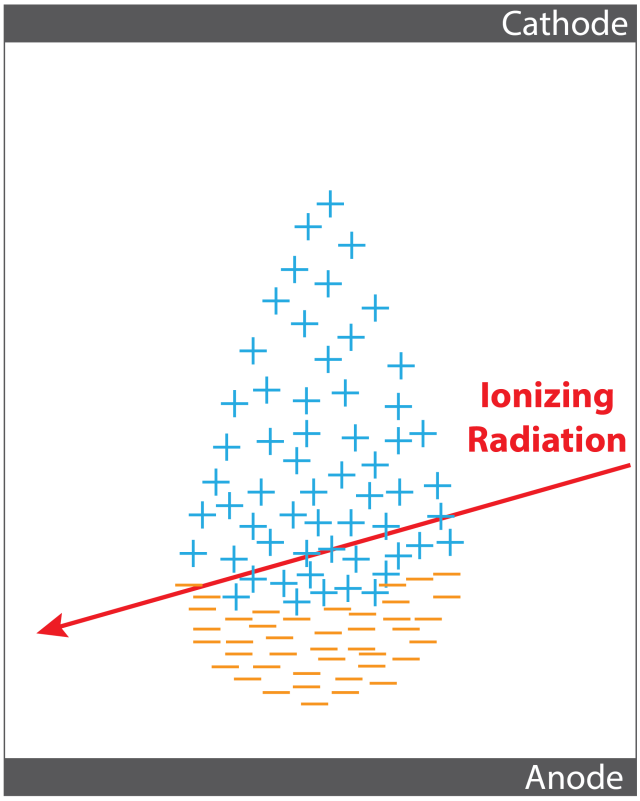

Figure 2.2: Avalanche droplet shape. Adapted from [22].

The number of electrons created by n primary electrons in this path dx will be

$$dn = n\alpha dx \tag{2.16}$$

where $\alpha = 1/\lambda$ is the *first Townsend coefficient* (λ is the mean free path). The number of final electrons is obtained by integrating the Eq. 2.16:

$$n = n_0 \exp(\alpha x) \tag{2.17}$$

where the ratio $\frac{n}{n_0}$ is a multiplication factor called *gas gain*, one important parameter for development of proportional counters.

2.1.4 Regions of Operation

Detectors with gaseous media have different regions of operation based on the applied field. These regions are recombination, ion chamber, proportional, region of limited proportionality, Geiger-Müller, and discharge [22]; all shown in Figure 2.3.

The first region is the **recombination region** where the ionization tends to form neutral molecules due to the low voltage applied and this recombination decreases as the voltage increases.

The second region, called **ion chamber region**, is characterized by the feature that all electron-ion pairs produced are collected. The increase in the bias voltage does not affect the measured current.

In the next region if the voltage is increased the current increases too, due to a strong electric field that can accelerate electrons to energies where they can ionize the gas molecules themselves, called secondary ionization. These secondary electrons can also be accelerated and produce further ionization, in a process named multiplication (or amplification), which will be explained in Sec. 2.1.3. In this region, the signal output is proportional to the applied voltage, hence this region is known as **proportional region**.

Right after the proportional region is the **limited proportionality region**, where the multiplication is large enough making that the electric field is distorted near the anode due to a space charge resulting in a loss of proportionality.

In **Geiger-Mueller region**, the energy of the particle is not important because the electric field there has high values generating various avalanches that result in a large number of charge pairs giving a saturated current, with the same pulse height independently of the primary particle energy. Geiger-Muller is an excellent counter although it can not distinguish between two different energies.

The last region is known as **continuous discharge** making the detector insensitive to any radiation, thus this region is avoided in gaseous detectors.

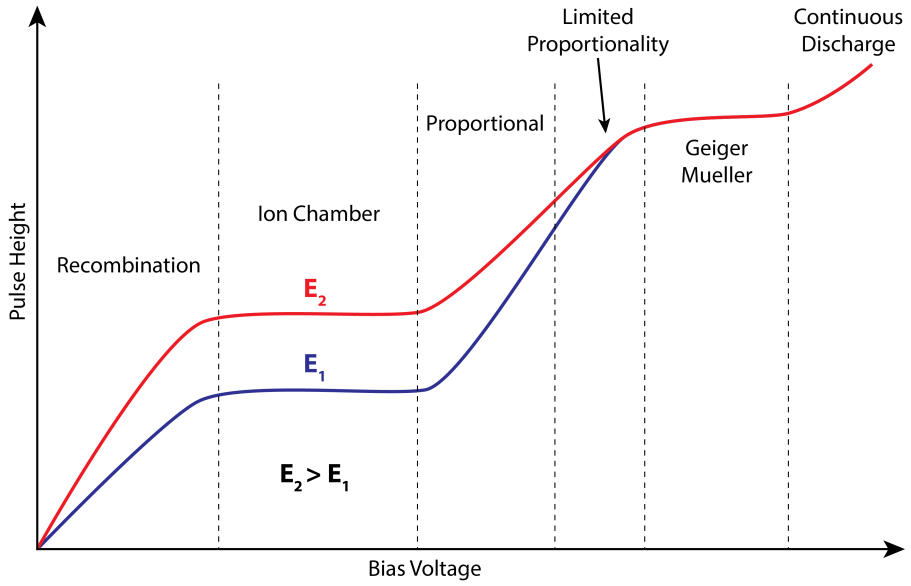

Figure 2.3: Regions of operation in gaseous detectors showing the charged collected versus the applied field. Adapted from [22].

2.2 Micro-Pattern Gaseous Detectors

Micro-Pattern Gaseous Detectors (MPGD) is a type of gaseous detector with small structures that emerged in the 90s. This new generation of detectors was employed using modern photo-lithographic technology.

2.2.1 Micro-Strip Gas Counter

The device micro-strip gas counter (MSGC) is considered the first MPGD proposed by Oed in 1988 [37]. This structure consists of alternated cathode and anode strips, with a typical pitch of $200-400\,\mu\mathrm{m}$ deposited on a dielectric substrate by a lithographic method. The thickness of the anode strips is kept small to ensure that the electric field is high. In Figure 2.4 it is shown a close view of the alternating anode with $10\,\mu\mathrm{m}$ wide and strips at $200\,\mu\mathrm{m}$ pitch.

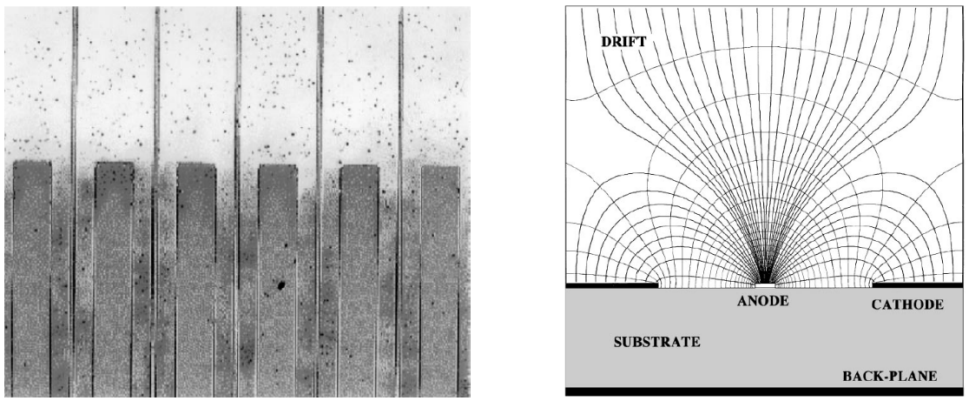

Figure 2.4: Left: MSGC plate with alternating anodes and cathode strips. Right: Electric field in the strips. Figures from [38].

2.2.2 Micromegas

In 1996 it was proposed a new type of high-granularity position-sensitive gaseous detector, called Micromegas [39]. It is a thin parallel-plate avalanche counter[1] consisting of a drift region and a narrow amplification gap ($25-150\,\mu\mathrm{m}$). A thin metal grid (micromesh) splits the gas volume in two regions, the amplification gap and the drift gap [40, 17]. In the drift region, electrons drift in a moderate electric field, however, in the avalanche region the electric field is much higher. A schematic drawing is shown in Figure 2.5.

[1]The parallel plate avalanche counter consists of two parallel plate electrodes separated by a small gap. It is filled with a proportional gas to induce an avalanche from the electrons and ions left by a particle that traverses the gap [24].

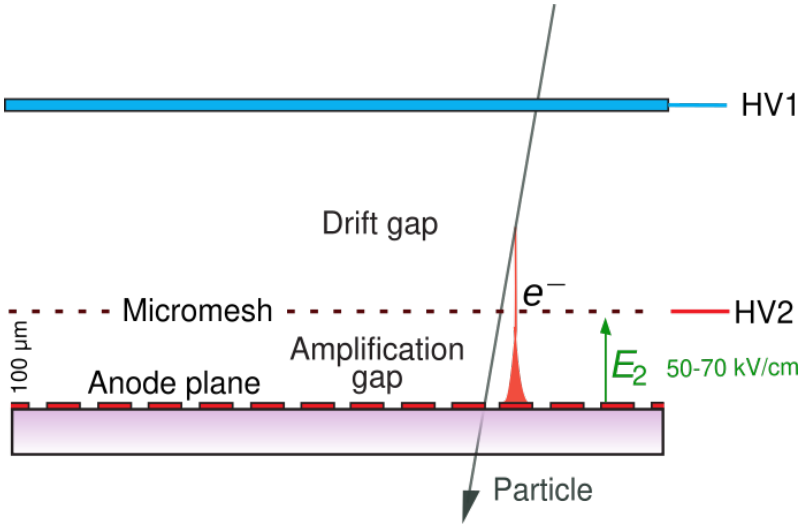

Figure 2.5: Micromegas sketch. Adapted from [17].

2.2.3 Gas Electron Multiplier

This detection structure was created by Fabio Sauli in 1997 [41] and has been used in many particle physics experiments, such as ALICE [42], CMS [43] and COMPASS [44].

The geometry of a 'standard GEM' manufactured at CERN has a set of holes arranged in a triangular pattern with $140\,\mu\mathrm{m}$ pitch and holes with $70\,\mu\mathrm{m}$ diameter, etched on $50\,\mu\mathrm{m}$ copper-clad Kapton™, as can be seen in Figure 2.6a. The hole has a characteristic double conical shape with an inner diameter of $50\,\mu\mathrm{m}$, shown in Figure 2.6b. The first GEM electrodes manufactured at CERN had an active area of $25 \times 25\,\mathrm{mm}^2$ on a $50\,\mu\mathrm{m}$ thick, copper-coated polymer foil [45].

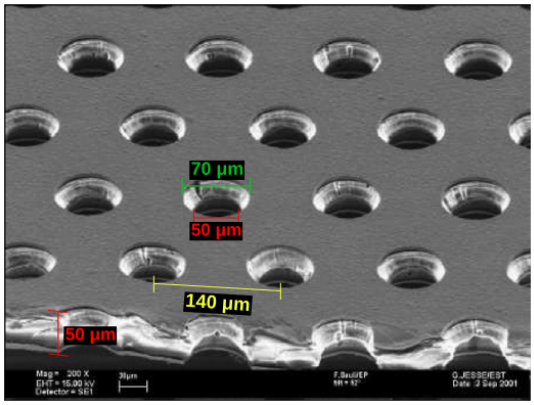

(a) Standard GEM foil seen through an electron microscope. Adapted from [46].

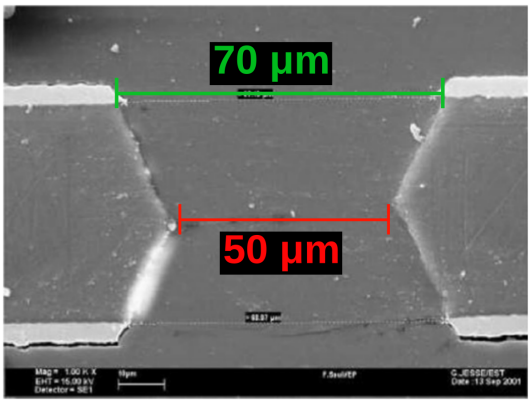

(b) Cross section through a GEM hole. Image from [46].

Figure 2.6: GEM foil structure.

Applying a high voltage between the copper layers an intense electric field is created inside the holes that act as an independent proportional counter. Due to the high electric field when electrons enter a hole it can be multiplied generating an avalanche

phenomenon. Thus, the GEM foil acts as a charge preamplifier, multiplying the electrons and transferring them to the lower region [38], as in Figure 2.7.

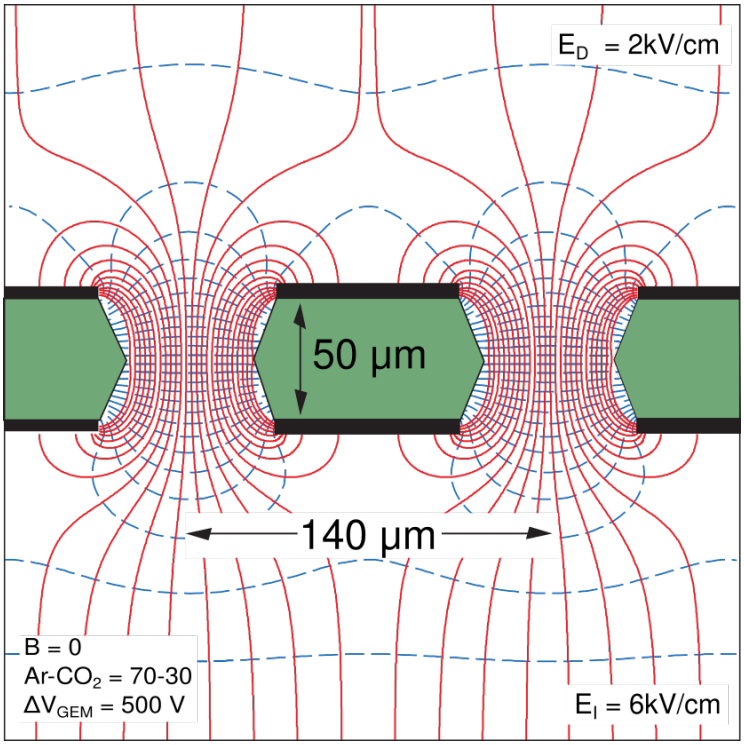

Figure 2.7: GEM amplification cell with typical dimensions. The electric field near GEM holes is represented in solid red lines and equipotentials in dashed blue lines. Adapted from [17] and [47].

This structure allows the transmission of charge, with the possibility to cascade several GEMs in a manner to obtain an even higher gain. With triple-GEM is possible to obtain gains of 10^5 depending on the gas mixture [48].

Figure 2.8 shows the main aspects of a generic triple-GEM detector. The cathode can be used as a neutron converter, for instance, a thin boron film could be coated on the cathode [49]. The detector geometry can be divided into 3 regions: drift, transfer, and induction. The drift region is where the primary ionization occurs. The electrons released in this region drift to the GEM holes where occurs charge multiplication. These secondary electrons are then transferred to the next GEM foil in the transfer region. In the last transfer, the secondary electrons enter the induction region and then are collected at the readout board. The readout stage permits spatial resolution approaching a few micrometers [24].

The gain in a GEM detector can be given in terms of an *effective gain*, which is defined as the ratio between the amount of charge recorded on the readout electrode and the number of primary charges [50]. The effective gain is always lower than the *real gain* because some electrons are lost on the bottom GEM electrode [45, 47].

Several aspects determine the gain of the GEM structure, for instance: the hole diameter, the gas composition as well as its pressure and temperature. Investigations of many geometries conclude that the gain is higher when an aspect ratio of the hole diameter over foil thickness is close to unity [47], as shown in Figure 2.9.

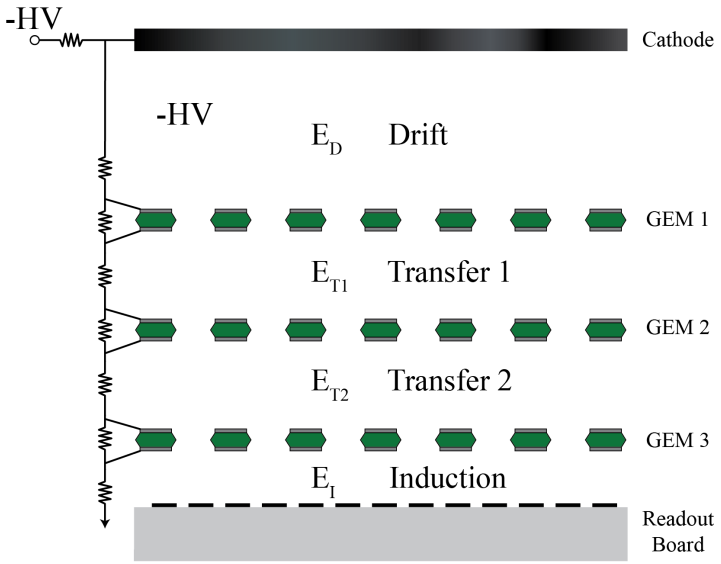

Figure 2.8: Sketch of a Triple-GEM detector. Adapted from [45].

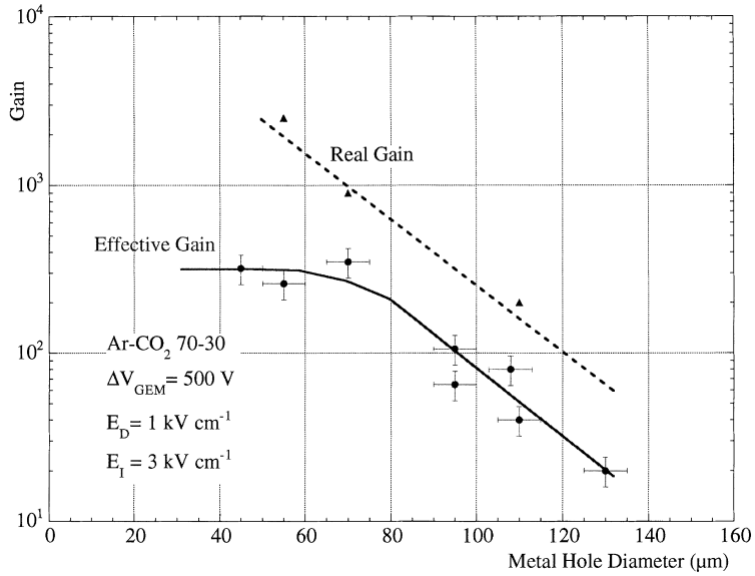

Figure 2.9: Real and effective gain of GEM foils as a function of diameter. Image from [47].

In Figure 2.10 the effects on the gain are shown when changing the gas mixture. In this particular case, the concentration of Ar-CO_2 mixture is changed in order to optimize the gain.

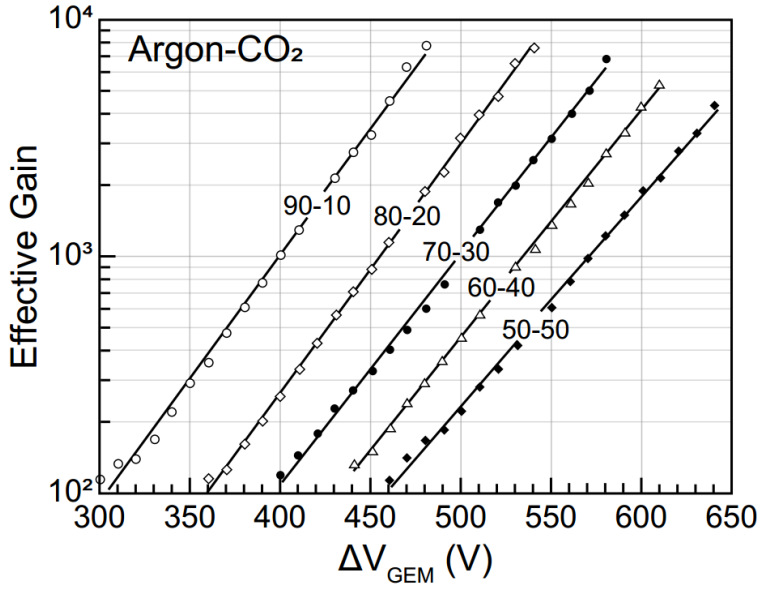

Figure 2.10: Effective gain of a single GEM foil as a function of voltage for different gas mixtures. Adapted from [45].

2.3 Characterizing a Position-Sensitive Detector

Several features characterize the performance of a position-sensitive radiation detector. The device's capability to measure radiation and the position where it interacted with the detector are key elements that must be evaluated in order to decide its possible applications. In the next sections, these features will be presented and discussed.

2.3.1 Spatial Resolution

The spatial resolution is a parameter that measures how good the system is to distinguish two closely spaced measurements in space [22]. The clarity of information in an image is a measurement of how well the image reveals the fine structure of the object [51]. The position resolution is closely related to the width of the different spread functions, which will be discussed here.

Suppose a point-like object whose image is recorded by a detector. Due to the limitations in the detection, this object will be recorded as a round shape with high intensity in the middle that decreases moving away from the center. With respect to any coordinate, the plot of this intensity will be represented by a Gaussian-like distribution. This distribution is the Point Spread Function (PSF).

Now, suppose that two of these point-like objects are moving close to each other. The detector is able to distinguish these objects when the distance between them is equal to or larger than one full width at half maximum (FWHM). Figure 2.11 shows the minimum distance where the detector is able to distinguish two of these points.

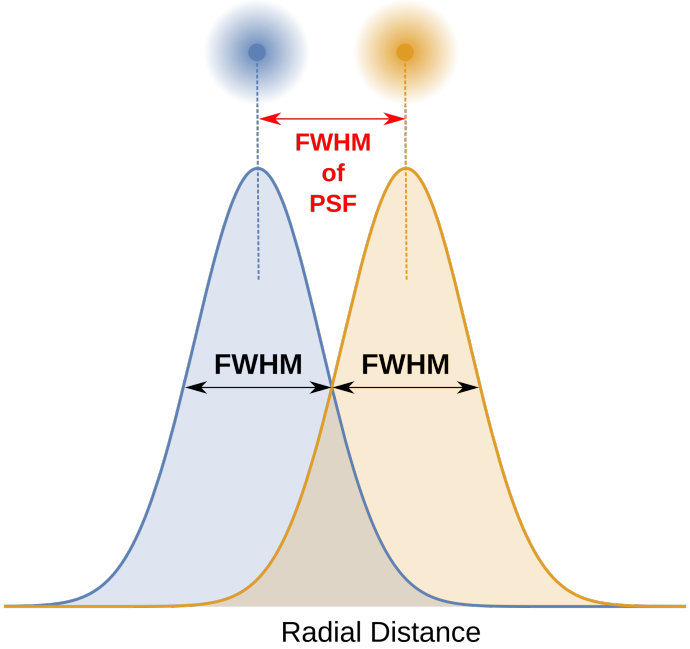

Figure 2.11: PSF of two points that are one FWHM distance apart. Adapted from [22].

As the spatial resolution is dependent on the value of the FWHM and the PSF is characterized by a Gaussian distribution, it is important to understand how to extract this information from a Gaussian distribution:

$$f(x) = \frac{1}{\sqrt{2\pi\sigma^2}} \exp\left[\frac{-(x-x_0)^2}{2\sigma^2}\right], \tag{2.18}$$

where σ is the standard deviation and x_0 is the center of the function. The FWHM is defined as

$$\begin{aligned} \text{FWHM} &= 2\sigma\sqrt{2\ln(2)}, \\ \text{FWHM} &\approx 2.355\sigma. \end{aligned} \tag{2.19}$$

This simple theoretical way to describe the spatial resolution is experimentally impractical because an infinitesimal point-like object is not possible to create. However, a point-like can be obtained approximately through a small hole or using derived functions, such as Line Spread Function or Edge Spread Function.

The Line Spread Function (LSF) is connected to the PSF via integration over one dimension

$$\text{LSF}(x) = \int_{-\infty}^{+\infty} \text{PSF}(x,y)dy. \tag{2.20}$$

The line consists of a large number of closely spaced points, given a profile of FWHMs. This method is also difficult to determine experimentally because it is difficult to create an ideal line object, as represented in Figure 2.12.

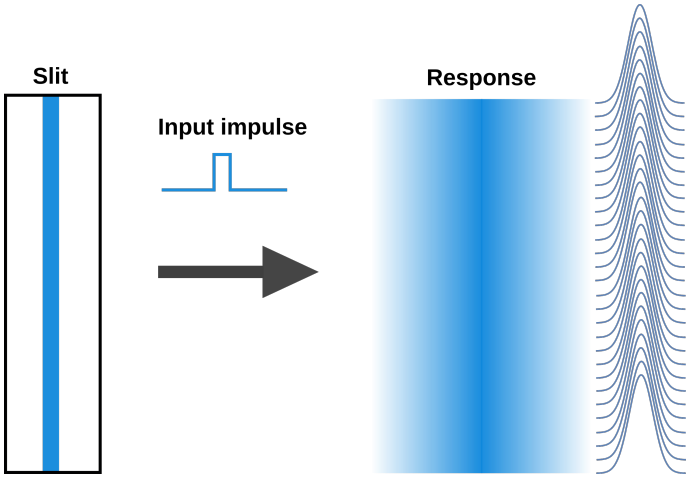

Figure 2.12: LSF can be considered a large number of closely spaced points in a line. Adapted from [22]

The Edge Spread Function (ESF) is a convenient way to determine the system resolution since LSF does not offer a practical way to determine the resolution. Any rectangular object can be used to apply this method since it offers an ideal step function, as represented in Figure 2.13. Integrating the LSF one can obtain the ESF [22]:

$$\mathrm{ESF}(x) = \int_{x'=-\infty}^{x} \mathrm{LSF}(x')dx'. \tag{2.21}$$

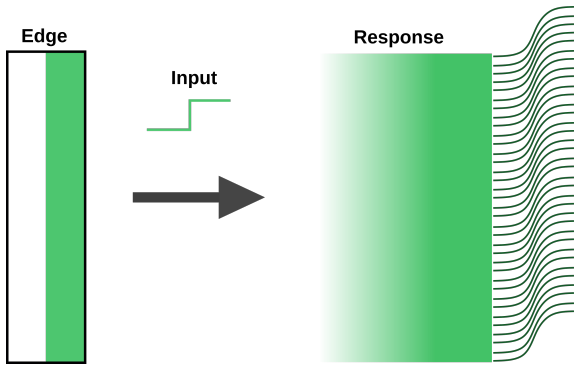

Figure 2.13: ESF obtained from a rectangular object. Adapted from [22].

The FWHM can be extracted using the *erf* function (also known as error function) which is used to fit the ESF:

$$\mathrm{erf}(p) = \frac{2}{\sqrt{\pi}} \int_0^p e^{-t^2} dt \tag{2.22}$$

where $p(x)$ is connected with the parameters of the PSF and defined as

$$p(x) = \frac{x - \mu}{\sigma\sqrt{2}}, \tag{2.23}$$

such that the resolution is given as in the PSF case in Eq. 2.19.

Summary

This chapter presented basic processes in gaseous detectors such as gas ionization, the drift and diffusion of electrons in this media as well as charge amplification. It introduced some of the Micro-Pattern Gaseous Detectors with a focus on a special structure called GEM that is important for this work. In the following chapters, a detailed simulation of this kind of detector aiming to optimize a thermal neutron detection system will be exploited.

Chapter 3

Simulation Tools

In the context of the development and optimization of particle detectors, Monte Carlo simulation is an essential tool to study the detector response in various conditions, with different particles and configurations without the cost of building a prototype. Each step in the development can be modeled in order to understand the signal generated by the detector.

This work aims to simulate a thermal neutron detection system that converts these particles into charged ones that can be measured in a gaseous detector, specifically the GEM-based detector. Therefore, the sequence of the simulation work is:

1. Generation and transport of neutrons inside the detector;
2. Simulation of the nuclear interaction between a neutron and a converter layer. In this dissertation, the converter layer is the boron-10;
3. Transport of the reaction products inside the converter layer;
4. Transport of the reaction products inside the gaseous media giving rise to ionization;
5. Drift of electrons and ions released in the ionization towards the anode and cathode, respectively, and
6. Charge distribution at the readout plane.

3.1 Primary Particle and Non-Gaseous Interactions

Steps 1, 2, and 3 can be understood as the primary particle generation (thermal neutrons) and its interactions with non-gaseous detector material. A well-established tool for this purpose is the GEANT4 [6], which is an acronym for "GEometry ANd Tracking", used to simulate the passage of particles through matter using Monte Carlo methods. GEANT4 is an object-oriented library programmed in C++, developed and maintained by CERN. Its areas of application include high energy, nuclear, and accelerator physics, as well as studies in medical and space science [6].

The GEANT4 has several features that aim to guarantee a good simulation of most diverse physical phenomena providing a range of facilities to the user such as the manipulation of geometry, tracking, detector response, run management, visualization, and user interface.

3.1.1 Geometry Definition

First of all, it is necessary to create a geometry where the particles will be transported. It starts in GEANT4 with the definition of a *solid volume*, defining the shape of the volume. By means of Boolean operations, 22 types of shapes (i.e. box, sphere, cylinder, etc) can model complex geometries.

Materials of any type can be chosen from a list or they can be user-specified, including isotopes, molecules, and compounds to be assigned to a given *solid volume* that is called *logic volume* in GEANT4.

The last step in the construction of a geometry is the positioning of this solid in the simulation *world*, defining a *physical volume.*

3.1.2 Physics Processes

The physics processes describe how particles interact with a material. In GEANT4, there are seven major categories of processes [52]:

1. electromagnetic,
2. hadronic,
3. decay,
4. photolepton-hadron,
5. optical,
6. parameterization, and
7. transportation.

There are a set of models to simulate the physics process and the choice depends on the user's needs. For instance, there are two packages for electromagnetic interactions of charged particles and photons with matter: "Standard EM" and "Low Energy EM". The choice between them depends on the energy of the secondaries. In the "Standard EM" only secondaries with energy above $1\,\mathrm{keV}$ are prioritized. When the secondary energy is below $1\,\mathrm{keV}$ other effects are important such as atomic relaxation and shell effects, which are provided by the "Low Energy EM" package.

In this work, the physics model QGSP_BERT_HP has been chosen since it is recommended by the GEANT4-collaboration for most low energy applications including the transport of low energy neutrons down to thermal energies [53]. The QGS stands for *quark-gluon string*, which describes the interaction which uses the quark-gluon string model [54] for high energies. P means that a *precompound* model handles the nuclear de-excitation when a high energy interaction creates an excited nucleus. BERT stands for *Bertini intra-nuclear cascade model* [55, 56] for hadrons with energy below $10\,\mathrm{GeV}$. And HP is an indication of a *high precision* model in neutron transport. This high precision model uses a highly accurate cross section for reactions like elastic and inelastic scattering, capture, and fission for neutrons with energy below $20\,\mathrm{MeV}$ down to thermal energies, and his data come from many releases of *evaluated nuclear data files* (ENDF).

The ENDF system was developed for the storage and retrieval of evaluated (i.e. recommended) nuclear data to be used for applications of nuclear technology [57]. The data stored are essentially nuclear reaction cross section together with the distribution in energy and angle of the secondary reaction products [52]. Among many maintained data bases, some was converted to GEANT4 format (e.g. ENDF/B-VII.1, JEFF-3.3, JENDL-4.0, etc) [58, 59, 60].

3.1.3 Primary Particle

After the definition of geometry and all physical processes that will define the particle behavior, it is necessary to define a source of primary particles. For each event in GEANT4, a primary particle is defined with its position, direction, and energy. This work used neutrons with thermal energy of $41.8\,\mathrm{meV}$.

3.2 Gaseous Interaction

Concerning steps 4, 5, and 6, a powerful tool capable to accomplish the requisites is the Garfield++, object-oriented libraries used for a detailed simulation of particle detectors based on ionization measurements in gases and semiconductors [7].

3.2.1 Geometry and Fields

The geometry as well as the electrostatic field configurations are provided to Garfield++ via two other software packages: Gmsh [61] and Elmer [62].

Gmsh is a three-dimensional finite element mesh generator with a built-in CAD engine and post-processor, modeling a 3D geometry of the detector creating a finite-element field map. Basically, the Gmsh tool splits the geometry into small elements where it is possible to apply the finite element method to calculate the electric fields. Figure 3.1 shows a sample of the detector cell by the finite element method.

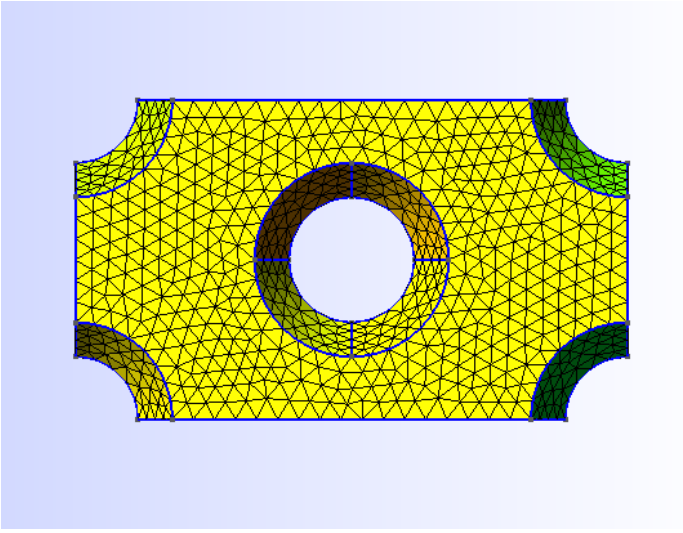

Figure 3.1: Sample of the detector cell represented by the finite element method.

Elmer is a finite element method solver for multi-physics problems like fluid dynamics, structural mechanics, electromagnetics, heat transfer and acoustics. After the geometry creation in Gmsh, Elmer solves the differential equations respecting the boundary conditions and the materials assigned by the user in the simulation.

The application of the finite element methods to problems with boundary conditions results in a set of linear equations as:

$$[K] \cdot \{u\} = \{F\}, \tag{3.1}$$

where $[K]$, $\{u\}$, and $\{F\}$ are, respectively, the matrix representing the properties of the problem, the unknown value, and the forces. In this work, $[K]$, $\{u\}$, are the electrical permittivity, and the electrical potential, respectively [63]. In case the $[K]$ matrix has an inverse, the solution for the problem is

$$\{u\} = [K]^{-1}\{F\}. \tag{3.2}$$

Thus, in an electrostatic problem, the Laplace equation must be solved:

$$\nabla^2\phi = \frac{\partial^2\phi}{\partial x^2} + \frac{\partial^2\phi}{\partial y^2} + \frac{\partial^2\phi}{\partial z^2} = 0. \tag{3.3}$$

And the electric field can be obtained in the whole space by:

$$E = -\nabla\phi. \tag{3.4}$$

3.2.2 Microscopic tracking for electrons

The first-order equation of motion:

$$\dot{\mathbf{r}} = \mathbf{v}_d\left(\mathbf{E}(\mathbf{r}), \mathbf{B}(\mathbf{r})\right) \tag{3.5}$$

is solved by means o Runge-Kutta integration in Garfield++. This method is suited for tracking electrons over large distances (e. g. TPC) or where the transverse diffusion does not have a significant impact on the signal (e. g. drift tubes). The drawback is that stochastic variations of drift paths are not taken into account.

On a microscopic level (characteristic dimensions of the electron mean free path, on the second-order equation of motion), Garfield++ employs the transport of electrons based on the algorithm used in Magboltz [64] for an accurate simulation of the trajectories. Magboltz solves the Boltzmann transport equations for electrons in gases with an applied electromagnetic field using semi-classical Monte Carlo simulation[65, 66].

In Figure 3.2 are shown electron trajectories calculated using microscopic tracking from Garfield++. This figure shows the positions of every 10^{th} electron collision in a GEM.

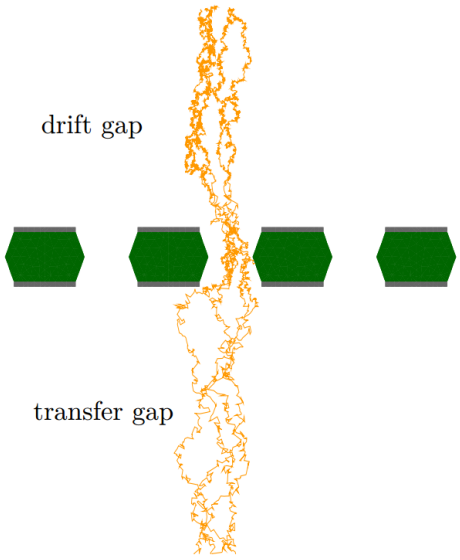

Figure 3.2: Microscopic tracking of electron trajectories in a GEM. From [64].

3.2.3 Ionization Pattern

The simulation of the ionization pattern generated by low energy ions is produced in Garfield++ through an interface with SRIM [25]. The toolkit SRIM is a program for simulating the energy loss of ions in matter producing tables of stopping power, range, and straggling parameters.

The tables generated with the SRIM are imported in Garfield++ through the class `TrackSrim`. This class generates tracks that reproduce the average quantities obtained by SRIM. The track is initiated with the energy set by the user and iteratively [7]:

- computes the energy loss per unit length at the current energy,
- determines the length of the step where the particle will produce a certain number of electrons,
- updates the trajectory given the particle energy,
- randomizes actual electromagnetic energy loss over the step and updates the energy.

As long as the particle has any energy left the above steps are repeated.

3.3 CPU-Time consuming in gaseous detector simulation

As already mentioned, the software Garfield++ is well suited for gaseous simulations due to its very detailed simulation of electrons propagation in the gas medium, its interactions, as well as the avalanche formation. However, all this has a cost on CPU processing time. In Figure 3.3 is shown the electronic avalanche calculated in Garfield++. All these lines are under microscopic tracking which makes the process very slow and all these interactions demand a lot of computational time making it a barrier to use this tool.

In the literature, it is found some parameterizations and manners to speed up the simulations in Garfield++ (through parameterizations or parallelism) as in [67, 68, 69]. In [67] it is mentioned that in the high energy simulation of a triple-GEM the CPU time can spend 20 hours per event, while in [68] the time needed to one single track on a standard distributed computing farm can spend around one day.

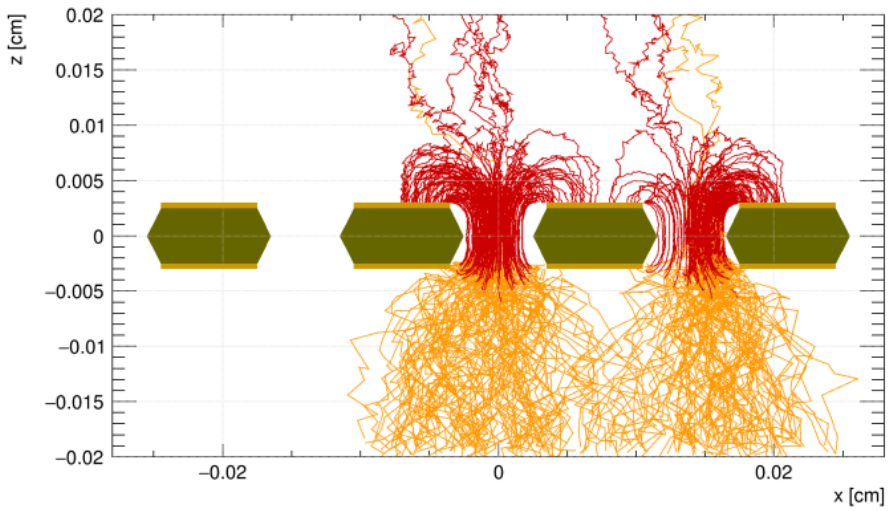

Figure 3.3: Electronic avalanche calculated in Garfield++. The orange lines are the electron drift path and the red lines ion drift path. Figure from [70].

In the case of neutron detectors, the reaction products from $^{10}\mathrm{B}(n,\alpha)^{7}\mathrm{Li}$ has a high ionizing power leading to a large number of electrons that needs to be considered in the avalanche calculations. This also leads to very time consuming CPU calculations and becomes impossible even in a cluster of computers to do these simulations. Considering this fact, the reduction in processing time by several orders of magnitude is crucial for a substantial study with enough statistics.

3.4 Summary

This chapter described the simulation tools and the steps used in this work to build a simulation concerning neutron detection with gaseous detectors. The time consuming of these tools is a problem that needs to be solved. In this context, an optimized simulation tool is required, which leads to the next chapter with the development of a parameterized simulation tool that combines GEANT4 and Garfield++.

Chapter 4

Fast Simulator

A complete simulation of a gaseous neutron detector using the $^{10}\mathrm{B}(n,\alpha)^{7}\mathrm{Li}$ reaction is very time consuming due to the high ionizing power of these products. The high number of electron trajectories that need to be simulated makes it impossible to properly evaluate the detector response. Thus, in this chapter, a fast simulator developed in this work will be presented aiming for a more efficient way to simulate this kind of detector that uses a parameterization of the charge deposited at the detector's readout plane. Figure 4.1 shows a schematic view of the simulation chain of the fast simulator.

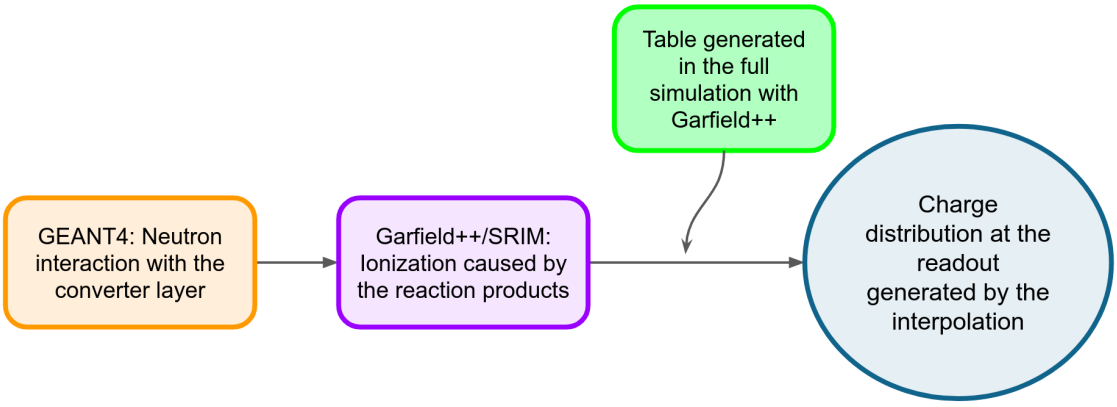

Figure 4.1: Simplified simulation chain of the fast simulator.

The simulation chain consists of a series of full simulations developed in Garfield++ with the tracking and subsequent avalanche of electrons starting in eight different points inside the drift region, this step is shown in the green box in Figure 4.1. These points were chosen in order to cover a range of possibilities in the charge distribution at the readout plane. The tracking continues until the secondary electrons reach the readout plane. In the readout plane their positions are saved, building a charge distribution to a given starting point in the drift region. For all these eight full simulations, parameters from a double Gaussian fit to the charge distribution in the readout plane are obtained and saved into a table that will be used in a future step.

The orange box in Figure 4.1 represents the development of the nuclear interaction of the thermal neutron with the converter layer in GEANT4. From this interaction, the position and momentum of the reaction products are saved when they cross the boundary

between the converter layer and the gaseous media towards the readout plane (i.e. only particles with a real possibility to trigger the detector and give rise to a measurable signal). At this stage, the saved data is used as input in Garfield++.

Then, the ionization pattern is generated through an interface with the code SRIM, which needs to be previously used to generate ionization tables, shown in the purple box in Figure 4.1. At this point, it is inserted into the fast simulator the lookup table created previously from the full simulations in Garfield++ (green box).

Finally, the charge distribution at the readout plane due to the electrons is given by the interpolation of the parameters from the lookup table depending on its position inside the drift region, shown in the blue box in Figure 4.1. All these steps will be described in detail in the following sections, and a complete flowchart of the simulation is shown in Figure 4.2.

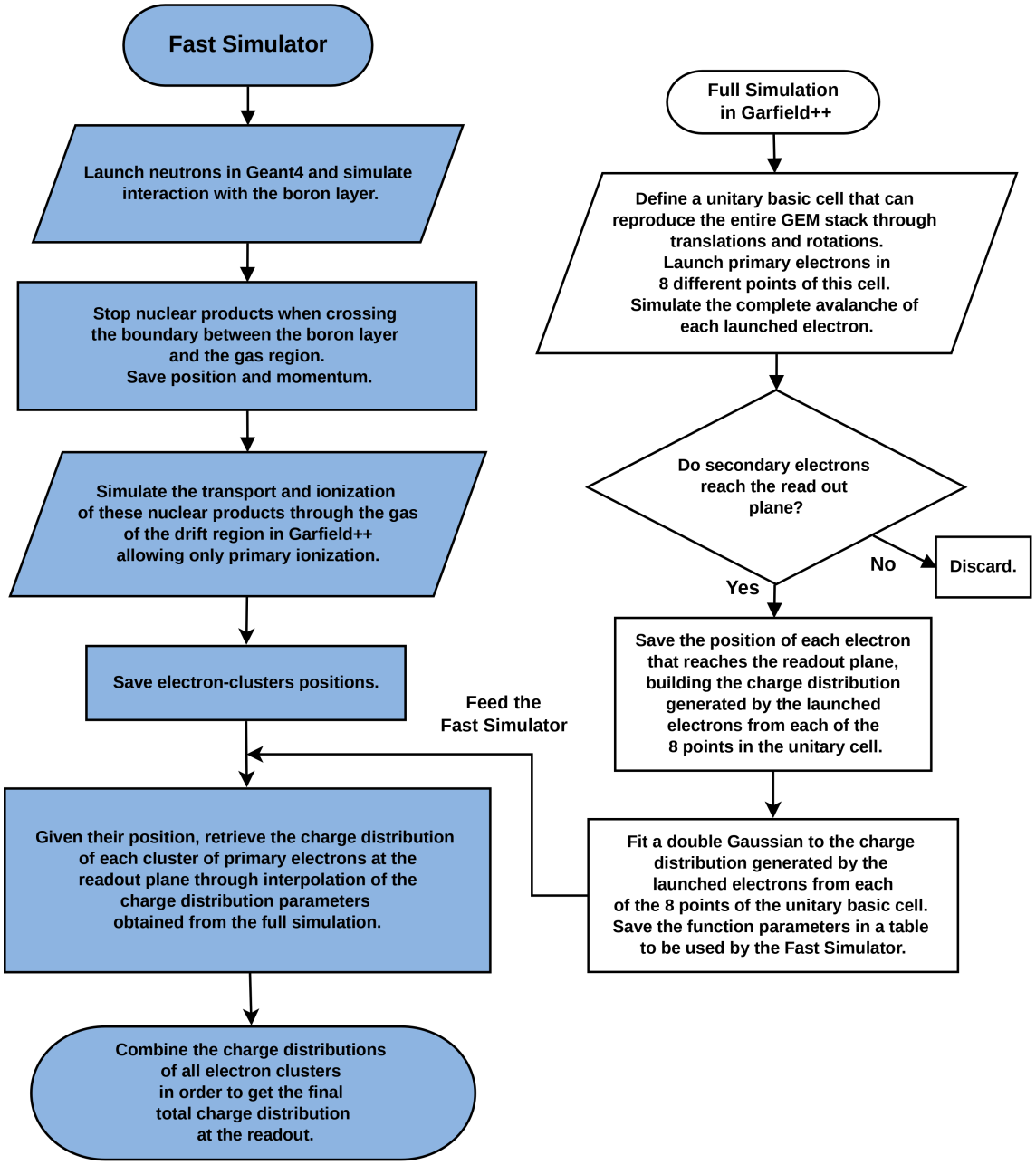

Figure 4.2: Fast simulator diagram flow.

4.1 Full Simulation in Garfield++

The fast simulator needs a first step in which a series of full simulations is crucial to generate a table containing the parameters that will be used to evaluate the final charge distribution at the readout plane.

As the GEM foil has a symmetry, as shown in Figure 4.3a, it is possible to define an area, named here as *unitary basic cell* as represented in Figure 4.3b.

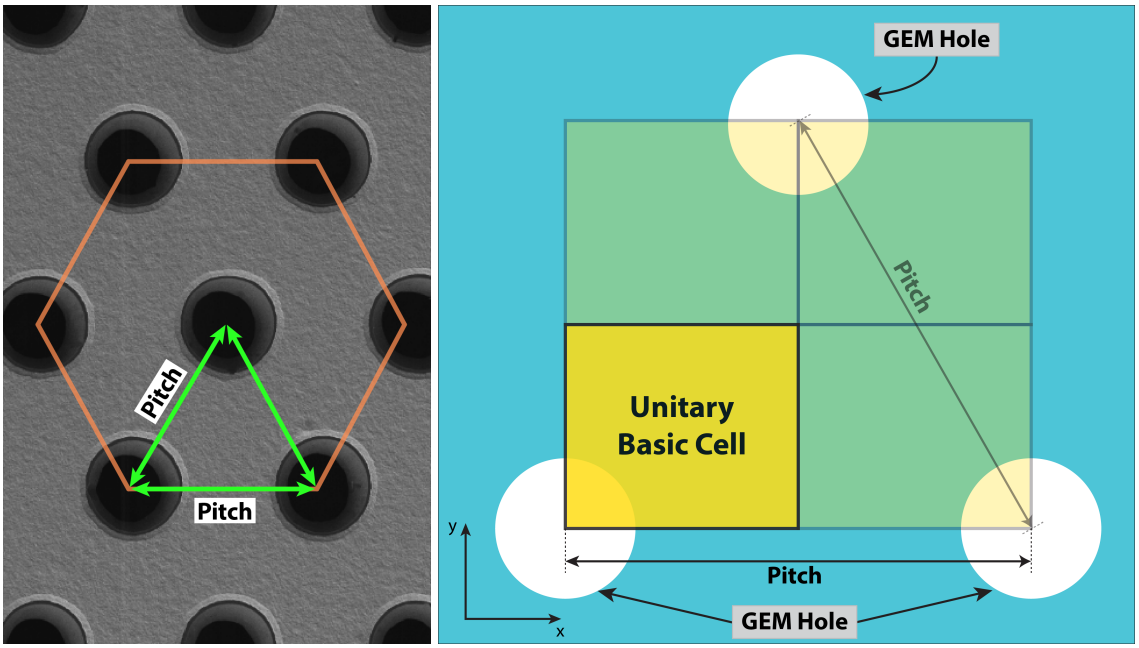

(a) GEM symmetry, adapted from [71].

(b) Unitary basic cell.

Figure 4.3: Parameterization strategies.

Figure 4.4 represents the necessary rotations and translations to build the entire GEM plane using this unitary basic cell. The letter R inside each cell is an illustration of the rotations and translations applied in each one. The rotations of the cell represented by the color red can compose entire GEM holes (cells indicated by the color blue, yellow and green) and these four cells can be translated along the GEM plane in order to build the entire foil.

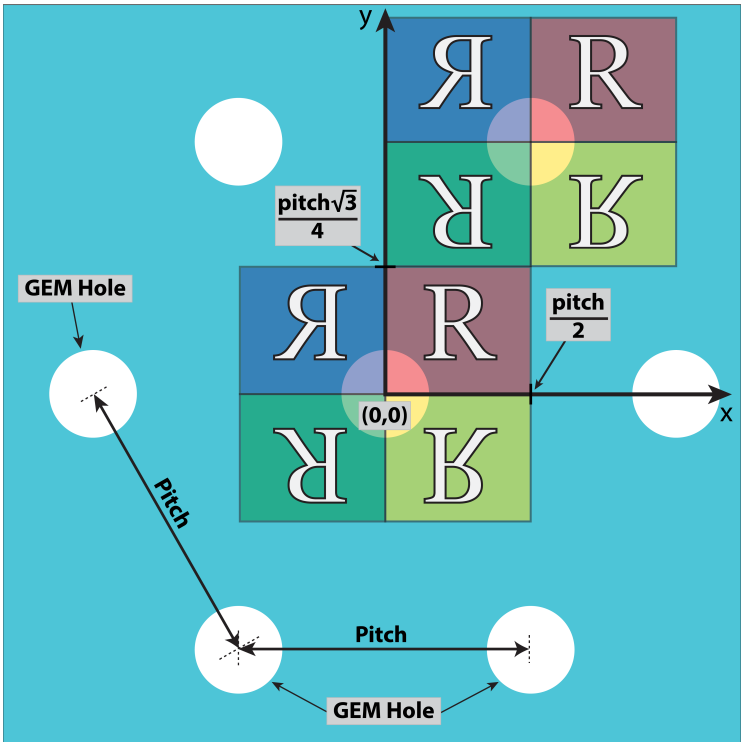

Figure 4.4: Strategy applied to obtain the entire map of the GEM foil.

The size of the unitary basic cell is defined by the pitch of the GEM foil. Considering the x-y axis as in Figure 4.4, the limits of the unitary basic cell is:

$$0 \leq x \leq \frac{\text{pitch}}{2} \quad \text{and}$$
$$0 \leq y \leq \frac{\text{pitch}\sqrt{3}}{4}.$$

All the fast simulator parameterization is based on the unitary basic cell, therefore an electron that is outside the limits of this cell needs to be virtually taken to the unitary basic cell to obtain the corresponding charge distribution and transported back to the original position taking the information of its charge distribution. In order to accomplish this, a global and local coordinate system was defined such that the global coordinate system is denoted by xy and represents the position of the electron at any point in the detector. The local coordinate system is denoted by $x'y'$ and represents the position of the electron in the unitary basic cell. The relation between xy and $x'y'$ coordinate systems are:

$$x' = \begin{cases} |x| - \frac{\text{pitch}}{2} \cdot \left\lfloor \frac{2\lfloor|x|\rfloor}{\text{pitch}} \right\rfloor & \text{if } \left\lfloor \frac{2\lfloor|x|\rfloor}{\text{pitch}} \right\rfloor \text{ is even} \\ -|x| + \frac{\text{pitch}}{2} \cdot \left(\left\lfloor \frac{2\lfloor|x|\rfloor}{\text{pitch}} \right\rfloor + 1 \right) & \text{if } \left\lfloor \frac{2\lfloor|x|\rfloor}{\text{pitch}} \right\rfloor \text{ is odd} \end{cases} \tag{4.1}$$

$$y' = \begin{cases} |y| - \frac{\text{pitch}\sqrt{3}}{4} \cdot \left\lfloor \frac{4\lfloor|y|\rfloor}{\text{pitch}\sqrt{3}} \right\rfloor & \text{if } \left\lfloor \frac{4\lfloor|y|\rfloor}{\text{pitch}\sqrt{3}} \right\rfloor \text{ is even} \\ -|y| + \frac{\text{pitch}}{2} \cdot \left(\left\lfloor \frac{2\lfloor|y|\rfloor}{\text{pitch}} \right\rfloor + 1 \right) & \text{if } \left\lfloor \frac{2\lfloor|y|\rfloor}{\text{pitch}} \right\rfloor \text{ is odd} \end{cases} \tag{4.2}$$

The relation between the global and local coordinate for a GEM with a pitch of $140\,\mu\mathrm{m}$ is shown in Figure 4.5.

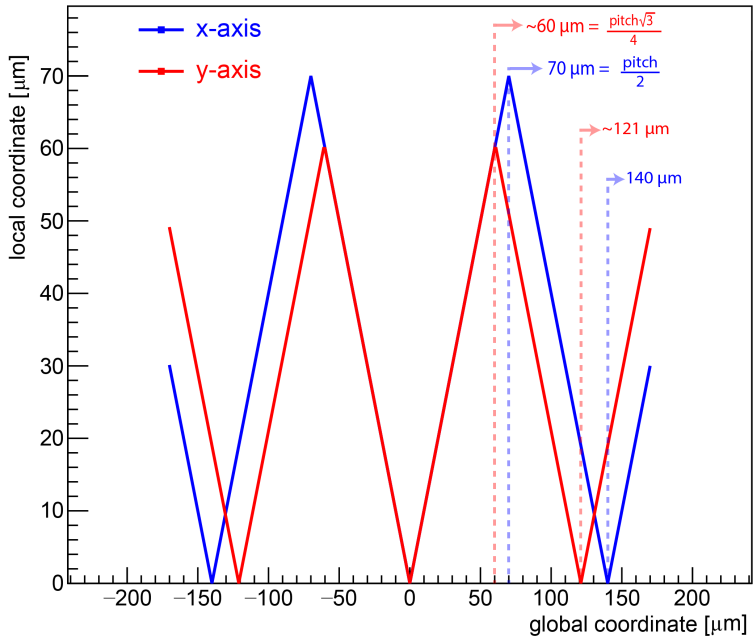

Figure 4.5: Global and local coordinate for a GEM with a pitch of $140\,\mu\mathrm{m}$. The blue and red lines represent the x-axis and y-axis, respectively.

A series of full simulations of electron trajectory is performed with 8 different initial points in the drift region. These points were selected to be key points within a unitary cell that allow a complete representation of any charge distribution since they reproduce the different conditions expected in this region of the detector. The starting points for the full simulation are shown in Figure 4.6 as four red circles and four green circles. The red ones belong to plane z_2, which is close to the cathode at the beginning of the drift path. The green ones belong to plane z_1, which is close to the GEM foil. Given that the electric field is different in those two planes of the z-axis, the box formed by the eight points tries to cover a range of possibilities in the charge distribution at the readout plane. Figure 4.7 shows an example of the full simulation of one electron propagating through the detector starting at the higher point in the drift region ($0.1\,\mathrm{cm}$) and drifting towards the two GEM foils and reaching the readout at $-0.2\,\mathrm{cm}$.

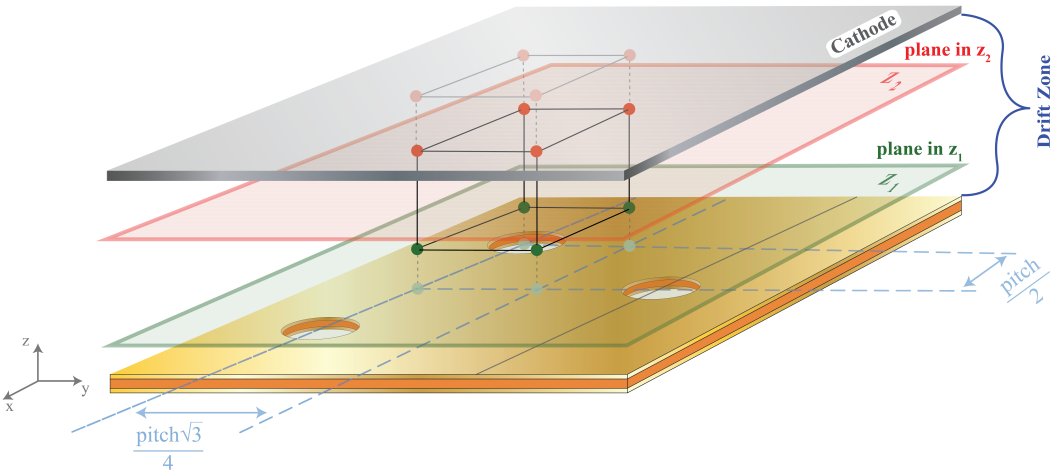

(a) Perspective view.

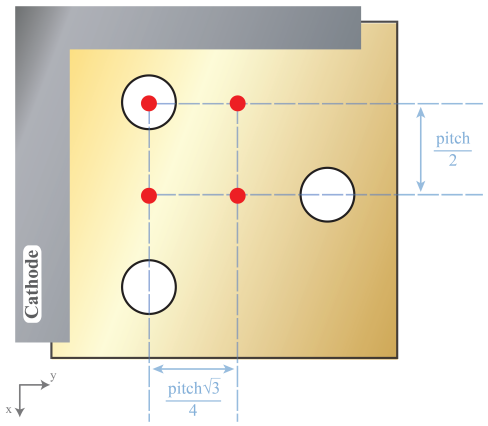

(b) Top view.

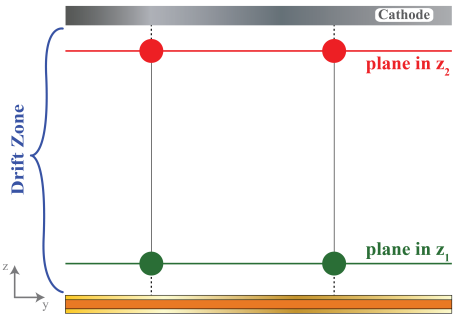

(c) Side view.

Figure 4.6: Sketch of the position of the eight starting points for a full simulation.

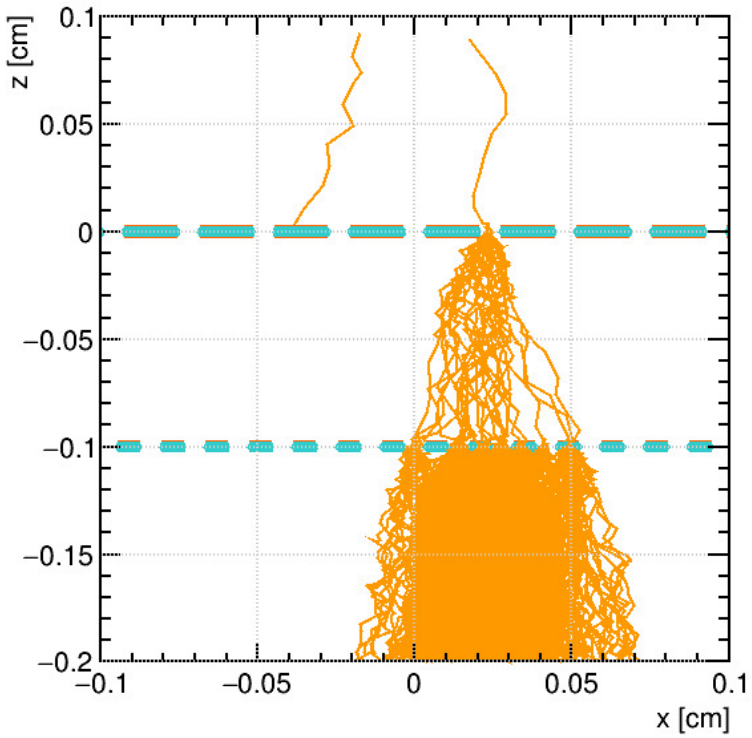

Figure 4.7: Avalanche produced by one electron.

The position in x-y is recorded for each electron that arrives at the readout plane, while those electrons that are stopped in the middle of the geometry are discarded. This results in the charge distribution at the readout plane for the full simulation can be parameterized using a double-Gaussian, as represented in Figure 4.8. When the charge is sharing two holes, i.e. many electrons are passing “equally” through two holes, the shape of the charge distribution cannot be a “perfect” Gaussian, but a Gaussian-like. Therefore, two Gaussian can better represent the charge distribution.

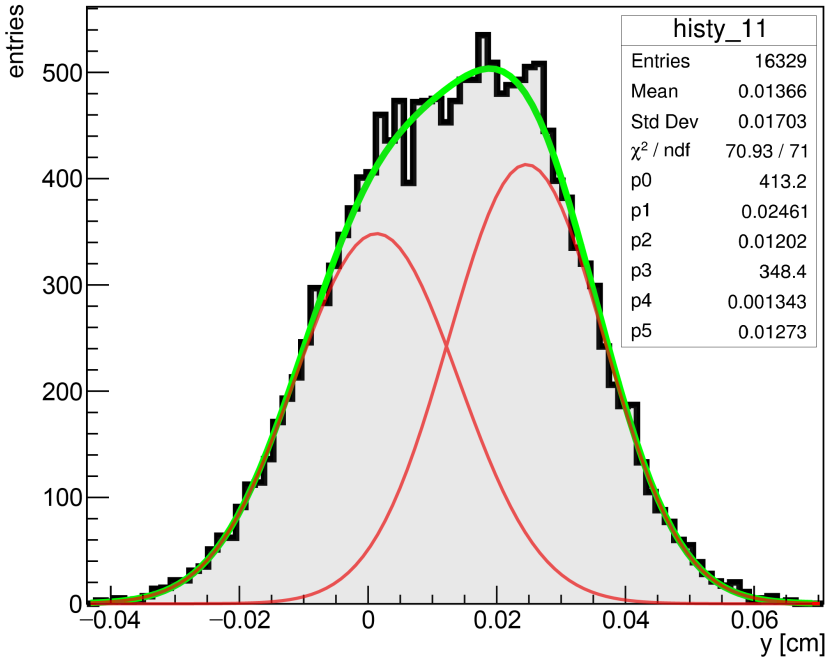

Figure 4.8: Charge distribution fitted by a double-Gaussian to one starting point from the drift region.

The goal with the full simulation in Garfield++ is to elaborate a *lookup table* where the parameters of the double-Gaussian fit are stored. The *lookup table* has the values of the fit for 8 points in the drift region, the points shown in red and green in Figure 4.6. Then, this *lookup table* is used to feed the fast simulator at a given point in order to interpolate the values of the parameters in that particular point.

4.2 Fast Simulator

The fast simulator is composed of isolated parts as sketched in Figure 4.1: the neutron interaction with the converter layer (orange in the sketch), the ionization caused by the reaction products (purple in the sketch), and the charge distribution at the readout (blue in the sketch) generated by the interpolation of the parameters stored in the lookup table (green in the sketch). The first step to accomplish an entire simulation in the fast simulator is the creation of a converter layer geometry in the GEANT4. Thus, the primary particles (thermal neutrons in this work) must be initialized followed by the simulation of the reaction of the neutrons with the converter layer material.

The reaction products created in the nuclear reaction are transported inside the converter layer until they reach the boundary with the gas medium (detection medium). When this condition has been achieved, the position and the momentum of the reaction products are saved together with the nature of the particle (α-particle or ^{7}Li) and the simulation process is interrupted because the drift of these particles continues in Garfield++.

In this step, the positions and momentum saved in GEANT4 are inserted as input, and the ionization pattern in the drift region is simulated using Garfield++ with its interface to SRIM [25]. The reaction products start in the boundary between the converter layer

and the gaseous media, but now the particles continue to travel inside the gas leading to ionization.

This interface between Garfield++ and SRIM requires a file previously created using SRIM with the following parameters [7]:

- a list of kinetic energies at which losses and straggling have been computed;
- average energy lost per unit distance due to electromagnetic and nuclear interaction;
- projected path length;
- longitudinal and transverse straggling.

In Garfield++ the energy loss in a single ionizing collision of the primary charged particle and the secondary electrons produced in this process are called a "cluster" [7]. Thus, the position of these clusters and the number of secondary electrons in each cluster are recorded. The result of this step is represented in Figure 4.9, where it is shown the clusters of electrons inside the drift region as a function of position, where each point has a certain number of electrons.

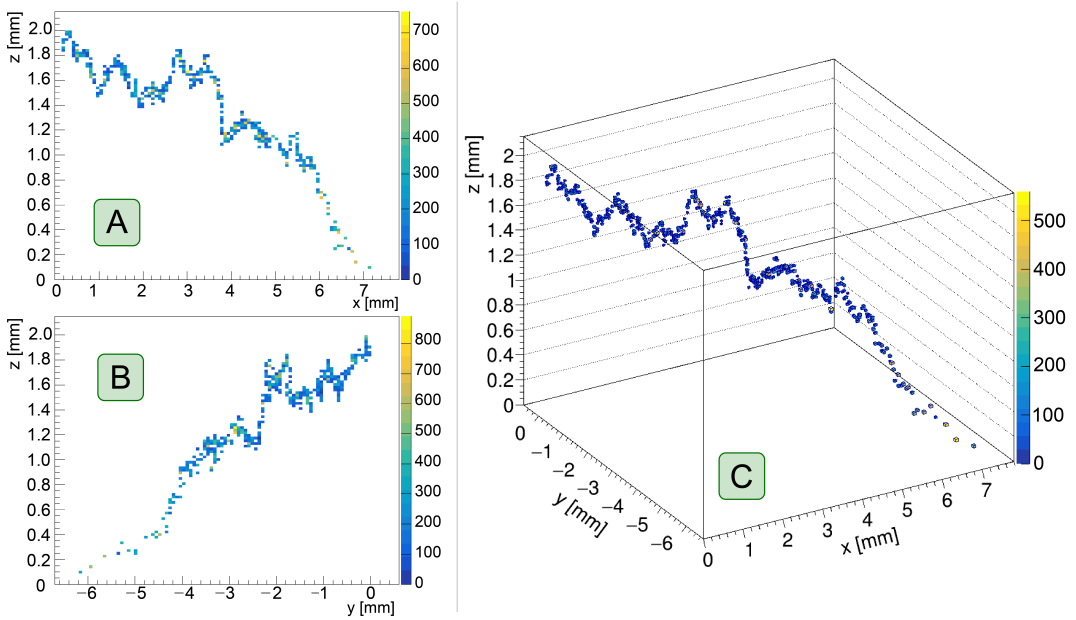

Figure 4.9: Ionization pattern due to an alpha particle in the drift region. The color indicates the number of electrons. The drift region has $2.0\,\mathrm{mm}$, and the labels A, B, and C represent the ionizations in z-x, z-y, and x-y-z, respectively.

The ionization pattern generated by SRIM is only allowed in the drift region because just a fraction of reaction products pass through the GEM foil and reach the transfer region and even less frequently the induction zone. The number of primary electrons released in the detector in these regions is shown in Figure 4.10.

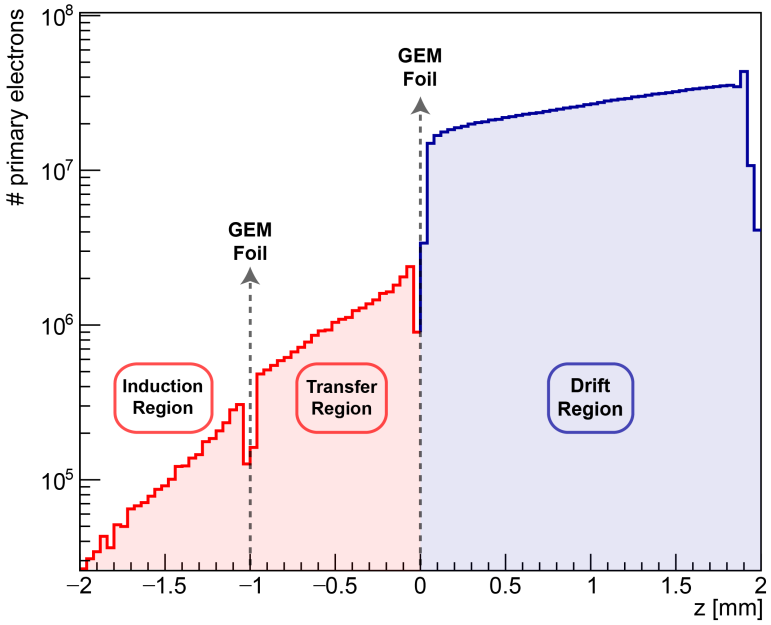

Figure 4.10: Primary electrons released in the detector by the reaction products with respect to z-axis. GEM foils in $0\,\mathrm{mm}$ and $-1.0\,\mathrm{mm}$.

Given the position of the electron cluster in the drift region, the corresponding charge distribution generated at the readout is given by the interpolation of the parameters of the function that represents the charge distribution at the readout in the neighboring positions. These parameters were stored in the lookup table described before.

In this work, linear interpolation was used. It is a mathematical method of curve fitting using linear polynomials. As illustrated in Figure 4.11, consider that the unidimensional function $f(x)$ is known in x_0 and x_1. Given a value x in the interval (x_0, x_1), the correspondent $f(x)$ is

$$\frac{f(x) - y_0}{x - x_0} = \frac{y_1 - y_0}{x_1 - x_0}, \tag{4.3}$$

then,

$$f(x) = y_0 \frac{x_1 - x}{x_1 - x_0} + y_1 \frac{x - x_0}{x_1 - x_0}. \tag{4.4}$$

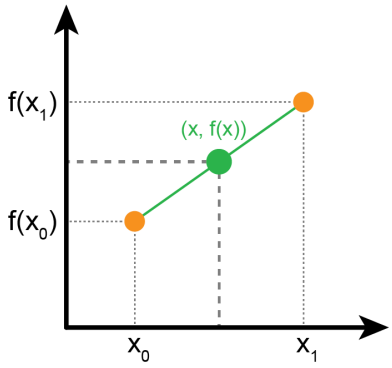

Figure 4.11: Linear interpolation illustration.

An interpolation can also be applied in two and three dimensions, called bilinear and trilinear, respectively, and the last one is used in the fast simulator to obtain the charge collected at the readout.

The trilinear interpolation estimates the value of a function in a point (x, y, z) by just repeating the linear interpolation (four times) between eight vertices of the cube, reducing it to a plane, then to a line, and finally to a point, as sketched in Figure 4.12.

The 6 values of the parameters of the double Gaussian that represents the charge distribution at the readout plane due to a cluster of electrons in point P of Figure 4.12 can be found through the trilinear interpolation of the known values of these parameters in the 8 points obtained through the full simulation. Let x_d, y_d, and z_d be:

$$x_d = \frac{x - x_0}{x_1 - x_0}, \qquad y_d = \frac{y - y_0}{y_1 - y_0}, \qquad z_d = \frac{z - z_0}{z_1 - z_0}, \tag{4.5}$$

where the index 0 and 1 represents the lower and upper point in each axis.

$G_i(x, y, z)$, where $i = 1, ..., 6$, in Figure 4.12a corresponds to the 6 values of the parameters of the double Gaussian that represents the charge distribution at the readout due to a cluster of electrons that starts drifting from the position (x, y, z). The position (x, y, z) is labeled by 0 or 1 when representing the vertices position of the unitary cell as shown in Figure 4.12. For instance, $G(0, 0, 0)$ corresponds to the 6 values of the parameters of the double Gaussian that represent the charge distribution due to a cluster of secondary electrons coming from point $(0, 0, 0)$. The values of the function parameters at each vertex ($G_i(0, 0, 0)$, $G_i(1, 0, 0)$, $G_i(0, 0, 1)$, $G_i(1, 0, 1)$, $G_i(0, 1, 0)$, $G_i(1, 1, 0)$, $G_i(0, 1, 1)$ and $G_i(1, 1, 1)$) are known from the Garfield++ full simulation. The parameters of the charge distributions at the red points indicated in Figure 4.12b are obtained through the interpolation in the x-axis:

$$\begin{aligned}
G_i(0, 0) &= G_i(0, 0, 0)(1 - x_d) + G_i(1, 0, 0)x_d \\
G_i(0, 1) &= G_i(0, 0, 1)(1 - x_d) + G_i(1, 0, 1)x_d \\
G_i(1, 0) &= G_i(0, 1, 0)(1 - x_d) + G_i(1, 1, 0)x_d \\
G_i(1, 1) &= G_i(0, 1, 1)(1 - x_d) + G_i(1, 1, 1)x_d
\end{aligned}$$

Now using the red points to interpolate in the y-axis, the situation pictured in Figure 4.12c

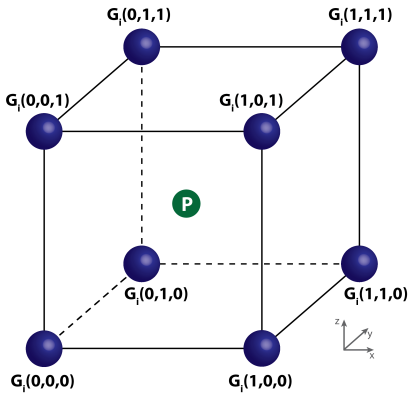

(a) Unknown interpolation point P with eight corner points.

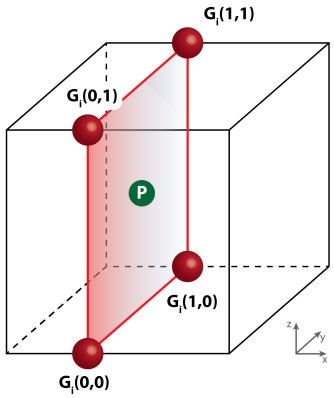

(b) Four points obtained after the first interpolation through the x-axis.

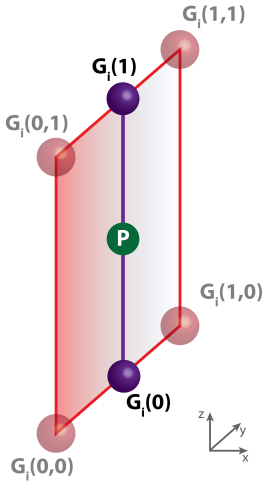

(c) Two points obtained after the interpolation through the y-axis.

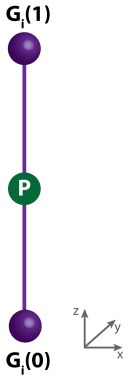

(d) Interpolation point P obtained with the remaining z-axis.

Figure 4.12: Trilinear interpolation strategy.

is obtained:

$$G_i(0) = G_i(0,0)(1-y_d) + G_i(1,0)y_d$$
$$G_i(1) = G_i(0,1)(1-y_d) + G_i(1,1)y_d$$

Finally, the interpolation in z-axis gives the values of the parameters of the function to an arbitrary point inside this cube. In this case, the point labeled as P shown in Figure 4.12d:

$$G_i(P) = G_i(0)(1-z_d) + G_i(1)z_d.$$

This process of collapsing the dimensions one at a time to a point is equivalent to scaling the contribution of each vertex by the volume of the parallelepiped formed between the query point and the vertex diametrically opposed to the vertex in question [72].

4.3 Summary

This chapter described the fast simulator that uses a parameterization of the charge distribution at the readout. The use of GEANT4 and Garfield++ to develop this tool will be validated in the next chapter. It will also present the results and validation of the fast simulator using experimental data from a position-sensitive double-GEM detector prototype.

Chapter 5

Simulation Results and Validation

This chapter will present results to validate the implementation of the tools presented in Chapter 3, which is essential to validate the fast simulator developed in this work and presented in Chapter 4. In order to show the validation and application of the fast simulator, experimental results from reference [73] will be used. This reference presents the performance of a position-sensitive gaseous neutron detector prototype made of GEMs [73].

5.1 Garfield++ Validation with Fe-55

In order to validate the implementation of the Garfield++ toolkit in this work, experimental results were used. This experiment evaluates the performance of a GEM-based detector by measuring the $5.9\,\mathrm{keV}$ X-ray emitted by a Fe-55 radioactive source reported in [74].

The experimental setup, which was reproduced in Garfield++, consists of a single GEM foil using bi-conical holes where outer and inner diameters holes were $55\,\mu\mathrm{m}$ and $85\,\mu\mathrm{m}$, respectively. The thickness of copper and Kapton were $5\,\mu\mathrm{m}$ and $50\,\mu\mathrm{m}$, respectively. The gas mixture was $\mathrm{Ar}/\mathrm{CO_2}$ (75/25) at $1\,\mathrm{atm}$ and the geometric and electric configuration is given in Table 5.1. A schematic view of the apparatus is shown in Figure 5.1.

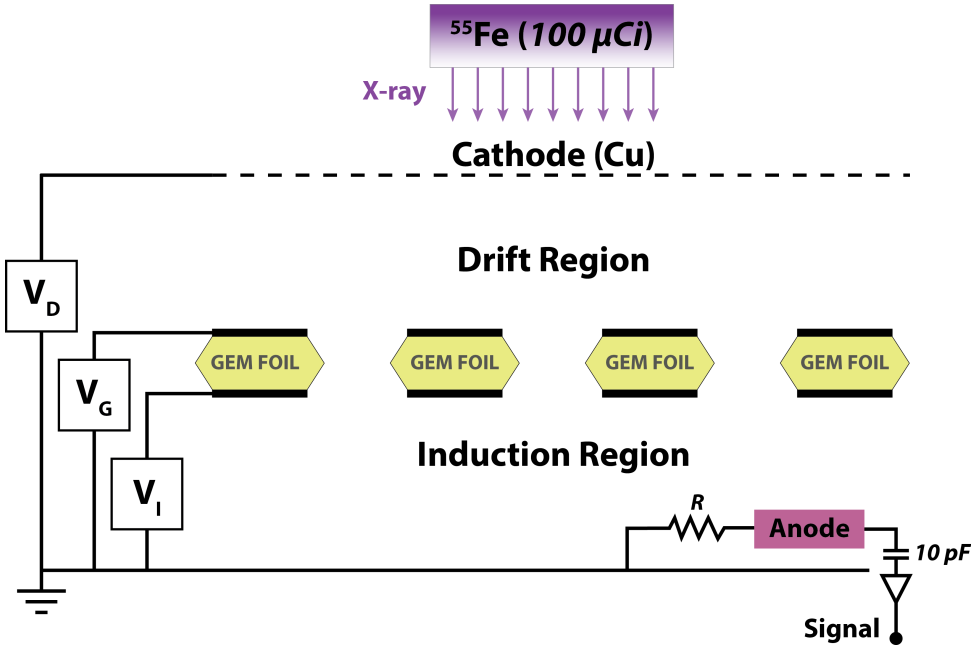

Figure 5.1: Sketch of the experiment. Adapted from [74].

Table 5.1: Geometric and electric setup.

	Drift (V_D)	**Induction (V_I)**
Size [mm]	2	1
Voltage [V]	270	400

Varying the GEM voltage (V_G in Figure 5.1) from $430\,\mathrm{V}$ to $510\,\mathrm{V}$ is observed that the peak of the ^{55}Fe spectrum shifted, both in experiment and simulation, as shown in Figure 5.2, although the simulation results do not reproduce exactly the measurement due to other effects that are not considered such as electronic components and their thresholds.

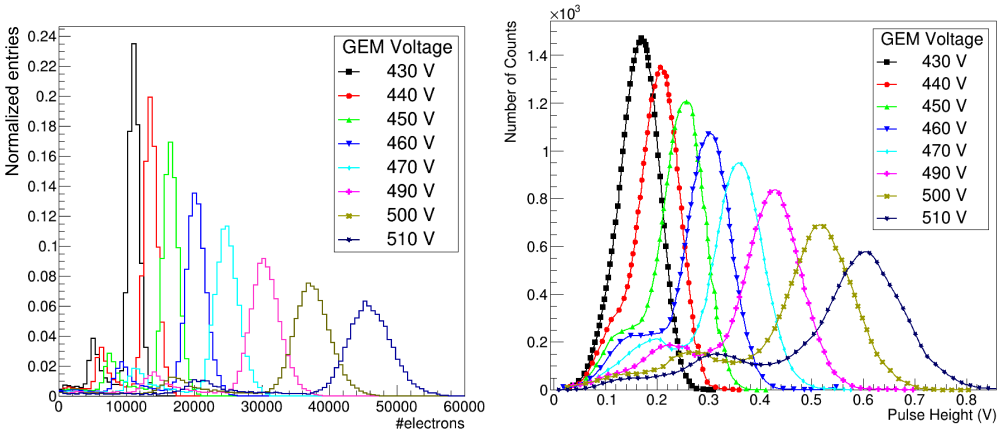

(a) Simulation in Garfield++.

(b) Experimental pulse height. Adapted from [74]

Figure 5.2: Pulse height spectrum for various V_{GEM} for simulation (left) and experiment (right).

The simulation can also be validated by comparing the results for the detector gain. As defined in Chapter 2, the effective gain is defined as the ratio between the amount of charge recorded on the readout electrode and the number of primary charges [50]. The results of the simulations and the experimental values are shown in Figure 5.3. The shape of the curve obtained in the simulation has the same behavior as the experimental one, and they differ only by a constant factor. This discrepancy is reported in other works [68, 75, 76, 77] and it is attributed to the underestimation of the gain in Garfield++ by a factor of 2 in a single GEM foil. In [77] it is pointed out that the underestimation is due to the path of an electron that is considered a straight line between two collisions. This aspect may underestimate the path length inside the GEM hole resulting in a reduced number of interactions and consequently producing a lower number of electron-ion pair production which gives a low effective gain. Despite that, the results indicate that the effective gain of the GEM detector increases exponentially with an increase in the voltage applied in the GEM (V_G). This is due to the avalanche of electrons that increase exponentially with the voltage.

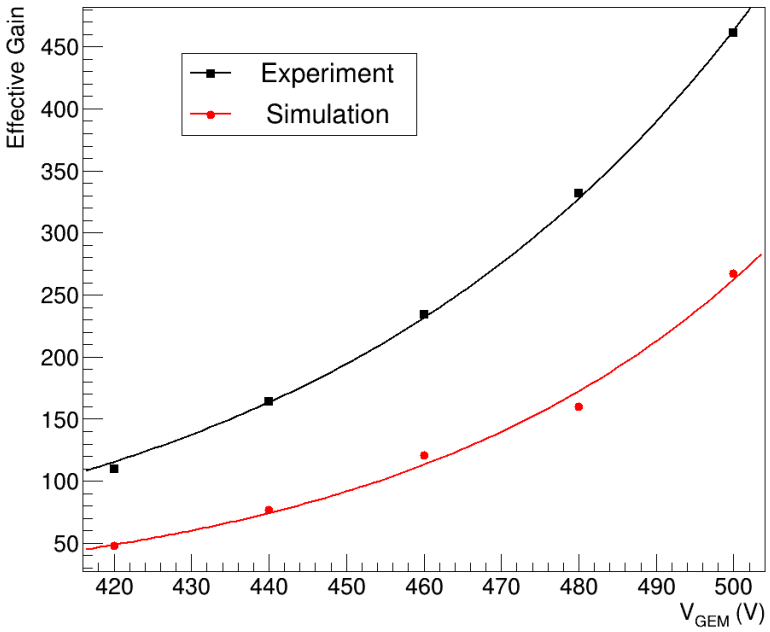

Figure 5.3: Effective gain obtained with simulation and experiment. The difference in Garfield++ is well-known in the MPGD community. Experimental data from [74].

5.2 Double-GEM Detector Prototype

In order to validate the simulations obtained with the fast simulator, experimental data measured by a research group colleague was used, as reported in his master's thesis [73]. This work reports the measurement with a double-GEM prototype, which was carried out at the Nuclear and Energy Research Institute (IPEN) facility. IPEN is a State of São Paulo autarchy, associated to the University of São Paulo for educational purposes and supported and operated technically and administratively by the National Nuclear Energy Commission (CNEN), a federal agency of the Ministry of Science, Technology, Innovations and Communications [78].

The apparatus of the experiment consists of a stack of two GEM foils, one with a large pitch ($280\,\mu\mathrm{m}$, denoted as GEM LP) and one with a standard pitch ($140\,\mu\mathrm{m}$, denoted as GEM S). A $0.5\,\mathrm{mm}$ thick aluminum cathode coated with boron carbide enriched in $^{10}\mathrm{B}$. The distance between the aluminum lid and the cathode is $3\,\mathrm{cm}$. The drift, transfer and induction regions were set to $2\,\mathrm{mm}$, $1\,\mathrm{mm}$ and $1\,\mathrm{mm}$ thick and bias of $100\,\mathrm{V}$, $300\,\mathrm{V}$ and $400\,\mathrm{V}$, respectively. The detector was filled with a gas mixture of Ar/CO_2 (90/10). A schematic view of the detector is shown in Figure 5.4.

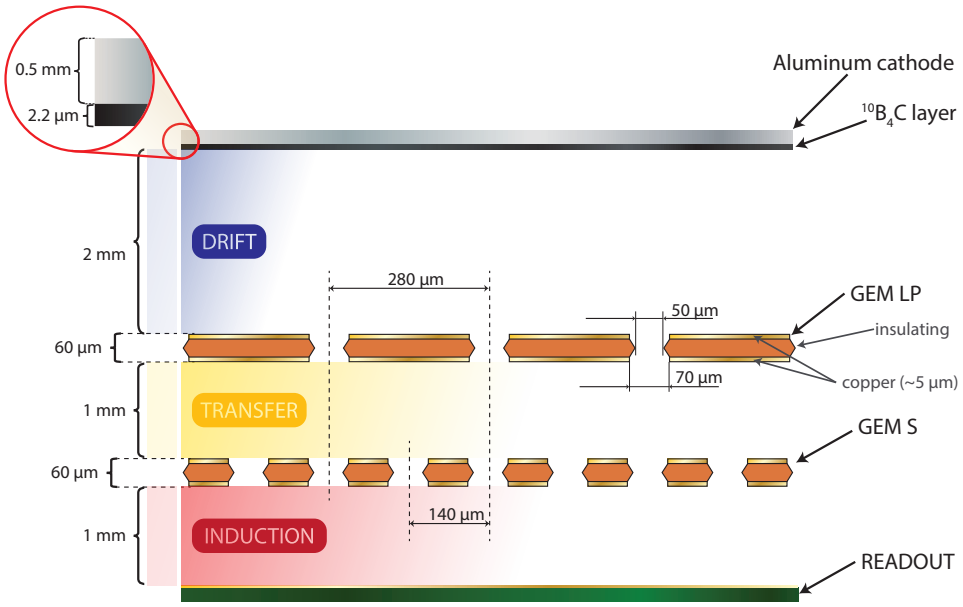

Figure 5.4: Double-GEM prototype scheme. Figure from [73].

5.2.1 Readout system

The detector readout is made of printed circuit board coupled to 256 copper strips in both X and Y direction, widely used for two-dimensional projective readout [45], shown in Figure 5.5. These strips consist of a $50\,\mu\mathrm{m}$ polymer foil and have $400\,\mu\mathrm{m}$ pitch.

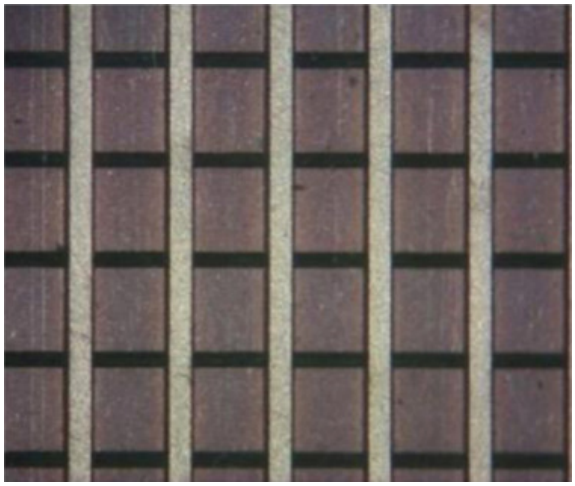

Figure 5.5: Readout strips with $400\,\mu\mathrm{m}$ pitch. Figure from [45].

The electrons generated in this detector are then collected in these strips, and the signal is read by resistive chains that provide four channels (two for each direction). The resistive chains consist of 128 SMD (Surface Mounted Device) resistors of $60.00\,\Omega$ connected to a Panasonic®130-pin connector, as shown in Figure 5.6.

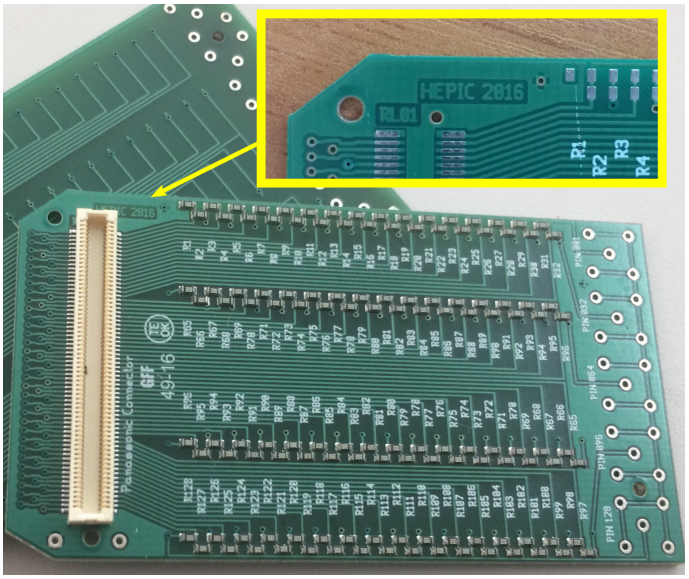

Figure 5.6: Resistive chain with 128 SMD resistors with a Panasonic®130-pin connector. Figure from [63]

In addition to the four signals (two for each direction x-y), a fifth signal (charge signal) is used as the trigger for the data acquisition. The acquisition system is based on NIM electronics, which is very well known for its reliability and versatility, considering the working regime of the detector. The signal collected at the bottom of the GEM LP (already pre-amplified) is divided into two chains: the first passing through a faster preamplifier followed by a discriminator, which will define the charge threshold for a given event. If the signal surpasses the threshold, it activates the 'gate generators', which define the digitizer's reading interval. The other chain is amplified and acquired as the charge signal. A multi-channel counter monitors the beam monitor detector, the discriminator, and the gate generator to check the triggering system. The sketch of the acquisition systems is shown in Figure 5.7

The signals collected at the end of the resistive chains on the readout are pre-amplified, amplified, and digitized as usual. This setup allows to reconstruct the events (their energy and position) using only five signals.

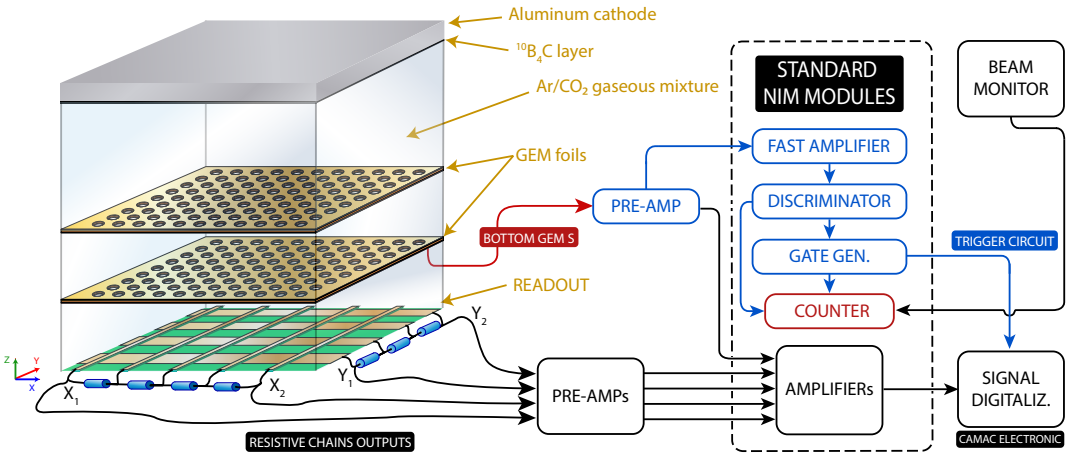

Figure 5.7: Sketch of the acquisition system. Figure from [73]

The charge signal obtained in each point (X_1, X_2, Y_1, and Y_2) is used to reconstruct the position where the charge reaches the readout using the center of gravity (COG) procedure [73]:

$$x = A\frac{Q_{X_2} - Q_{X_1}}{Q_{X_2} + Q_{X_1}} \quad \text{and} \quad y = B\frac{Q_{Y_2} - Q_{Y_1}}{Q_{Y_2} + Q_{Y_1}}, \tag{5.1}$$

where A and B are constants to fine adjust the image. Q_{X_1}, Q_{X_2}, Q_{Y_1} and Q_{Y_2} are the charges collected at the resistive chains. Figure 5.8 shows a schematic view of this procedure.

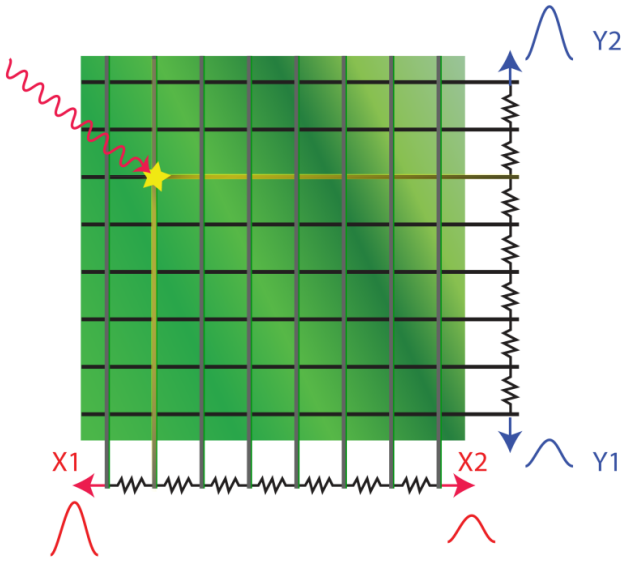

Figure 5.8: Sketch of the charge signal distribution in the strips. Figure from [73].

5.2.2 Measurements

The detector prototype was tested at the IEA-R1 nuclear reaction installed at the Nuclear and Energy Research Institute (IPEN) facility [79]. The IEA-R1 has $4.5\,\mathrm{MW}$ power pro-

vided by a water-cooled pool reactor, shown in Figure 5.9.

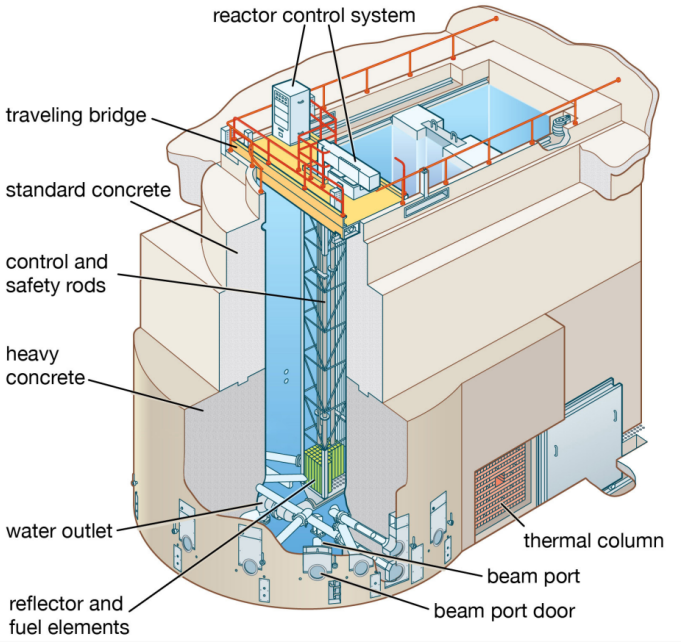

Figure 5.9: Sketch of pool reactor. Figure from [73].

A multi-blade focusing silicon monochromator is used to select monochromatic neutrons with $1.399\,\text{Å}$ ($41.8\,\text{meV}$), yielding a flux of neutrons of $6.22 \times 10^4\,\text{n}/(\text{cm}^2\,\text{s})$.

The apparatus was mounted on a x-y-z precision table allowing a fine positioning of the detector with respect to the beam. The detector is shown in (A) of Figure 5.10, where the shields of the y-axis resistive chain (B), the preamplifiers box (C), high voltages inputs (D), and the beam outlet (E) are also shown.

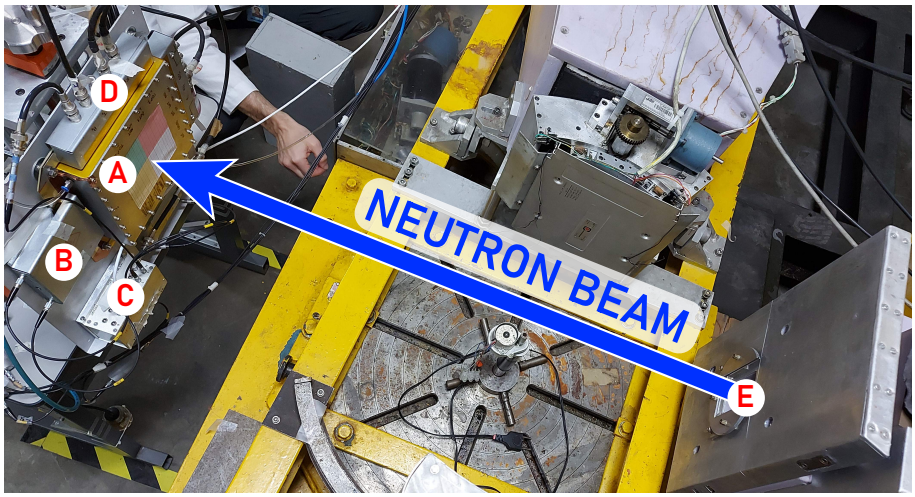

Figure 5.10: The detector position (A) relative to the neutron beam. (B) shields of the y-axis resistive chain, (C) preamplifiers box, (D) high voltage inputs and (E) beam outlet. Figure from [73].

5.3 Double-GEM Detector Simulation

In GEANT4 a thermal neutron point source with $25\,\mathrm{meV}$ was used to hit perpendicularly the boron-10 converter layer. The visualization of this interaction given in GEANT4 is shown in Figure 5.11 with some graphic adaptations for better visualization. By default, GEANT4 attributes the color red, green, and blue for negative, neutral, and positive charges, respectively. The details of this particular simulated interaction given by GEANT4 in the run-time are shown in Figure 5.12.

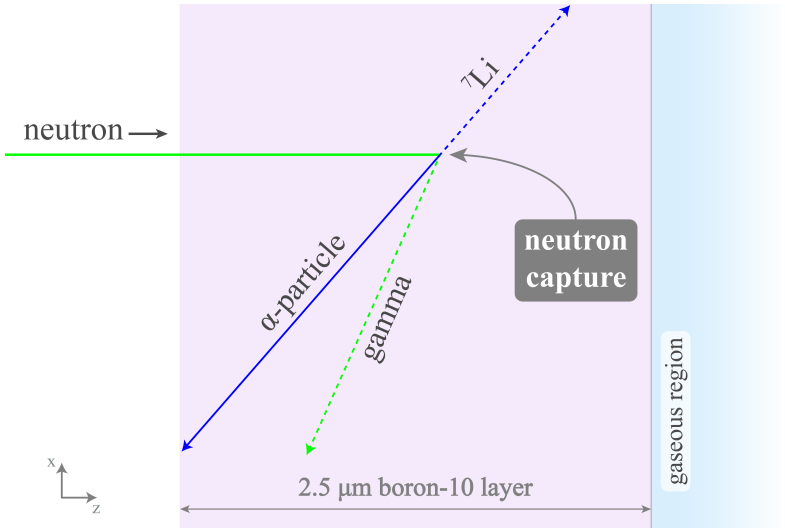

Figure 5.11: Thermal neutron interaction with the boron-10 layer in GEANT4. This figure was adapted from the default GEANT4 visualization. Neutral particle tracks are pictured in green and positive ones in blue.

```
G4WT0 > ===================================================================
G4WT0 >
G4WT0 > --> Event 0 starts with initial seeds (69251859,72525340).
G4WT0 >
G4WT0 > ************************************************************************************************************
G4WT0 > * G4Track Information:   Particle = neutron,   Track ID = 1,   Parent ID = 0
G4WT0 > ************************************************************************************************************
G4WT0 >
G4WT0 > Step#    X(mm)    Y(mm)    Z(mm) KinE(MeV)  dE(MeV) StepLeng TrackLeng  NextVolume ProcName
G4WT0 >     0       -0       -0     -500   2.5e-08        0        0         0 worldPhysical initStep
G4WT0 >     1        0        0        0   2.5e-08        0      500       500 b10PhysicalSD Transportation
G4WT0 >     2        0        0  0.00142         0        0  0.00142       500 b10PhysicalSD neutronInelastic
G4WT0 >
G4WT0 > ************************************************************************************************************
G4WT0 > * G4Track Information:   Particle = Li7,   Track ID = 4,   Parent ID = 1
G4WT0 > ************************************************************************************************************
G4WT0 >
G4WT0 > Step#    X(mm)    Y(mm)    Z(mm) KinE(MeV)  dE(MeV) StepLeng TrackLeng  NextVolume ProcName
G4WT0 >     0        0        0  0.00142     0.848        0        0         0 b10PhysicalSD initStep
G4WT0 >     1  0.00102 0.000366  0.00214         0    0.848   0.0013    0.0013 b10PhysicalSD ionIoni
G4WT0 >
G4WT0 > ************************************************************************************************************
G4WT0 > * G4Track Information:   Particle = gamma,   Track ID = 3,   Parent ID = 1
G4WT0 > ************************************************************************************************************
G4WT0 >
G4WT0 > Step#    X(mm)    Y(mm)    Z(mm) KinE(MeV)  dE(MeV) StepLeng TrackLeng  NextVolume ProcName
G4WT0 >     0        0        0  0.00142     0.471        0        0         0 b10PhysicalSD initStep
G4WT0 >     1 -0.00416 -0.00128 -2.17e-19     0.471        0  0.00458   0.00458 worldPhysical Transportation
G4WT0 >     2     -500     -154     -170     0.471        0      550       550  OutOfWorld Transportation
G4WT0 >
G4WT0 > ************************************************************************************************************
G4WT0 > * G4Track Information:   Particle = alpha,   Track ID = 2,   Parent ID = 1
G4WT0 > ************************************************************************************************************
G4WT0 >
G4WT0 > Step#    X(mm)    Y(mm)    Z(mm) KinE(MeV)  dE(MeV) StepLeng TrackLeng  NextVolume ProcName
G4WT0 >     0        0        0  0.00142      1.47        0        0         0 b10PhysicalSD initStep
G4WT0 >     1   -0,002 -0.00072        0         0     1.47  0.00256   0.00256 b10PhysicalSD Transportation
G4WT0 >
G4WT0 > >>> Event 0 >>> Simulation truth : neutron (0,0,0.006854069448190979)
G4WT0 > Thread-local run terminated.
G4WT0 > Run Summary
G4WT0 >   Number of events processed : 1
G4WT0 >   User=0.050000s Real=0.056968s Sys=0.010000s [Cpu=105.3%]
```

Figure 5.12: Details of the nuclear interaction with boron-10 simulated in GEANT4 of Figure 5.11.

5.3.1 Detection Efficiency

All the geometry and materials described in the double-GEM experiment were simulated in GEANT4. A thermal neutron point source with $41.8\,\mathrm{meV}$ was used to evaluate the optimum thickness for a $^{10}B_4C$ converter layer, which corresponds to the thickness that permits the maximum number of reaction products (α-particle and $^7\mathrm{Li}$ ions) entering the gaseous drift region of the detector. The thickness of the converter layer was varied from $0.5\,\mu\mathrm{m}$ to $5.0\,\mu\mathrm{m}$ and 1×10^6 neutrons were launched for each studied thickness. The results are shown in Figure 5.13, which shows an optimum thickness close to $2.5\,\mu\mathrm{m}$. It is also shown an analytical calculation from the experimental work [73]. The results obtained with the GEANT4 are in reasonable agreement with the analytical prediction.

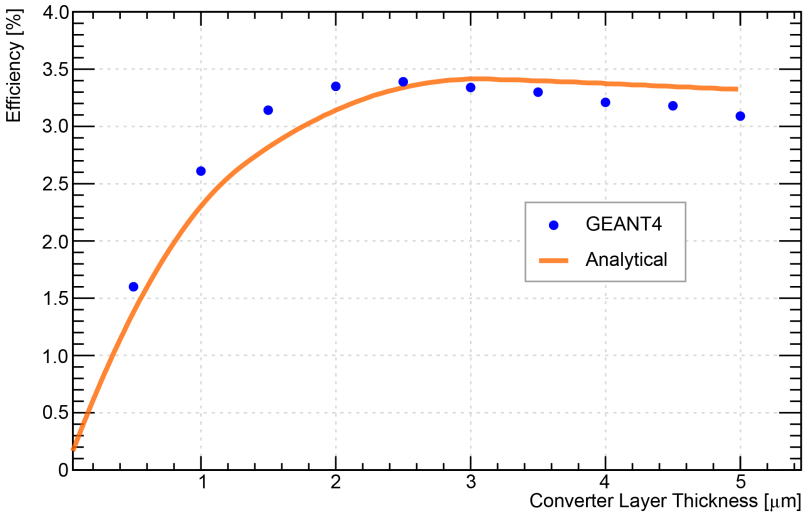

Figure 5.13: GEANT4 simulation of the optimum efficiency for the thickness of $^{10}B_4C$ converter layer. The uncertainty is smaller than the point size. The line is an analytical calculation from [73].

5.3.2 Spatial Resolution and Position Calibration

A cadmium mask was used to obtain the position calibration and an estimation of the spatial resolution of the detector given that cadmium has a high neutron absorption cross-section. The mask was placed just in front of the detector, intercepting the neutron beam. The cadmium mask was constructed with a set of holes with diameters of $1.5\,\mathrm{mm}$, $2.5\,\mathrm{mm}$ and $3.5\,\mathrm{mm}$, as shown in Figure 5.14.

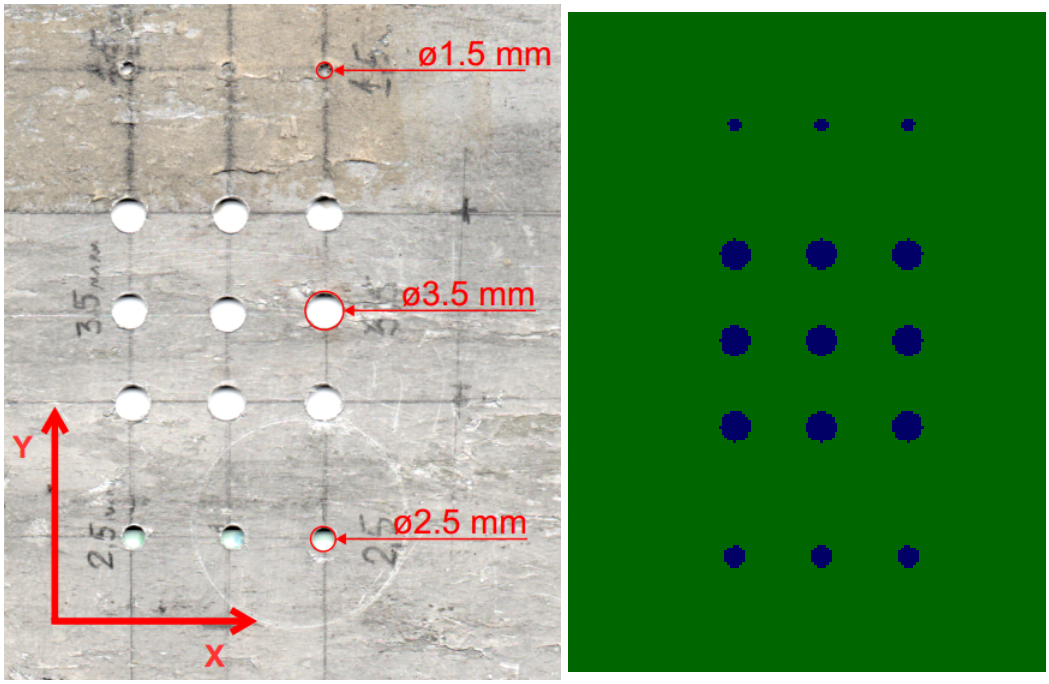

(a) Drilled cadmium mask. Figure from [73].

(b) Mask reproduced in Geant4.

Figure 5.14: Cadmium mask.

The simulation was accomplished as close as possible to the configuration in the experimental environment. A rectangular uniform thermal neutron beam of $41.8\,\mathrm{meV}$ was simulated covering the holes in the cadmium mask. The material in the converter layer was set as boron carbide ($^{10}B_4C$) with $2.2\,\mu\mathrm{m}$ thick and the detector was filled with a gas mixture of Ar/CO_2 (90/10). The geometry with the cadmium mask and a visualization of the tracks generated in GEANT4 are shown in Figure 5.15.

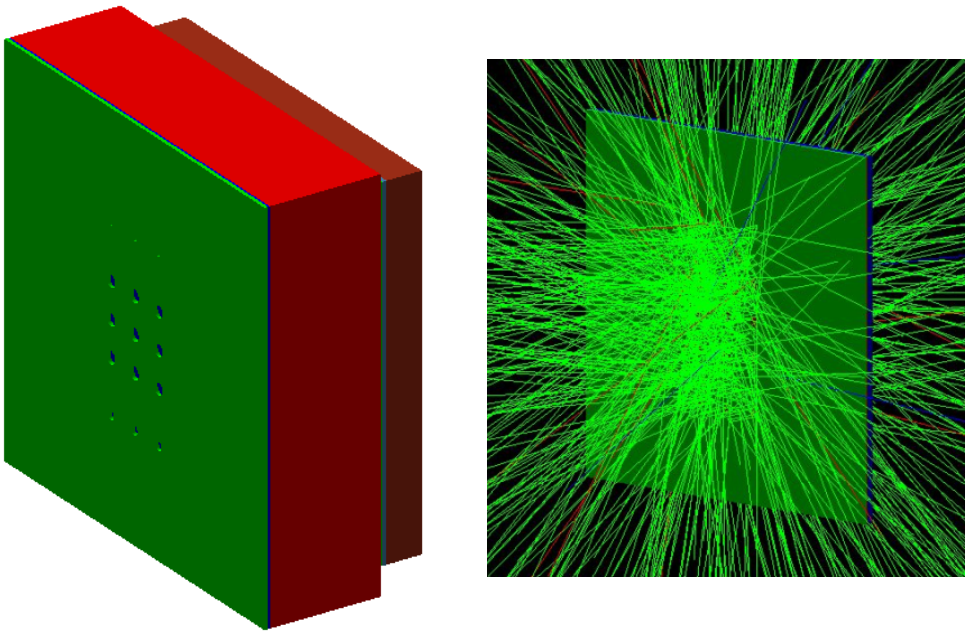

Figure 5.15: Left: experimental geometry simulated in GEANT4, with cadmium mask in green. Right: example of particles tracking from the rectangular thermal neutron beam. Line colors red, green, and blue are for negative, neutral, and positive charges, respectively.

A first result can be obtained considering only the energy deposited in the detector by the neutrons. Figure 5.16 shows the energy spectrum obtained from the experimental data (red line) and the simulation as well. It shows the contribution from each reaction product (α-particles in blue and $^{7}\mathrm{Li}$ in magenta) and the total one (black line). This agreement between simulation and experimental data is already very good although this simulation does not include several effects, like the charge multiplication (later considered in the fast simulator) and the electronics of the experiment.

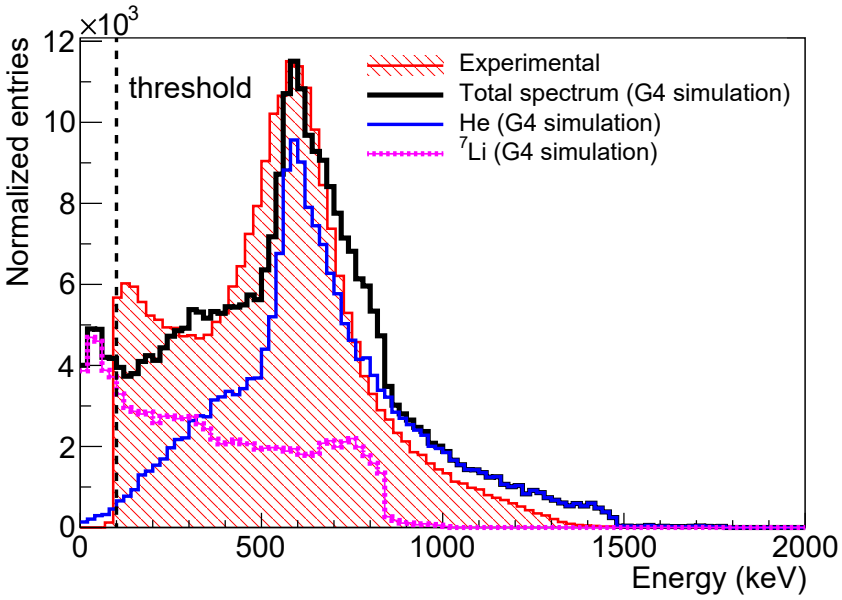

Figure 5.16: Simulated energy spectrum in GEANT4 compared with the experiment. Figure from [32].

This simulation uses the low-energy electromagnetic model Livermore [80] to evaluate the deposited energy by the reaction products (α-particle or ^{7}Li) inside the drift region and it was used as a pre-calibration for the experimental spectrum. The electronic threshold of $100\,\mathrm{keV}$ was not considered in the simulation as well as the charge multiplication process which will be presented later during the discussion of the fast simulator.

The spatial distribution in the x-y plane obtained in the experiment and in GEANT4 using the cadmium mask is shown in Figure 5.17. The charge distributions are very similar with a higher intensity in the center of each hole and getting smoother in smaller ones.

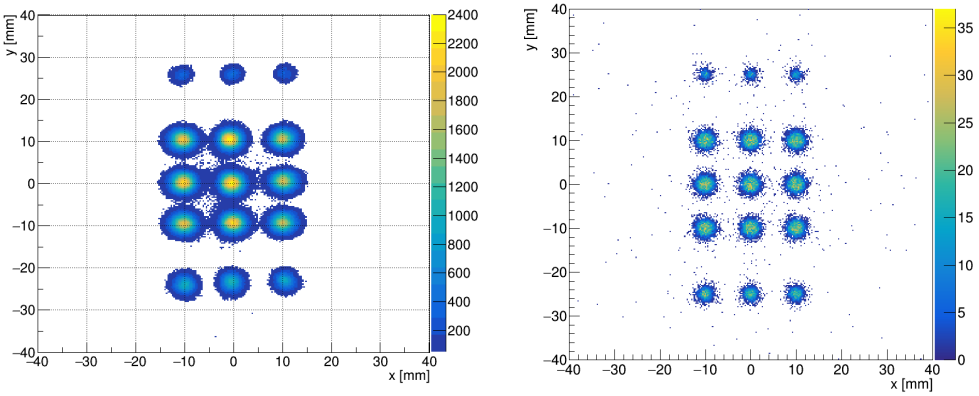

(a) Experimental data from [73].

(b) Simulation in GEANT4.

Figure 5.17: Neutron image in x-y experimental and simulation.

Moving to the fast simulator, the first step is to generate the electrostatic conditions in the detector, as the electrostatic potential map shown in Figure 5.18.

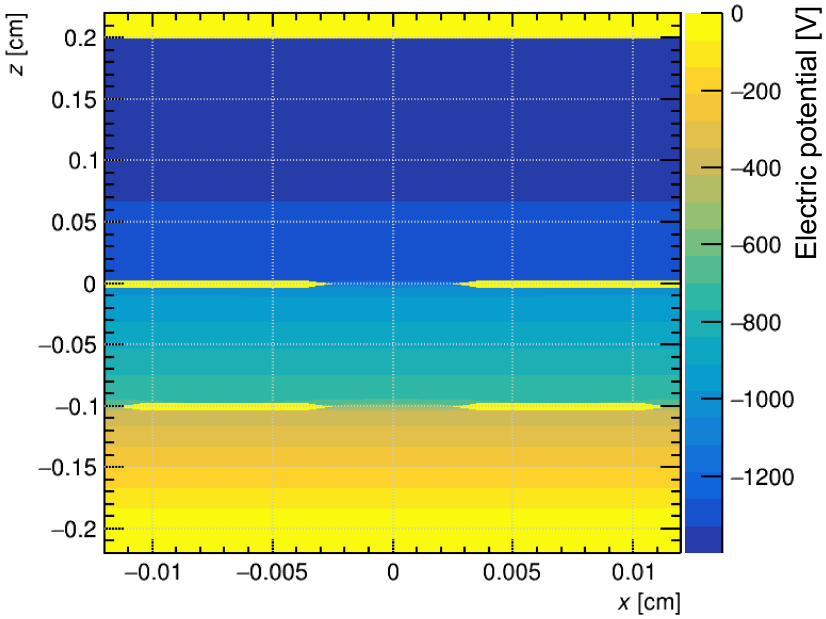

Figure 5.18: Electrostatic potential map in the fast simulator given in Volts.

The first result from the fast simulator is again the energy spectrum and the charge distribution in the readout (x-y) plane. Inserting the GEANT4 output (position and momentum of the reaction products) in the fast simulator, the yield and spatial distribution of the charge are obtained as shown in Figure 5.19. The obtained spectrum as well as the x-y distribution in the fast simulator have good agreement with the experimental data.

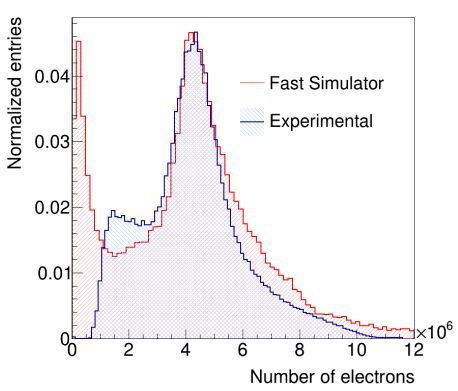

(a) Simulated energy spectrum in fast simulator compared with the experiment. Figure from [81].

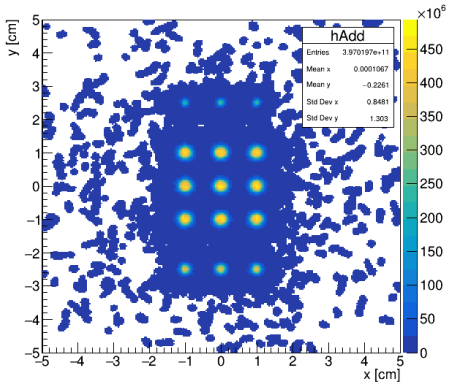

(b) Distribution in x-y for the fast simulator.

Figure 5.19: Results in the fast simulator.

Figure 5.20 shows a projection of the charge distribution in the x-axis for the three central holes (with $3.5\,\mathrm{mm}$ diameter, in Figure 5.14). The simulation shows a good agreement with the experimental data. Few differences can be observed in the amplitude of the distributions as well as in their tails. This feature can be due to noise, lack of homogeneity in the neutron beam, and other effects that were not considered in the fast simulator.

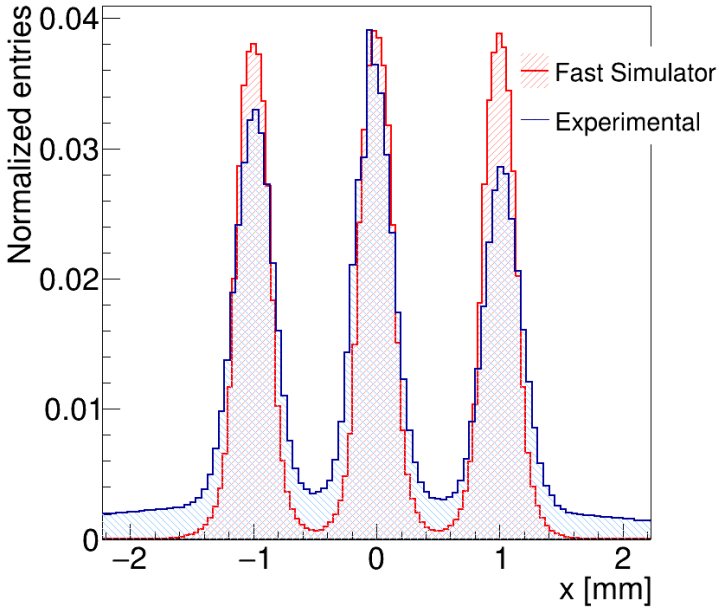

Figure 5.20: Projection in x-axis for the central holes in mask A. Figure from [81].

The set of holes in the mask was used to compare the position resolution (given by the FWHM of the spatial charge distribution) calculated through the fast simulator and the experimental results as shown in Figure 5.21. It can be seen that the shape of the two curves are similar differing only by a fixed amount.

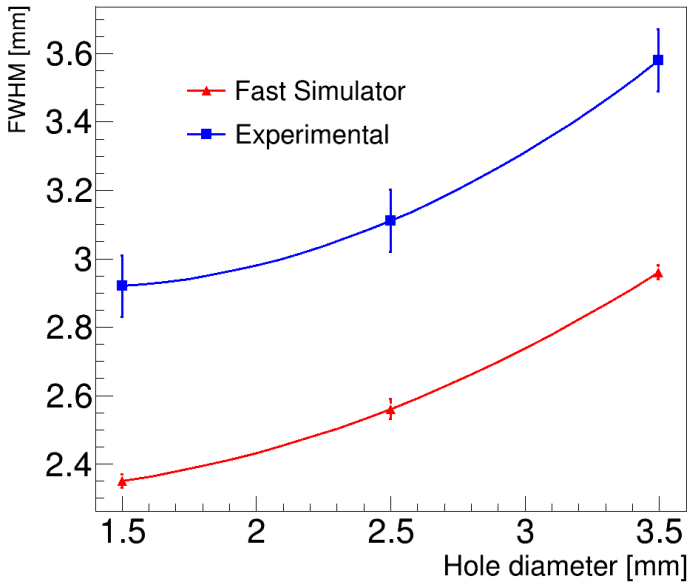

Figure 5.21: Comparison between the FWHM obtained from the holes in mask A for fast simulator and experimental. Figure from [81].

It is interesting to add the simulation obtained in GEANT4 in some of the previous results to emphasize the importance of the fast simulator. When the drift, diffusion, and

multiplication of the electrons in the avalanche are taken into account the results change considerably. In the next figures, the colors red, blue, and black represent fast simulator, GEANT4, and experimental data, respectively.

Figure 5.22 shows the energy spectrum obtained using the fast simulator (red), the one using only the deposited energy by the reaction products in GEANT4 (blue) and the experimental data (black).

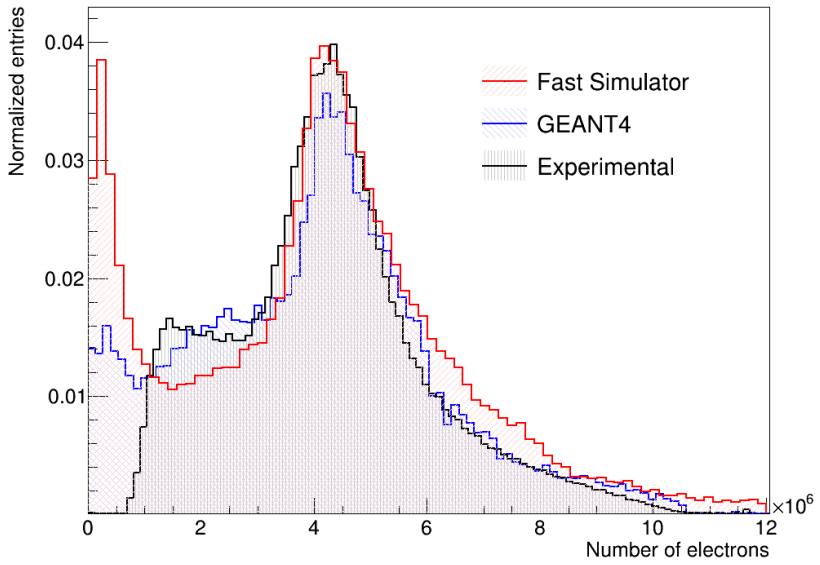

Figure 5.22: Energy spectrum in the fast simulator (red line), GEANT4 output (blue line) and experimental (black line).

In Figure 5.23, the red line corresponds to the spatial charge distribution in the fast simulator, the blue line shows the position distribution of the energy deposited by the reaction products in GEANT4 and the black line shows the projection obtained in the experimental data.

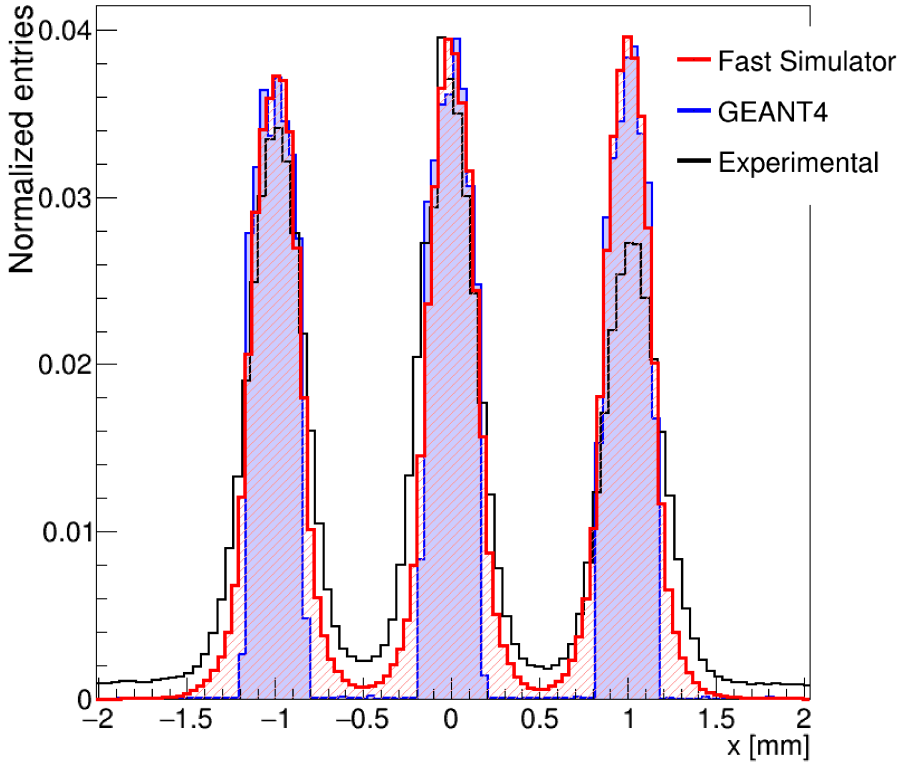

Figure 5.23: Spatial charge distribution in one axis from the fast simulator (red line), GEANT4 output (blue line) and experimental (black line).

It is also interesting to compare the FWHM obtained with the fast simulator, GEANT4 and in the experimental data as shown in Figure 5.24.

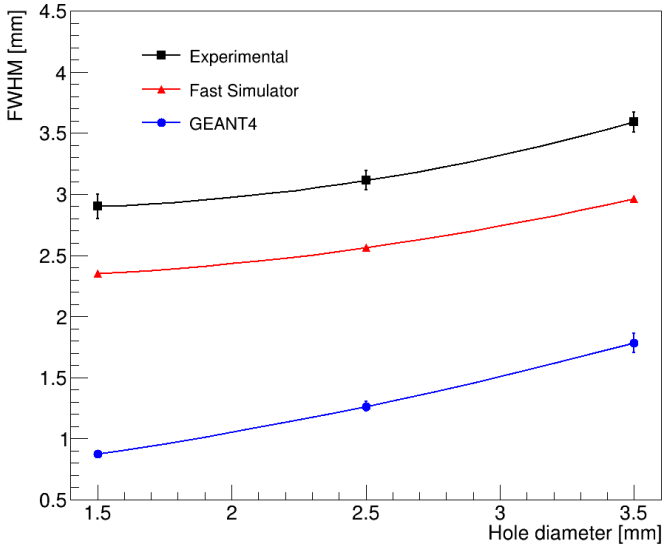

Figure 5.24: Comparison between the FWHM obtained from the holes in mask A for the fast simulator(red), GEANT4 (blue) and experimental (black).

Although it has an agreement, the long tails in the fast simulator are more similar to the experimental data. This shows that in the fast simulator the drift of the charges and its impact on the detector response is more accurate when considering only the GEANT4.

Benchmark

The simulation of the double-GEM detector prototype was used to estimate the improve in CPU processing time. The complete track for just one electron spends on average $11\,007(1382)\,\mathrm{ms}$ in a full simulation, while in the fast simulator the time spent was $0.82(3)\,\mathrm{ms}$. Considering that one event deposits an average $407\,\mathrm{keV}$ according to the simulations which yield $\approx 1.4 \times 10^4$ electrons, hence $\approx 43\,\mathrm{h}$ per event in the full simulation against $\approx 12\,\mathrm{s}$ per event in the fast simulator. Thus, this benchmark, performed using an Intel Core i5-8265U CPU @1.60 GHz and 8GB of RAM, shows that the fast simulator was 4 orders of magnitude faster.

5.4 Summary

The fast simulator has shown to have a good agreement concerning the energy spectrum as well as the spatial distribution when compared to experimental data although some discrepancies are still present. The processing time was greatly improved in the fast simulator, making it possible to study these detectors using Garfield++ and GEANT4. In the next chapter, the fast simulator was used to study possible strategies to improve the position resolution of a detector analyzing possible optimizations in terms of gas mixture and pressure.

Chapter 6

Detector Optimization

Beam monitoring is important in several applications such as particle accelerators, or in the medical field where the precise control of the beam is crucial [82]. Radioisotope production and cancer radiotherapy need precision and accurate beam for safety and efficient procedures. Another example is neutron scattering which is used in many areas of science, from clean energy to nanotechnology, materials engineering, and fundamental physics [83]. All these applications need a device capable of locating the radiation, hence a position-sensitive detector.

A position-sensitive detector is a device constructed with the purpose of locating the interaction point of a specific particle and with a certain resolution capable of distinguishing closely spaced radiation making the spatial resolution an important parameter in these devices. The desired spatial resolution depends on the application. For instance, in high-energy experiments, a resolution of a few microns is not uncommon, on the other hand, for medical applications, like a CT scanner, a spatial resolution of a few millimeters is appropriate for diagnostic [22].

Considering GEM-based neutron detectors with a solid neutron converter, the performance of a position-sensitive detector depends on several conditions [84]:

- the emitting angle of the secondary charged particle;
- the track length of a charged particle in the working gas;
- the electron diffusion and
- the pitch of the readout strips [20].

Some of these parameters can be modified aiming the improvement of the spatial resolution. For instance, in [85] a very high spatial resolution is achieved by increasing the counting-gas pressure and allowing an improvement from $2.6\,\mathrm{mm}$ to $1.2\,\mathrm{mm}$ with $1.0\,\mathrm{bar}$ and $3.5\,\mathrm{bar}$, respectively. The CASCADE and Japan Proton Accelerator Research Complex (J-PARC) have almost the same working gas and pressure but a different readout strip pitch. In J-PARC the pitch is $0.8\,\mathrm{mm}$ which gives a $1.2\,\mathrm{mm}$ resolution at $1\,\mathrm{bar}$ which is better than $2.6\,\mathrm{mm}$ at the CASCADE with a strip of $1.56\,\mathrm{mm}$. A sub-millimeter spatial resolution in neutron detection can be achieved with the introduction of a Time Projection Chamber (TPC), as suggested in [86, 87, 88, 89].

In this chapter, an optimization of the double-GEM detector prototype described in section 5.2 will be shown, focusing on the improvement of the spatial resolution by exploiting the properties of the working gas, as its composition and its pressure, making changes in reaction products path length and in the electron drift and diffusion.

6.1 Preliminary analysis

Previously to the optimization using the fast simulator, a series of tests of the viability of the proposed approaches to improve the spatial resolution were performed with preliminary simulations in both SRIM and Garfield++.

Considering that when a particle travels a shorter path, which in this case is the projected range, the ionization can be constrained in a small region leading to an improvement in the spatial resolution. Using SRIM, the projected range was simulated for α-particles for different pressures and gases, shown in Figure 6.1. This result shows that the projected range for xenon is shorter than for argon, and higher pressures also result in a shorter projected range.

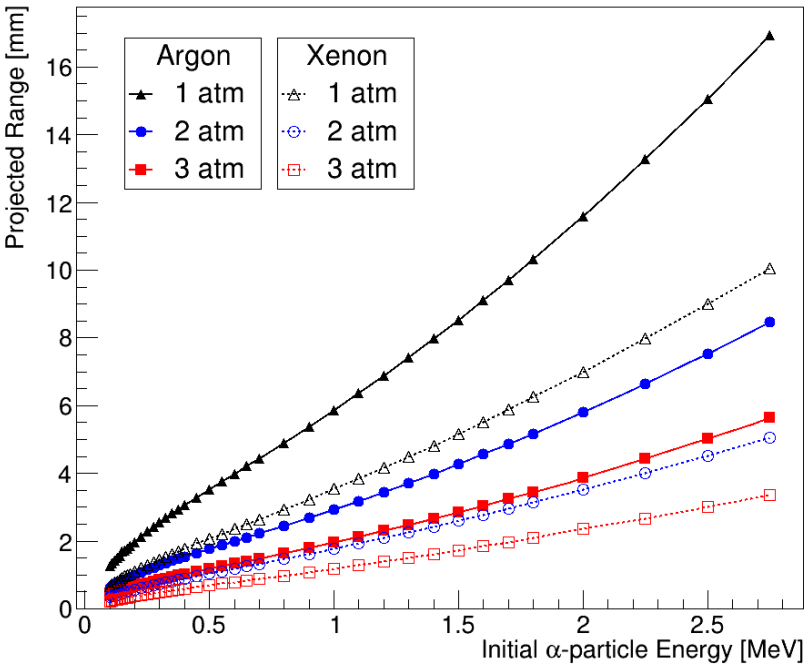

Figure 6.1: Alpha particle range depending on its initial energy, for different pressures. Close and open marks represent argon and xenon gas, respectively. Simulated using SRIM.

Using Garfield++, ionization in the drift region was simulated to illustrate the motivation for increasing the pressure in argon, as shown in Figure 6.2. The path of an ionizing particle (α-particle or ^{7}Li, in this case) through the drift region for different values of pressure shows that when the pressure increases the track of the particle, as well as the

electron deposition, is restricted to a smaller range in x-axis as shown in the left panel (Figure 6.2a). The right panel (6.2b) shows the electron-clusters distribution in the x-axis due to 500 neutrons with $41.8\,\mathrm{meV}$ hitting always perpendicularly the same point of the detector, i.e. starting at the same spatial point and moving always to the same direction. This result shows that the distribution gets narrower as the pressure increase.

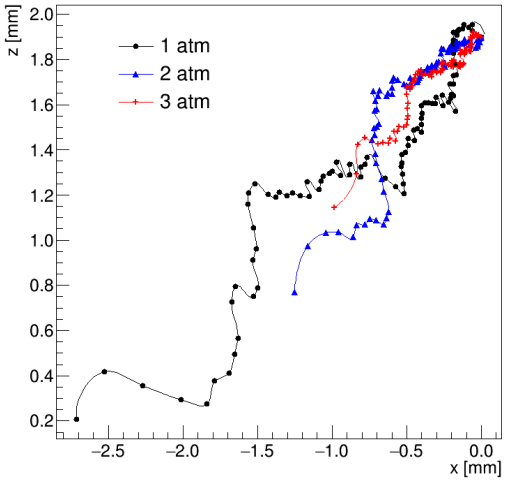

(a) A visual example of the decrease in the ionization region for one particle..

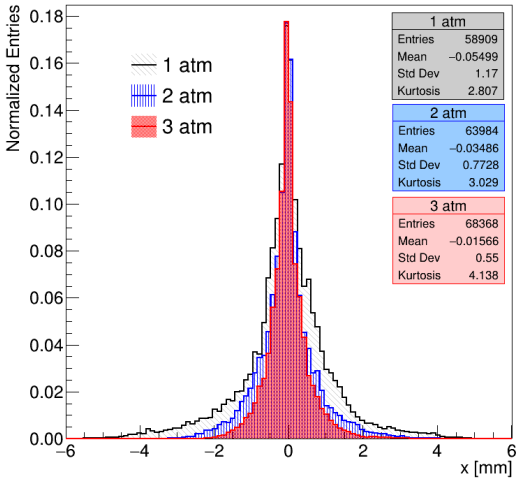

(b) Electron-cluster position on the x-axis in the drift region, considering 500 neutrons starting at the same point.

Figure 6.2: Analysis of the relation between argon gas pressure and the position resolution. Figure from [90].

The results presented in Figure 6.1 and Figure 6.2 are a clear indication that the spatial resolution can be improved by increasing the pressure and/or changing the gas composition to one with a higher atomic number.

6.2 Optimizations using the Fast Simulator

The fast simulator described in Chapter 4 was used to perform a series of simulations using two gas mixtures:

- $\mathrm{Ar}/\mathrm{CO}_2$ (90/10) and
- $\mathrm{Xe}/\mathrm{CO}_2$ (90/10),

and three values of pressure: $1, 2,$ and $3\,\mathrm{atm}$. Each configuration was initialized with 2×10^6 thermal neutrons of $41.8\,\mathrm{meV}$ hitting perpendicularly the detector.

The spatial resolution was characterized and quantified by the spread functions: *point spread function* (PSF) and *edge spread function* (ESF). These methods were described in the previous chapter, see section 2.3.

The distribution in the x-y plane of the electrons in the readout plane as well as the projection in the x-axis for the point spread function with the Gaussian fit for 1, 2, and 3 atm is shown in Figure 6.3 and in Figure 6.4 for argon and xenon, respectively.

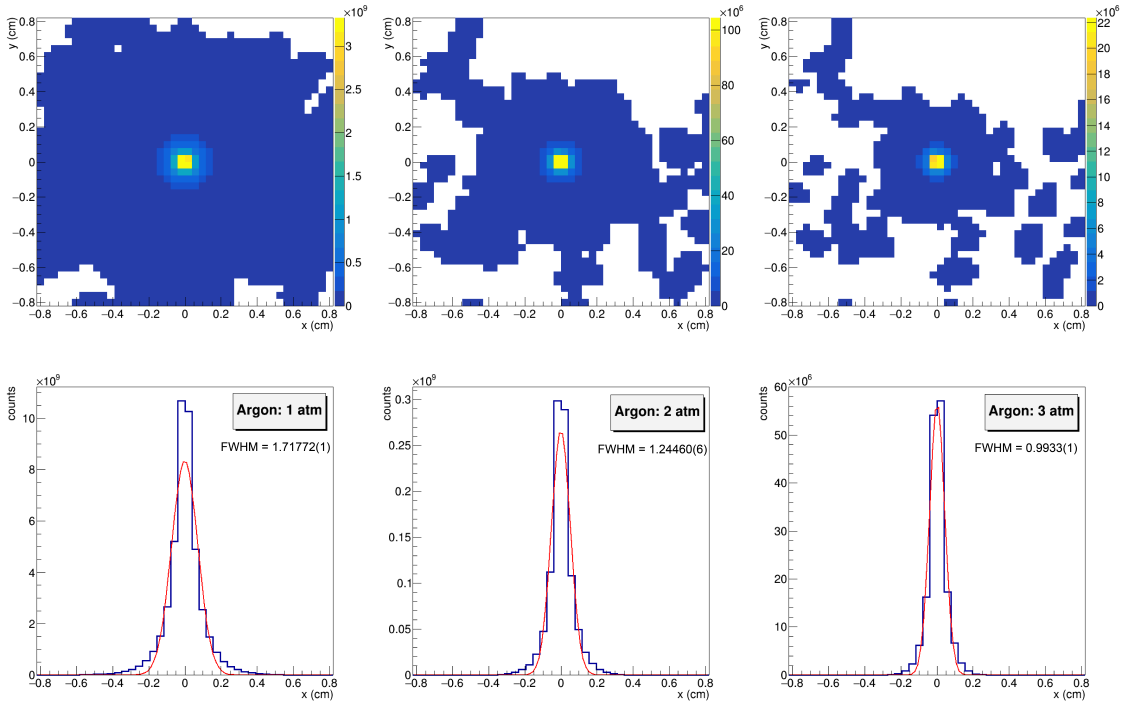

Figure 6.3: Optimization for argon gas and three pressures: 1, 2, and 3 atm.

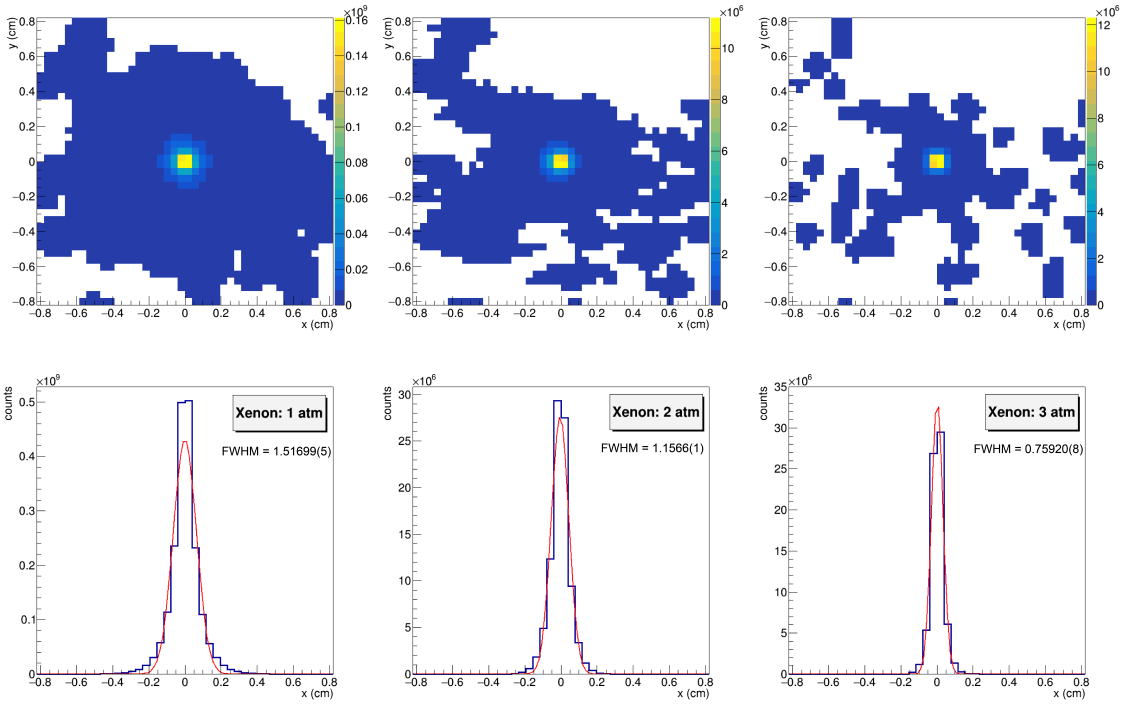

Figure 6.4: Optimization for xenon gas and three pressures: 1, 2 and 3 atm.

A summary of the spatial resolution, in terms of the FWHM, obtained through the PSF method is compiled in Figure 6.5.

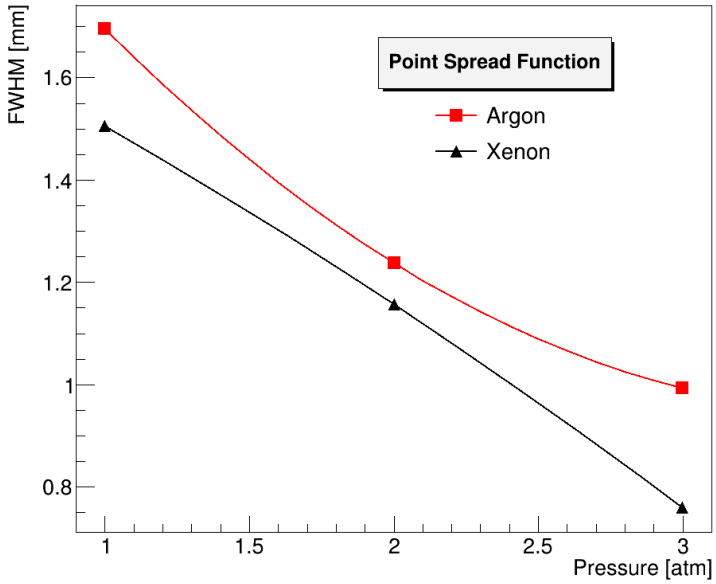

Figure 6.5: Spatial resolution with respect to gas pressure estimated using the point spread function (PSF). The uncertainty is smaller than the point size.

The spatial resolution was also estimated using the ESF. To apply the ESF in the simulation, a cadmium mask with a square hole of $1\,\mathrm{cm}^2$ centered in (0,0) in the plane x-y was simulated. A rectangular beam of 2×10^6 thermal neutrons was used with the same energy of $41.8\,\mathrm{meV}$. The charge distribution at the readout plane as well as its spatial (x-y) distribution is shown in Figure 6.6 and in Figure 6.7 for argon and xenon, respectively.

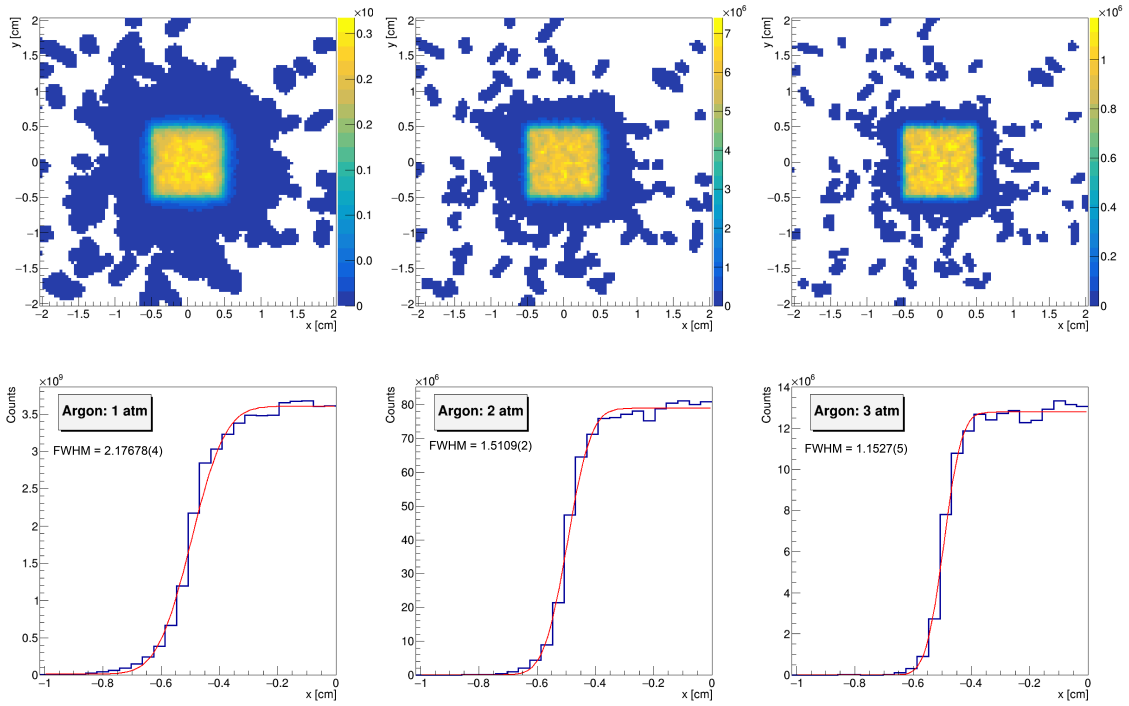

Figure 6.6: Optimization for argon gas and three pressures: 1, 2, and 3 atm.

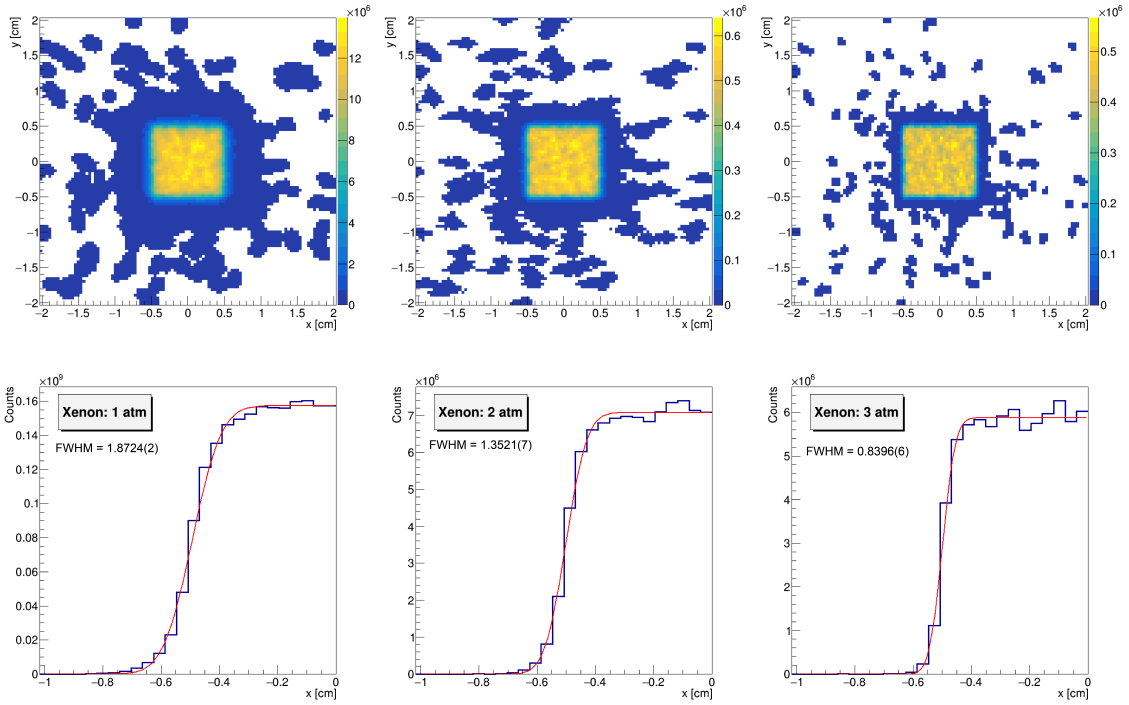

Figure 6.7: Optimization for xenon gas and three pressures: 1, 2 and 3 atm.

The optimization obtained with argon and xenon for three pressures is summarized with the FWHM of each setup in Figure 6.8. An improvement of at least $41\,\%$ can be

achieved in the simulations by making these changes in the gas composition and pressure, as shown in the results.

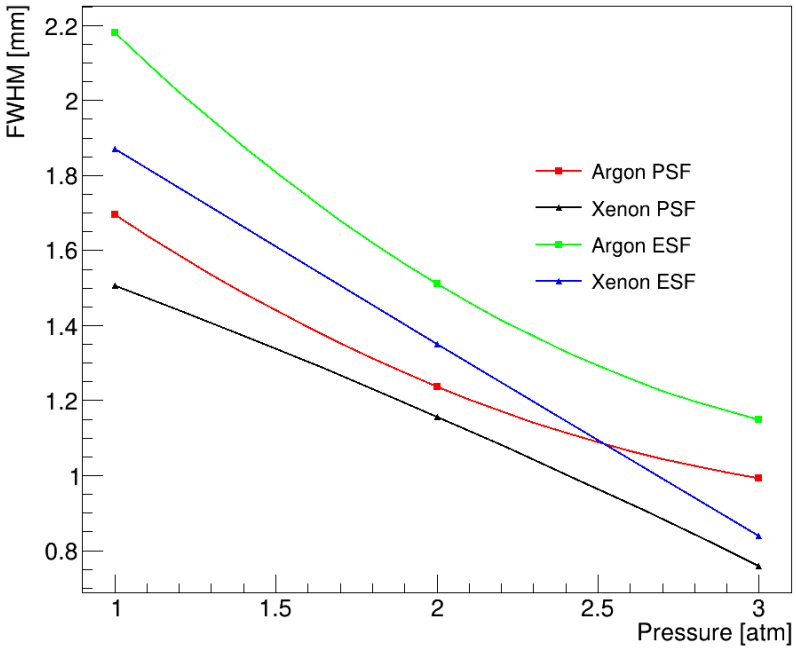

Figure 6.8: FWHM optimization using argon and xenon for both methods: PSF and ESF. The uncertainty is smaller than the point size.

The results in Figure 6.8 reveal that the spatial resolution has a complex dependence on different aspects of the detector design. The α-particles range is higher in argon with a pressure of $3\,\mathrm{atm}$ than in xenon with $2\,\mathrm{atm}$ (shown in Figure 6.1). However, the spatial resolution is better for the argon case with $3\,\mathrm{atm}$ pressure. Here, the diffusion of electrons in gases should be considered, because this is a significant factor for the position resolution, as discussed in 2.1.2.

Figure 6.9 presents the drift velocity of electrons in both gas mixtures simulated with Magboltz [65] through Garfield++ integration, showing that the electrons have a higher drift velocity in argon. Thus, it is expected that with a higher velocity the diffusion becomes smaller and then a better spatial resolution is obtained, as pointed out in Figure 6.8.

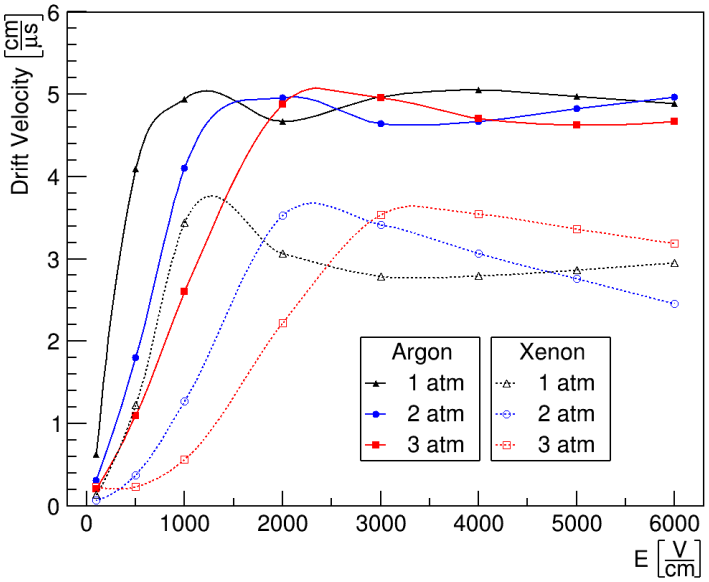

Figure 6.9: Drift velocity as a function of the drift field for gas mixtures at different pressures. Close and open marks represent argon and xenon gas, respectively. Figure from [90]. This was the only simulation in this section that was not done in the fast simulator but in Magboltz.

6.3 Summary

The optimizations evaluated using the fast simulator show that a position-sensitive detector can be optimized in terms of spatial resolution by changing its gas and/or changing its pressure. However, the drift velocity needs to be taken into account. In general, the optimizations analyzed showed an increase of at least $41\,\%$ for the cases studied in this work.

Chapter 7

Conclusion and Outlook

This work presented a parameterization strategy to build a fast simulator for GEM-based neutron detectors using GEANT4 and Garfield++ that results in the charge distribution from a thermal neutron interaction with a converter layer.

The code accelerates the simulation process parameterizing the charge distribution in the detector readout plane. In the performance test using an Intel Core i5-8265U CPU @1.60 GHz and 8GB of RAM, the fast simulator was 4 orders of magnitude faster. The full simulation would take $\approx 43\,\mathrm{h}$ per event (one neutron) while the fast simulator took only $\approx 12\,\mathrm{s}$ per event.

The spatial resolution as well as the energy spectrum obtained when comparing experimental results and the fast simulator predictions presented a good agreement, despite some differences that can be due to effects not implemented in the simulation, such as electronic noise or the lack of homogeneity in the neutron beam among others.

This tool was used to perform an optimization that aims for a better spatial resolution, showing that changes in the working gas as its composition to one with a higher atomic number and/or a higher pressure are good choices to improve the spatial resolution, with all simulations showing an improvement of at least $41\,\%$. The simulation shows that the drift velocity must also be considered for the optimization, clarifying the importance of a detailed simulation for detector optimization and the utility of the created code.

This fast simulator is a versatile tool that can be explored and improved to achieve a higher agreement with the experiment through the implementation of other experimental effects such as the electronic noise and a more realistic readout system. Its usage can be extended to detect heavy charged particles, not only restricted to thermal neutrons, corroborating its versatility.

Bibliography

[1] K. Tsorbatzoglou and R. D. McKeag, "Novel and efficient 10b lined tubelet detector as a replacement for 3he neutron proportional counters," *Nuclear Instruments and Methods in Physics Research Section A: Accelerators, Spectrometers, Detectors and Associated Equipment*, vol. 652, no. 1, pp. 381–383, 2011, symposium on Radiation Measurements and Applications (SORMA) XII 2010. [Online]. Available: https://www.sciencedirect.com/science/article/pii/S0168900210018899

[2] P. Peerani, A. Tomanin, S. Pozzi, J. Dolan, E. Miller, M. Flaska, M. Battaglieri, R. De Vita, L. Ficini, G. Ottonello, G. Ricco, G. Dermody, and C. Giles, "Testing on novel neutron detectors as alternative to 3he for security applications," *Nuclear Instruments and Methods in Physics Research Section A: Accelerators, Spectrometers, Detectors and Associated Equipment*, vol. 696, pp. 110–120, 2012. [Online]. Available: https://www.sciencedirect.com/science/article/pii/S0168900212007929

[3] A. Pietropaolo, F. Murtas, G. Claps, L. Quintieri, D. Raspino, G. Celentano, A. Vannozzi, and O. Frasciello, "A new 3he-free thermal neutrons detector concept based on the gem technology," *Nuclear Instruments and Methods in Physics Research Section A: Accelerators, Spectrometers, Detectors and Associated Equipment*, vol. 729, pp. 117–126, 2013. [Online]. Available: https://www.sciencedirect.com/science/article/pii/S0168900213008917

[4] M. Titov, "New developments and future perspectives of gaseous detectors," *Nuclear Instruments and Methods in Physics Research Section A: Accelerators, Spectrometers, Detectors and Associated Equipment*, vol. 581, no. 1, pp. 25–37, 2007, vCI 2007. [Online]. Available: https://www.sciencedirect.com/science/article/pii/S0168900207014441

[5] F. Sauli, "GEM: A new concept for electron amplification in gas detectors," *Nuclear Instruments and Methods in Physics Research Section A: Accelerators, Spectrometers, Detectors and Associated Equipment*, vol. 386, no. 2-3, pp. 531–534, feb 1997.

[6] S. Agostinelli, J. Allison, K. Amako, J. Apostolakis, H. Araujo, P. Arce, M. Asai, D. Axen, S. Banerjee, G. Barrand, F. Behner, L. Bellagamba, J. Boudreau, L. Broglia, A. Brunengo, H. Burkhardt, S. Chauvie, J. Chuma, R. Chytracek, G. Cooperman, G. Cosmo, P. Degtyarenko, A. Dell'Acqua, G. Depaola, D. Dietrich, R. Enami, A. Feliciello, C. Ferguson, H. Fesefeldt, G. Folger, F. Foppiano, A. Forti, S. Garelli, S. Giani, R. Giannitrapani, D. Gibin, J. Gómez Cadenas, I. González, G. Gracia Abril, G. Greeniaus, W. Greiner, V. Grichine, A. Grossheim, S. Guatelli, P. Gumplinger, R. Hamatsu, K. Hashimoto, H. Hasui, A. Heikkinen, A. Howard,

V. Ivanchenko, A. Johnson, F. Jones, J. Kallenbach, N. Kanaya, M. Kawabata, Y. Kawabata, M. Kawaguti, S. Kelner, P. Kent, A. Kimura, T. Kodama, R. Kokoulin, M. Kossov, H. Kurashige, E. Lamanna, T. Lampén, V. Lara, V. Lefebure, F. Lei, M. Liendl, W. Lockman, F. Longo, S. Magni, M. Maire, E. Medernach, K. Minamimoto, P. Mora de Freitas, Y. Morita, K. Murakami, M. Nagamatu, R. Nartallo, P. Nieminen, T. Nishimura, K. Ohtsubo, M. Okamura, S. O'Neale, Y. Oohata, K. Paech, J. Perl, A. Pfeiffer, M. Pia, F. Ranjard, A. Rybin, S. Sadilov, E. Di Salvo, G. Santin, T. Sasaki, N. Savvas, Y. Sawada, S. Scherer, S. Sei, V. Sirotenko, D. Smith, N. Starkov, H. Stoecker, J. Sulkimo, M. Takahata, S. Tanaka, E. Tcherniaev, E. Safai Tehrani, M. Tropeano, P. Truscott, H. Uno, L. Urban, P. Urban, M. Verderi, A. Walkden, W. Wander, H. Weber, J. Wellisch, T. Wenaus, D. Williams, D. Wright, T. Yamada, H. Yoshida, and D. Zschiesche, "Geant4—a simulation toolkit," *Nuclear Instruments and Methods in Physics Research Section A: Accelerators, Spectrometers, Detectors and Associated Equipment*, vol. 506, no. 3, pp. 250–303, jul 2003.

[7] H. Schindler and R. Veenhof, "Garfield++ - Simulation of Tracking Detectors," http://cern.ch/garfieldpp.

[8] E. Rutherford, "Bakerian lecture: nuclear constitution of atoms," *Proceedings of the Royal Society of London. Series A, Containing Papers of a Mathematical and Physical Character*, vol. 97, no. 686, pp. 374–400, 1920.

[9] W. Bothe and H. Becker, "Künstliche Erregung von Kern-γ-Strahlen," *Zeitschrift fur Physik*, vol. 66, no. 5-6, pp. 289–306, May 1930.

[10] I. Joliot-Curie and F. Joliot-Curie, *Émission de protons de grande vitesse par les substances hydrogénées sous l'influence des rayons-γ tres pénétrants*. Gauthier-Villars, 1932.

[11] J. Chadwick, "The existence of a neutron," *Proceedings of the Royal Society of London. Series A, Containing Papers of a Mathematical and Physical Character*, vol. 136, no. 830, pp. 692–708, jun 1932. [Online]. Available: https://royalsocietypublishing.org/

[12] E. Amaldi, "From the discovery of the neutron to the discovery of nuclear fission," *Physics Reports*, vol. 111, no. 1, pp. 1–331, 1984. [Online]. Available: https://www.sciencedirect.com/science/article/pii/037015738490214X

[13] S. Paul, "The puzzle of neutron lifetime," *Nuclear Instruments and Methods in Physics Research Section A: Accelerators, Spectrometers, Detectors and Associated Equipment*, vol. 611, no. 2, pp. 157–166, 2009, particle Physics with Slow Neutrons. [Online]. Available: https://www.sciencedirect.com/science/article/pii/S0168900209015174

[14] F. M. Gonzalez, E. M. Fries, C. Cude-Woods, T. Bailey, M. Blatnik, L. J. Broussard, N. B. Callahan, J. H. Choi, S. M. Clayton, S. A. Currie, M. Dawid, E. B. Dees, B. W. Filippone, W. Fox, P. Geltenbort, E. George, L. Hayen, K. P. Hickerson, M. A. Hoffbauer, K. Hoffman, A. T. Holley, T. M. Ito, A. Komives, C.-Y. Liu, M. Makela,

C. L. Morris, R. Musedinovic, C. O'shaughnessy, R. W. Pattie, J. Ramsey, D. J. Salvat, A. Saunders, E. I. Sharapov, S. Slutsky, V. Su, X. Sun, C. Swank, Z. Tang, W. Uhrich, J. Vanderwerp, P. Walstrom, Z. Wang, W. Wei, and A. R. Young, "Improved neutron lifetime measurement with ucnτ," 2021.

[15] A. T. Yue, M. S. Dewey, D. M. Gilliam, G. L. Greene, A. B. Laptev, J. S. Nico, W. M. Snow, and F. E. Wietfeldt, "Improved determination of the neutron lifetime," *Phys. Rev. Lett.*, vol. 111, p. 222501, Nov 2013. [Online]. Available: https://link.aps.org/doi/10.1103/PhysRevLett.111.222501

[16] D. Castelvecchi, "Physicists make most precise measurement ever of neutron's lifetime," oct 2021. [Online]. Available: https://doi.org/10.1038/d41586-021-02812-z

[17] P. Zyla *et al.*, "Review of Particle Physics," *PTEP*, vol. 2020, no. 8, p. 083C01, 2020, and 2021 update.

[18] L. W. Alvarez and F. Bloch, "A quantitative determination of the neutron moment in absolute nuclear magnetons," *Phys. Rev.*, vol. 57, pp. 111–122, Jan 1940. [Online]. Available: https://link.aps.org/doi/10.1103/PhysRev.57.111

[19] B. Willis and C. Carlile, *Experimental Neutron Scattering*. OUP Oxford, 2017. [Online]. Available: https://books.google.com.br/books?id=aPR0DgAAQBAJ

[20] M. Köhli, F. Allmendinger, W. Häußler, T. Schröder, M. Klein, M. Meven, and U. Schmidt, "Efficiency and spatial resolution of the CASCADE thermal neutron detector," *Nuclear Instruments and Methods in Physics Research A*, vol. 828, pp. 242–249, Aug. 2016.

[21] H. Cember and T. E. Johnson, *Introduction to health physics*. NNRA Library, 2009.

[22] S. N. Ahmed, *Physics and engineering of radiation detection*, 2014.

[23] W. R. Leo, *Techniques for Nuclear and Particle Physics Experiments: a How-to Approach*. Springer Berlin Heidelberg, 1994.

[24] G. F. Knoll, *Radiation detection and measurement*. John Wiley, 2010.

[25] J. F. Ziegler, M. D. Ziegler, and J. P. Biersack, "SRIM - The stopping and range of ions in matter (2010)," *Nuclear Instruments and Methods in Physics Research, Section B: Beam Interactions with Materials and Atoms*, vol. 268, no. 11-12, pp. 1818–1823, jun 2010. [Online]. Available: https://ui.adsabs.harvard.edu/abs/2010NIMPB.268.1818Z/abstract

[26] M. Joyce, *Nuclear Engineering: A Conceptual Introduction to Nuclear Power*. Elsevier Science, 2017. [Online]. Available: https://books.google.com.br/books?id=HXbUDAAAQBAJ

[27] R. T. Kouzes, J. H. Ely, L. E. Erikson, W. J. Kernan, A. T. Lintereur, E. R. Siciliano, D. L. Stephens, D. C. Stromswold, R. M. V. Ginhoven, and M. L. Woodring, "Neutron detection alternatives to 3 he for national security applications," 2010. [Online]. Available: www.elsevier.com/locate/nima

[28] C. Tyler, "Running low. in: 1663 - los alamos science and technology magazine," https://www.lanl.gov/discover/publications/1663/2014-august/_assets/docs/1663_22_HE3.pdf, pp. 8–13, 2014. [Online]. Available: https://www.lanl.gov/discover/publications/1663/2014-august/_assets/docs/1663_22_HE3.pdf

[29] A. Koning, D. Rochman, J.-C. Sublet, N. Dzysiuk, M. Fleming, and S. van der Marck, "Tendl: Complete nuclear data library for innovative nuclear science and technology," *Nuclear Data Sheets*, vol. 155, pp. 1–55, 2019, special Issue on Nuclear Reaction Data. [Online]. Available: https://www.sciencedirect.com/science/article/pii/S009037521930002X

[30] N. Tsoulfanidis and S. Landsberger, *Measurement and Detection of Radiation*. CRC Press, Taylor & Francis Group, 2015. [Online]. Available: https://books.google.com.br/books?id=A93WoQEACAAJ

[31] D. S. McGregor, M. D. Hammig, Y. H. Yang, H. K. Gersch, and R. T. Klann, "Design considerations for thin film coated semiconductor thermal neutron detectors - i: Basics regarding alpha particle emitting neutron reactive films," *Nuclear Instruments and Methods in Physics Research, Section A: Accelerators, Spectrometers, Detectors and Associated Equipment*, vol. 500, pp. 272–308, 11 2003.

[32] L. S. Filho, R. F. dos Santos, G. de Souza, M. Paulino, F. Souza, M. Moralles, H. da Luz, M. Bregant, M. Munhoz, C.-C. Lai, C. Höglund, P.-O. Svensson, L. Robinson, and R. Hall-Wilton, "Double-GEM based thermal neutron detector prototype," *Journal of Instrumentation*, vol. 17, no. 09, p. P09018, sep 2022. [Online]. Available: https://doi.org/10.1088/1748-0221/17/09/p09018

[33] E. Rutherford and H. Geiger, "An electrical method of counting the number of α-particles from radio-active substances," *Proceedings of the Royal Society of London. Series A, Containing Papers of a Mathematical and Physical Character*, vol. 81, pp. 141–161, 8 1908. [Online]. Available: https://royalsocietypublishing.org/

[34] W. Blum, L. Rolandi, and W. Riegler, *Particle detection with drift chambers*, ser. Particle Acceleration and Detection, 2008.

[35] F. Sauli, *Gaseous Radiation Detectors: Fundamentals and Applications*, ser. Cambridge Monographs on Particle Physics, Nuclear Physics and Cosmology. Cambridge University Press, 2023.

[36] A. Peisert and F. Sauli, *Drift and diffusion of electrons in gases: a compilation (with an introduction to the use of computing programs)*, ser. CERN Yellow Reports: Monographs. Geneva: CERN, 1984. [Online]. Available: https://cds.cern.ch/record/154069

[37] A. Oed, "Position-sensitive detector with microstrip anode for electron multiplication with gases," *Nuclear Instruments & Methods in Physics Research Section A-accelerators Spectrometers Detectors and Associated Equipment*, vol. 263, pp. 351–359, 1988.

[38] F. Sauli, *Gaseous radiation detectors : fundamentals and applications*. Cambridge University Press, 2014.

[39] Y. Giomataris, P. Rebourgeard, J. P. Robert, and G. Charpak, "Micromegas: A high-granularity position-sensitive gaseous detector for high particle-flux environments," *Nuclear Instruments and Methods in Physics Research, Section A: Accelerators, Spectrometers, Detectors and Associated Equipment*, vol. 376, pp. 29–35, 6 1996.

[40] D. Attié, S. Aune, E. Berthoumieux, F. Bossù, P. Colas, A. Delbart, E. Dupont, E. F. Ribas, I. Giomataris, A. Glaenzer, H. Gómez, F. Gunsing, F. Jambon, F. Jeanneau, M. Lehuraux, D. Neyret, T. Papaevangelou, E. Pollacco, S. Procureur, M. Revolle, P. Schune, L. Segui, L. Sohl, M. Vandenbroucke, and Z. Wu, "Current status and future developments of micromegas detectors for physics and applications," *Applied Sciences*, vol. 11, no. 12, 2021. [Online]. Available: https://www.mdpi.com/2076-3417/11/12/5362

[41] F. Sauli, "GEM: A new concept for electron amplification in gas detectors," *Nuclear Instruments and Methods in Physics Research Section A: Accelerators, Spectrometers, Detectors and Associated Equipment*, vol. 386, no. 2-3, pp. 531–534, feb 1997.

[42] J. Adolfsson, M. Ahmed, S. Aiola, J. Alme, T. Alt, W. Amend, F. Anastasopoulos, C. Andrei, M. Angelsmark, V. Anguelov, A. Anjam, H. Appelshäuser, V. Aprodu, O. Arnold, M. Arslandok, D. Baitinger, M. Ball, G. Barnaföldi, E. Bartsch, P. Becht, R. Bellwied, A. Berdnikova, M. Berger, N. Bialas, P. Bialas, S. Biswas, B. Blidaru, L. Boldizsár, L. Bratrud, P. Braun-Munzinger, M. Bregant, C. Britton, S. Brucker, E. Brücken, H. Büsching, R. Soto Camacho, A. Campos, G. Caragheorgheopol, D. Carvalho, A. Castro, P. Chatzidaki, P. Christiansen, L. Clonts, T. Cormier, A. Couto, H. Cubas, A. Deisting, P. Dhankher, S. Dittrich, V. Duta, R. Ehlers, M. Engel, M. Ericson, N. Ezell, L. Fabbietti, F. Flor, G. Föhner, U. Frankenfeld, E. Futo, J. Gaardhøje, M. Munhoz, C. Garabatos, P. Gasik, T. Geiger, Á. Gera, P. Glässel, D. Goh, O. Grachov, A. Grein, M. Gul, T. Gunji, M. Habib, H. Hamagaki, G. Hamar, J. Hansen, A. Harlenderova, J. Harris, S. Hassan, P. Hauer, S. Hayashi, S. Heckel, J. Hehner, J. Heino, E. Hellbär, H. Helstrup, A. Herghelegiu, L. Hernandes da Costa Porto, R. Hernandez, H. Hernandez Herrera, T. Herold, T. Hilden, B. Hohlweger, S. Hornung, C. Hughes, S. Hummel, M. Ivanov, J. Jung, M. Jung, D. Just, E. Kangasaho, L. Karayan, B. Ketzer, S. Kirsch, M. Kleiner, T. Klemenz, S. Klewin, A. Knospe, E. Koskinen, M. Kowalski, L. Kreis, M. Krüger, N. Kupfer, R. Lang, L. Lautner, M. Lesch, Y. Lesenechal, F. Liebske, C. Lippmann, V. Litichevskyi, M. Ljunggren, W. Llope, S. Mahmood, T. Mahmoud, R. Majka, C. Markert, J. Martinez, T. Martins, S. Masciocchi, A. Mathis, O. Matonoha, Y. Matsuyama, A. Matyja, M. Meres, D. Mihaylov, D. Miśkowiec, T. Mittelstaedt, L. Montali, D. Moraes, C. Mordasini, T. Morhardt, S. Muley, J. Mulligan, R. Munzer, H. Murakami, K. Münning, A. Nassirpour, H. Natal da Luz, C. Nattrass, R. Negrao De Oliveira, H. Neves, B. Nielsen, W. Noije, M. Ogino, A. Oliveira Da Silva, A. Oskarsson, J. Ottnad, K. Oyama, A. Önnerstad, L. Österman, A. Pabon, Y. Pachmayer, G. Paić, J. Parkkila, S. Pathak, R. Patra, V. Peskov, M. Petris, M. Petrovici, M. Planinic, F. Pompei, L. Prodan, A. Radu, L. Radulescu, J. Rak, J. Rasson, V. Ratza, K. Read, A. Rehman, R. Renfordt,

K. Røed, D. Röhrich, E. Rubio, T. Rudzki, A. Rusu, M. Saleh, B. Sanches, J. Schambach, S. Scheid, C. Schmidt, A. Schmier, H. Schulte, K. Schweda, D. Sekihata, N. Shimizu, S. Siebig, R. Silva, D. Silvermyr, D. Simpson, B. Sitar, N. Smirnov, T. Snellman, H. Soltveit, S. Sorensen, F. Sozzi, J. Stachel, A. Szabo, L. Šerkšnytė, Y. Takeuchi, G. Tambave, Y. Tanaka, K. Terasaki, R. Turpeinen, K. Ullaland, B. Ulukutlu, E. Umaka, A. Utrobicic, D. Varga, A. Vargas, M. Vargyas, R. Varma, O. Vazquez Rueda, A. Velure, S. Vereschagin, S. Vergara Limón, L. Vergara Urrutia, O. Vorbach, B. Voss, D. Vranic, R. Warmack, T. Weber, C. Weidlich, J. Wiechula, B. Windelband, S. Winkler, and W. Witt, "The upgrade of the ALICE TPC with GEMs and continuous readout," *Journal of Instrumentation*, vol. 16, no. 03, p. P03022, mar 2021. [Online]. Available: https://iopscience.iop.org/article/10.1088/1748-0221/16/03/P03022

[43] R. Venditti, "Production and quality control of the new chambers with GEM technology in the CMS Muon System," *Nuclear Instruments and Methods in Physics Research Section A: Accelerators, Spectrometers, Detectors and Associated Equipment*, vol. 936, pp. 476–478, 2019. [Online]. Available: https://www.sciencedirect.com/science/article/pii/S016890021831581X

[44] B. Ketzer, Q. Weitzel, S. Paul, F. Sauli, and L. Ropelewski, "Performance of triple GEM tracking detectors in the COMPASS experiment," *Nuclear Instruments and Methods in Physics Research Section A: Accelerators, Spectrometers, Detectors and Associated Equipment*, vol. 535, no. 1, pp. 314–318, 2004. [Online]. Available: https://www.sciencedirect.com/science/article/pii/S0168900204016687

[45] F. Sauli, "The gas electron multiplier (GEM): Operating principles and applications," *Nuclear Instruments and Methods in Physics Research Section A: Accelerators, Spectrometers, Detectors and Associated Equipment*, vol. 805, pp. 2–24, 2016.

[46] C. Altunbas, M. Capéans, K. Dehmelt, J. Ehlers, J. Friedrich, I. Konorov, A. Gandi, S. Kappler, B. Ketzer, R. D. Oliveira, S. Paul, A. Placci, L. Ropelewski, F. Sauli, F. Simon, and M. V. Stenis, "Construction, test and commissioning of the triple-gem tracking detector for compass," *Nuclear Instruments and Methods in Physics Research, Section A: Accelerators, Spectrometers, Detectors and Associated Equipment*, vol. 490, pp. 177–203, 9 2002.

[47] S. Bachmann, A. Bressan, L. Ropelewski, F. Sauli, A. Sharma, and D. Mörmann, "Charge amplification and transfer processes in the gas electron multiplier," *Nuclear Instruments and Methods in Physics Research Section A: Accelerators, Spectrometers, Detectors and Associated Equipment*, vol. 438, no. 2-3, pp. 376–408, dec 1999.

[48] A. Orthen, H. Wagner, H. Besch, S. Martoiu, R. H. Menk, A. Walenta, and U. Werthenbach, "Gas gain and signal length measurements with a triple-gem at different pressures of ar-, kr- and xe-based gas mixtures," *Nuclear Instruments and Methods in Physics Research Section A Accelerators Spectrometers Detectors and Associated Equipment*, vol. 512, 03 2003.

[49] K. Saenboonruang, "Recent developments in gem-based neutron detectors," *Journal of Physics: Conference Series*, vol. 611, no. 1, p. 012016, apr 2015. [Online]. Available: https://dx.doi.org/10.1088/1742-6596/611/1/012016

[50] C. Richter, A. Breskin, R. Chechik, D. Mörmann, G. Garty, and A. Sharma, "On the efficient electron transfer through gem," *Nuclear Instruments and Methods in Physics Research Section A: Accelerators, Spectrometers, Detectors and Associated Equipment*, vol. 478, no. 3, pp. 538–558, 2002. [Online]. Available: https://www.sciencedirect.com/science/article/pii/S0168900201008968

[51] W. R. Hendee and E. R. Ritenour, *Medical Imaging Physics*. John Wiley & Sons, Inc., 10 2002. [Online]. Available: http://doi.wiley.com/10.1002/0471221155

[52] *Geant 4 - Book For Application Developers. Release 11.0, Rev6.0, http://cern.ch/geant4-userdoc/UsersGuides/ForToolkitDeveloper/fo/BookForToolkitDevelopers.pdf (December 2021)*, Geant4 Collaboration. [Online]. Available: http://cern.ch/geant4-userdoc/UsersGuides/ForToolkitDeveloper/fo/BookForToolkitDevelopers.pdf

[53] T. G. collaboration, "Geant4, recommended physics lists." [Online]. Available: https://geant4.web.cern.ch/support/physics_lists/particle_physics/use_cases

[54] G. Folger and J. P. Wellisch, "String parton models in geant4," 6 2003. [Online]. Available: https://arxiv.org/abs/nucl-th/0306007

[55] H. W. Bertini, "Low-energy intranuclear cascade calculation," *Phys. Rev.*, vol. 131, pp. 1801–1821, Aug 1963. [Online]. Available: https://link.aps.org/doi/10.1103/PhysRev.131.1801

[56] A. Heikkinen, N. Stepanov, and J. P. Wellisch, "Bertini intra-nuclear cascade implementation in geant4," 6 2003. [Online]. Available: http://arxiv.org/abs/nucl-th/0306008

[57] A. Trkov and D. Brown, "ENDF-6 Formats Manual: Data formats and procedures for the evaluated nuclear data files," 2018. [Online]. Available: https://www-nds.iaea.org/exfor/x4guide/manuals/endf-manual.pdf

[58] E. Mendoza, D. Cano-Ott, T. Koi, and C. Guerrero, "New standard evaluated neutron cross section libraries for the geant4 code and first verification," *IEEE Transactions on Nuclear Science*, vol. 61, no. 4, pp. 2357–2364, 2014.

[59] E. Mendoza, D. Cano-Ott, C. Guerrero, and R. Capote, "International atomic energy agency indc international nuclear data committee new evaluated neutron cross section libraries for the geant4 code prepared by iaea nuclear data section, vienna international centre, a-1400 vienna, austria," 2012. [Online]. Available: http://www-nds.iaea.org/reports-new/indc-reports/

[60] E. Mendoza and D. Cano-Ott, "Indc international nuclear data committee update of the evaluated neutron cross section libraries for the geant4 code iaea nuclear data section," 2018. [Online]. Available: http://www-nds.iaea.org/publications

[61] C. Geuzaine and J.-F. Remacle, "Gmsh: A 3-D finite element mesh generator with built-in pre- and post-processing facilities," *International Journal for Numerical Methods in Engineering*, vol. 79, no. 11, pp. 1309–1331, sep 2009.

[62] J. Ruokolainen, M. Malinen, P. Raback, T. Zwinger, A. Pursula, and M. Byckling, "ElmerSolver Manual," 2022. [Online]. Available: http://www.nic.funet.fi/index/elmer/doc/ElmerSolverManual.pdf

[63] G. G. A. d. Souza, "X-ray fluorescence imaging system based on thick-gem detectors," Master's thesis, Universidade de São Paulo, 2019.

[64] H. Schindler, "Microscopic Simulation of Particle Detectors," 2012, presented 13 Dec 2012. [Online]. Available: https://cds.cern.ch/record/1500583

[65] S. F. Biagi, "Monte Carlo simulation of electron drift and diffusion in counting gases under the influence of electric and magnetic fields," *Nuclear Instruments and Methods in Physics Research, Section A: Accelerators, Spectrometers, Detectors and Associated Equipment*, vol. 421, no. 1-2, pp. 234–240, jan 1999.

[66] ——, "Magboltz - transport of electrons in gas mixtures," https://magboltz.web.cern.ch/magboltz/.

[67] Farinelli, Riccardo, "Gts - garfield-based triple-gem simulator," *EPJ Web Conf.*, vol. 245, p. 02025, 2020. [Online]. Available: https://doi.org/10.1051/epjconf/202024502025

[68] A. Amoroso, R. B. Ferroli, I. Balossino, M. Bertani, D. Bettoni, A. Bortone, A. Calcaterra, S. Cerioni, W. Cheng, G. Cibinetto, A. C. Ramusino, F. Cossio, M. D. R. Rolo, F. De Mori, M. Destefanis, J. Dong, F. Evangelisti, R. Farinelli, L. Fava, G. Felici, I. Garzia, M. Gatta, G. Giraudo, S. Gramigna, M. Greco, L. Lavezzi, M. Maggiora, R. Malaguti, A. Mangoni, S. Marcello, M. Melchiorri, G. Mezzadri, E. Pace, S. Pacetti, P. Patteri, J. Pellegrino, A. Rivetti, M. Scodeggio, S. Sosio, and S. Spataro, "Parsifal: a toolkit for triple-gem parametrized simulation," 2020. [Online]. Available: https://arxiv.org/abs/2005.04452

[69] Sheharyar, A., Bouhali, O., and Castaneda, A., "Speeding up and parallelizing the garfield++," *EPJ Web Conf.*, vol. 174, p. 06004, 2018. [Online]. Available: https://doi.org/10.1051/epjconf/201817406004

[70] E. Brücken and T. Hildén, "GEM Foil Quality Assurance For The ALICE TPC Upgrade," *EPJ Web of Conferences*, vol. 174, p. 03004, feb 2018. [Online]. Available: https://www.epj-conferences.org/10.1051/epjconf/201817403004

[71] "Upgrade of the ALICE Time Projection Chamber," Tech. Rep., Oct 2013. [Online]. Available: https://cds.cern.ch/record/1622286

[72] D. R. Canelhas, T. Stoyanov, and A. J. Lilienthal, "A survey of voxel interpolation methods and an evaluation of their impact on volumetric map-based visual odometry," in *2018 IEEE International Conference on Robotics and Automation (ICRA)*, 2018, pp. 3637–3643.

[73] L. d. A. S. Filho, "Gem-based thermal neutron detector with $^{10}B_4C$ deposition on aluminum cathode," Master's thesis, Universidade de São Paulo, 2021.

[74] S. Y. Ha, I. Kim, C. Hahn, D. Yoo, and S. Park, "Energy resolution of a single gem detector," *Journal of The Korean Physical Society - J KOREAN PHYS SOC*, vol. 55, 12 2009. [Online]. Available: https://www.researchgate.net/publication/239010285_Energy_Resolution_of_a_Single_GEM_Detector

[75] R. Farinelli, M. Alexeev, A. Amoroso, S. Bagnasco, R. B. Ferrioli, I. Balossino, M. Bertani, D. Bettoni, A. Bortone, F. Bianchi, A. Calcaterra, S. Cerioni, J. Chai, W. Cheng, S. Chiozzi, G. Cibinetto, F. Cossio, A. C. Ramusino, G. Cotto, M. D. R. Rolo, F. D. Mori, M. Destefanis, F. Evangelisti, L. Fava, G. Felici, L. Gaido, I. Garzia, M. Gatta, G. Giraudo, S. Gramigna, M. Greco, L. Lavezzi, S. Lusso, H. Li, M. Maggiora, R. Malaguti, A. Mangoni, S. Marcello, M. Melchiorri, G. Mezzadri, M. Mignone, S. Pacetti, P. Patteri, B. Passalacqua, A. Rivetti, M. Savrié, S. Sosio, S. Spataro, E. Tskhadadze, L. Yan, and R. Wheadon, "A fast and parametric digitization for triple-GEM detectors," *Journal of Physics: Conference Series*, vol. 1525, no. 1, p. 012113, apr 2020. [Online]. Available: https://doi.org/10.1088/1742-6596/1525/1/012113

[76] C. Azevedo, P. Correia, L. Carramate, A. Silva, and J. Veloso, "THGEM gain calculations using garfield++: solving discrepancies between simulation and experimental data," *Journal of Instrumentation*, vol. 11, no. 08, pp. P08 018–P08 018, aug 2016. [Online]. Available: https://doi.org/10.1088/1748-0221/11/08/p08018

[77] M. U. Ahmed, "Simulation of the electron and ion movement through a 4-gem stack," Master's thesis, Goethe University Frankfurt, 2021.

[78] IPEN, "Progress report: 2014-2016," 2018. [Online]. Available: https://www.ipen.br/portal_por/conteudo/documentos/PR_2014_2016_01Introduction.pdf

[79] E. Maprelian, W. M. Torres, A. B. Junior, P. E. Umbehaun, J. R. Berretta, and G. Sabundjian, "Total and partial loss of coolant experiments in an instrumented fuel assembly of iea-r1 research reactor," *Nuclear Engineering and Design*, vol. 363, p. 110610, 2020. [Online]. Available: https://www.sciencedirect.com/science/article/pii/S0029549318307301

[80] *Geant 4 - Physics Reference Manual. Release 10.7, Re5.0, https://geant4-userdoc.web.cern.ch/UsersGuides/PhysicsReferenceManual/fo/PhysicsReferenceManual.pdf (December 2020)*, Geant4 Collaboration. [Online]. Available: https://geant4-userdoc.web.cern.ch/UsersGuides/PhysicsReferenceManual/fo/PhysicsReferenceManual.pdf

[81] R. F. dos Santos, M. G. Munhoz, M. Moralles, L. A. S. Filho, M. Bregant, and F. A. Souza, "Development of a fast simulator for gem-based neutron detectors," *Journal of Physics: Conference Series*, vol. 2374, no. 1, p. 012160, nov 2022. [Online]. Available: https://dx.doi.org/10.1088/1742-6596/2374/1/012160

[82] K. P. Nesteruk, "Beam monitor detectors for medical applications," *Reports of Practical Oncology & Radiotherapy*, vol. 19, pp. S32–S36, 2014. [Online]. Available: https://www.sciencedirect.com/science/article/pii/S150713671400073X

[83] F. Issa, A. Khaplanov, R. Hall-Wilton, I. Llamas, M. D. Riktor, S. R. Brattheim, and H. Perrey, "Characterization of thermal neutron beam monitors," *Phys. Rev. Accel. Beams*, vol. 20, p. 092801, Sep 2017. [Online]. Available: https://link.aps.org/doi/10.1103/PhysRevAccelBeams.20.092801

[84] T. Yang, J. Zhou, X. Zhou, L. Zhu, H. Zhu, J. Zhou, Y. Xia, Y. Wei, X. Jiang, W. Yang, G. Yang, S. Wang, Y. Xie, Z. Sun, Q. Ouyang, J. Zhu, and Y. Chen, "A novel method to improve the spatial resolution of gem neutron detectors with a stopping layer," *IEEE Transactions on Nuclear Science*, vol. 69, no. 1, pp. 68–77, 2022.

[85] M. Klein and C. J. Schmidt, "CASCADE, neutron detectors for highest count rates in combination with ASIC/FPGA based readout electronics," *Nuclear Instruments and Methods in Physics Research Section A: Accelerators, Spectrometers, Detectors and Associated Equipment*, vol. 628, no. 1, pp. 9–18, 2011, vCI 2010. [Online]. Available: https://www.sciencedirect.com/science/article/pii/S0168900210014683

[86] D. Pfeiffer, F. Resnati, J. Birch, R. Hall-Wilton, C. Höglund, L. Hultman, G. Iakovidis, E. Oliveri, E. Oksanen, L. Ropelewski, and P. Thuiner, "The μTPC method: improving the position resolution of neutron detectors based on MPGDs," *Journal of Instrumentation*, vol. 10, no. 04, pp. P04 004–P04 004, apr 2015. [Online]. Available: https://doi.org/10.1088/1748-0221/10/04/p04004

[87] B. Flierl, R. Hertenberger, O. Biebel, and K. Zeitelhack, "Tpc-like readout for thermal neutron detection using a gem-detector," *Nuclear Instruments and Methods in Physics Research Section A: Accelerators, Spectrometers, Detectors and Associated Equipment*, vol. 824, pp. 528–531, 2016, frontier Detectors for Frontier Physics: Proceedings of the 13th Pisa Meeting on Advanced Detectors. [Online]. Available: https://www.sciencedirect.com/science/article/pii/S0168900215014680

[88] D. Pfeiffer, F. Resnati, J. Birch, M. Etxegarai, R. Hall-Wilton, C. Höglund, L. Hultman, I. Llamas-Jansa, E. Oliveri, E. Oksanen, L. Robinson, L. Ropelewski, S. Schmidt, C. Streli, and P. Thuiner, "First measurements with new high-resolution gadolinium-GEM neutron detectors," *Journal of Instrumentation*, vol. 11, no. 05, pp. P05 011–P05 011, may 2016. [Online]. Available: https://doi.org/10.1088/1748-0221/11/05/p05011

[89] Y. Zhang, H. Wu, J. Zhou, S. Zhao, and B. Hu, "Track identification and reconstruction in fast neutron detection by mpgd," *Nuclear Instruments and Methods in Physics Research Section A: Accelerators, Spectrometers, Detectors and Associated Equipment*, vol. 906, pp. 68–76, 2018. [Online]. Available: https://www.sciencedirect.com/science/article/pii/S0168900218309598

[90] R. F. dos Santos, M. G. Munhoz, and M. Moralles, "Performance and optimization of a GEM-based neutron detector using a parameterized fast simulator," *Journal*

of Physics: Conference Series, vol. 2340, no. 1, p. 012048, sep 2022. [Online]. Available: https://doi.org/10.1088/1742-6596/2340/1/012048